

Band topology and exchange effects in compensated Eu-based compounds



Dissertation

zur Erlangung des Grades

“Doktor der Naturwissenschaften”

am Fachbereich Physik, Mathematik und Informatik

der Johannes Gutenberg-Universität

in Mainz

Nayra Adriana Alvarez Pari

geboren am 17th September 1995

in Cochabamba, Bolivien

Mainz, 10th October 2025

Berichterstatter: removed due to data protection

removed due to data protection

Prüfungsdatum: 2nd February 2026

This work is licensed under attribution (CC-BY-4.0).

Anhänge gemäß Prüfungsordnung

Ich versichere, dass ich die Arbeit selbstständig verfasst und keine anderen als die angegebenen Quellen und Hilfsmittel benutzt sowie Zitate kenntlich gemacht habe.

I hereby declare that the thesis submitted is my own unaided work. All direct or indirect sources used are acknowledged as references.

10 October 2025

Nayra Adriana Alvarez Pari
INSPIRE Group
Institut für Physik – FB 08

Staudingerweg 7
Johannes Gutenberg University
D-55128 Mainz

Abstract

The family of Eu-based compounds has attracted significant attention as a rich platform for exploring the interplay between the magnetic order – arising from the localized Eu 4f electrons – and the band topology. In particular, several compensated magnetic states within this family have been reported to host exotic topological phases, which are not only promising for technological applications such as more stable nanoscale devices, but also offer the opportunity to explore high-energy physics phenomena in condensed matter systems.

In this Thesis, we investigate the band topology and surface states of the conventional collinear antiferromagnetic phase of EuCd_2As_2 – a phase that exhibits spin degeneracy in momentum-space – both in the absence and under strain effects. Our analysis is based on magnetic symmetry and topological analysis of the electronic structure. We show that shear strain serves as an effective tuning parameter between the Dirac semimetal and the axion insulator phase, and induces gapped surfaces, thereby enhancing the prospects for the experimental detection of the axion insulator phase in this compound and related materials.

We further investigate two compensated non-collinear magnetic orders reported in the axion insulator candidate EuIn_2As_2 – the helical and the broken-helical phases – aiming to identify the exchange-dominated effects on the electronic structure. Our results reveal a non-relativistic spin-split bands characterized by a pure odd-parity-wave spin polarization in the helical phase, and a mixed even and odd parity character in the broken-helical phase. Altogether, we provide a comprehensive characterization of the exchange-induced spin polarization in momentum-space, offering new insights into the microscopic mechanisms governing this material and opening new research directions for exploring the interplay of unconventional magnetism and topology. We have also computed a spin-dependent transport response, the Edelstein effect, which primarily originates from the odd-parity character of the spin polarization and exhibits a predominantly non-relativistic origin. Since these two non-collinear magnetic phases in EuIn_2As_2 are regarded as topological insulating states, the Edelstein effect could enable for low-dissipation electric-field control of the magnetic order.

Keywords: Topological phases, electronic structure, compensated order, spin symmetries, odd-parity-wave magnetism, Edelstein effect.

Acknowledgements

Removed due to data privacy.

Contents

Anhänge gemäß Prüfungsordnung

Abstract	i
Acknowledgements	iii
Introduction	1
1 Symmetries and Topology in compensated magnets	9
1.1 Blochs Theorem and the Reciprocal space	10
1.1.1 Symmetry constraints on the electronic structure	11
1.2 Magnetic materials: A symmetry perspective	12
1.2.1 Magnetic space groups	12
1.2.2 Spin space groups	15
1.3 Topological band theory	19
1.3.1 Topological insulators	20
1.3.2 Weyl and Dirac semimetals	23
1.3.3 Magnetic topological quantum chemistry	25
1.4 Summary	26
2 First principles electronic theory	29
2.1 Density functional theory	30
2.1.1 Non-relativistic Kohn-Sham equations	30
2.1.2 Potential and wavefunction approximations	34
2.1.3 Relativistic Kohn-Sham equations	36
2.2 Wannier interpolation method	36
2.3 Surface state calculations	38
2.4 Summary	41
3 Strain control of band topology in collinear EuCd_2As_2	43
3.1 Crystal structure of collinear AFM EuCd_2As_2	43
3.2 The Dirac semimetal phase in the out-of-plane AFM EuCd_2As_2	45
3.3 Higher-order topological insulator phase in the in-plane AFM EuCd_2As_2	47

3.4	Band topology under shear strain	49
3.5	Summary	52
4	Exchange-dominated physics in non-collinear EuIn_2As_2	53
4.1	Magnetic configuration	54
4.2	Non-trivial spin point group classification	55
4.3	The helical phase	57
4.4	The broken-helical phase	63
4.5	Non-relativistic linear Edesltein effect	66
4.6	Summary	70
	Conclusion	73
	Appendix A Symmetry transformation rules of the linear response tensor	75
	Bibliography	77

Introduction

“When you hear of a sudden unexpected discovery – a bolt from the blue – you can always be sure that it has grown up by the influence of one individual to another, and it is the mutual influence which makes the enormous possibility of scientific advance”

— Ernest Rutherford

The unprecedented growth of digital information over the past decade, boosted by the COVID-19 pandemic and further accelerated by the rise of artificial intelligence technologies, has created a growing demand for more efficient ways to store and manipulate information, specially as the current ferromagnet-based spintronic technologies approach the limits on spatial integration and switching speed of magnetic memory bits. Spintronics exploit the control over the electrons spins to develop electronic devices, so identifying new materials capable of supporting next-generation electronic devices has become of greatest importance. In this context, compensated magnets – that exhibit a vanishing net magnetization – were first identified by Louis Néel in the 1930s [1]; at the time, they were seen as extremely interesting from a theoretical point of view, yet useless for applications [2, 3]. In recent years, however, they have emerged as a promising platform for developing an alternative class of spintronics with an ultrafast dynamics, and minimal stray fields that enable highly dense device integration [4–8].

Compensated magnets were long assumed to have spin-degenerate bands across the entire momentum-space. While this holds true for conventional antiferromagnets (AFMs) that preserve \mathcal{PT} or $\mathcal{PT}\tau$, which guarantees Kramers spin degeneracy at every \mathbf{k} , it is not the case for the so-called *unconventional* CMs, which instead exhibit splittings with a characteristic higher-order partial wave ordering (either with a odd p-, f-wave or even d-,g-,i-wave order), even at the absence of spin-orbit coupling (SOC) [9, 10].

Meanwhile, the study of topological phases of matter has further expanded from non-magnetic systems to their magnetic counterparts, revealing a rich phenomenology [11]. Within compensated materials, there have been proposals ranging from fast topological memories [12, 13] to topological spin textures that allow more stable nanoscale

magnetic structures [14]. Beyond applications, compensated topological materials also provide a fertile arena for fundamental studies, probing of Dirac [15] and Weyl [16, 17] quasiparticles, the chiral anomaly [16], and even proposals to detect the axion dark matter [18–20].

A remarkable topological phase that emerges exclusively within amgnetic materials, in covevntional antiferromagnets, is the 3D Dirac semimetal (DSM) phase, which hosts fourfold degenerate linear band crossings – Dirac points (DPs) – near the Fermi level. In the vicinity of these points, electrons behave as high-energy Dirac fermions. This phase has attracted particular interest for possibly enabling fast topological memory devices based on the metal-insulator transition [12, 21]. Beyond the DSM phase, a wide variety of exotic topological phases have been as well predicted to emerge in CMs – including Weyl semimetals [22, 23], axion insulators [24], and higher-order topological insulators (HOTIs) [25, 26]- making them a fertile platform for exploring the interplay between topology and their compensated order [27]. Device applications based on topological magnets typically requires a precise control over their topological properties. Since a crystal topological properties are intimately related to and defined by its symmetries [11, 28–30], they can be effectively controlled via symmetry-breaking perturbations, such as external magnetic or electric fields [12, 21, 31, 32], chemical doping [33], and latttice deformations via strain or pressure [34–37].

Motivated by the rich variety of compensated magnetic phases with non-trivial topology reported in Eu-based compounds [25, 38–45], we select the antiferromagnetic EuCd_2As_2 as our first model system, as theory and experiments proposed it can host multiple topological phases [24, 39, 46–48]. This compound exhibits two collinear antiferromagnetic phases as its lowest energy configurations, which can stabilize either the Dirac semimetal phase or the axion insulator phase depending on Néel vector orientation [24, 39]. Efforts to control its topological properties, include the aplication of magnetic fields [48, 49], hydrostatic pressure [37, 50], and strain [34, 51]. In particular, applying anisotropic strain has become a powerful technique, as it can induce substantial changes on the electronic structure, which can be engineered in a continuous and precise manner [35, 36]. Accordingly, in Chapter 3, we explore the effects of shear strain as an additional tuning parameter to modulate the topological properties of AFM EuCd_2As_2 , combining symmetry analysis, first-principles calculations, and surface states to further track the emergence of topological boundary states.

We show in [52] that strain can open a gap on one of the natural cleavage surfaces of EuCd_2As_2 while preserving the axion insulator phase. The resulting gapped surface would promote the emergence of hinge modes propagating along these edges, enhancing prospects to realize the axion state and related topological magnetoelectric phenomena. In paticular, shear strain proves to be an effective tuning parameter for controlling the surface states in EuCd_2As_2 , or related systems.

The symmetry and topology analysis of EuCd_2As_2 was framed in terms of *magnetic*

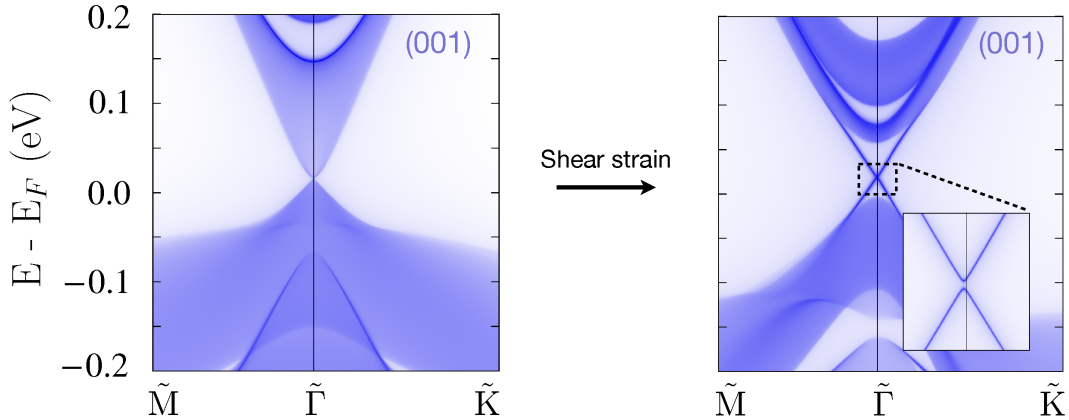


Figure 1: **Strain-induced gap opening on the AFM EuCd_2As_2** : The breaking of the threefold rotation symmetry C_{3z} in the out-of-plane AFM order opens a gap on the bulk, and the breaking of a glide mirror symmetry on the (001) surface induces a gap opening.

symmetries – the standard framework for exploring topological phases in magnetic materials [29]. An additional framework for describing the symmetries of magnetic materials is provided by *spin symmetries*, particularly suited when spin-orbit coupling effects are weak [53–55]. This symmetry framework has recently gained notariety for providing a complete classification of collinear compensated magnets, allowing the identification of a new third *altermagnetic* class in which the *Kramers spin degeneracy* is lifted, resulting in alternating spin-split bands with a characteristic higher-partial-wave order constrained to an even-parity (d-, g- or i-wave order) that breaks \mathcal{T} in the electronic structure [56, 57]. The identification of this new altermagnetic class has provided an explanation for the unconventional \mathcal{T} -symmetry breaking in the electronic structure of compensated magnets and related phenomena that couldn’t be fully captured magnetic symmetry constraints alone [58–62]. Crucially, the complete classification of these unconventional magnetic orders through *spin point groups* has helped to identify its non-relativistic origin – arising primarily from exchange interactions and crystal fields [10].

In the search for odd-parity magnetic orderings in compensated magnets, Hellenes. Birk. A and co-authors [63] have identified non-collinear and non-centrosymmetric magnetic configurations that preserve $\mathcal{T}\tau$ symmetry, and show a p- or f-wave order in momentum-space, termed as p-wave magnets. In contrast to altermagnetic even-parity-wave orders, p-wave magnets are \mathcal{T} -symmetric in momentum-space, thereby forbidding transport responses such as the anomalous Hall effect. The key for this discovery relied on searching in materials with a non-collinear spin arrangement where the $\text{SO}(2)$ symmetry¹ is broken due to the absence of a unique spin quantization axis. Therefore the

¹ $\text{SO}(2)$ represents a group of continuous spin rotations around the collinearity axis that restricts the

magnetic orderings are no longer restricted to have even-parity in momentum-space. Consequently, materials with a non-collinear spin arrangement can be further interesting, as they can host a richer variety of magnetic orders and transport phenomena.

The family of Eu-122 compounds is often associated with strong spin-orbit coupling effects due to the localized Eu-4f electrons. Nevertheless, recent reports of non-relativistic spin-split bands reaching 150 meV in the collinear compensated phase of EuIn_2As_2 [64], indicate that exchange effects are also significant in this compound. In addition, this material has drawn particular interest as the axion insulator phase has been reported in the collinear phase [25]. However, experiments report a more complex non-collinear magnetic ground state rather than a simple collinear order in EuIn_2As_2 [40, 65–68]. Motivated in understanding the exchange-induced effects on the electronic structure of EuIn_2As_2 , we select two coplanar phases – the helical and broken-helical states – that consist of a pure-helix spin arrangement and a superposition of a pure-helix with an in-plane collinear antiferromagnetic order [40, 65], as illustrated in Fig 2. Notably, despite the more complex magnetic configuration, studies in Ref. [40] reports the axion insulator phase can persist.

We show in [69] that the pure helical spin texture gives rise to an odd-parity-wave magnetic order, with a p-wave character, very similar to the $\mathcal{T}\tau$ p-wave magnets [63] but only in the non-relativistic regime. Another similarity we identify between the helical phase and the p-wave magnets is that both exhibit a dominant collinear spin polarization in momentum-space, resulting from the presence of pure spin translation symmetries. Remarkably, the pure helix phase represents a case of a system that breaks \mathcal{T} as point group operator while inducing an effective \mathcal{T} -symmetric magnetic ordering in momentum-space in the non-relativistic regime. Additionally, we show that the g -wave altermagnetic order from the collinear order, survives in the non-collinear broken-helical phase. The presence of odd and even magnetic orderings in the broken-helical phase is expected as \mathcal{T} symmetry is broken (see Figure. 2). Furthermore, we find that the magnetic orderings and spin-split bands remain qualitatively unchanged when incorporating spin-orbit coupling effects.

Effective ways to probe unconventional magnetism often rely in transport responses. Responses allowed in odd-parity wave magnets, include the linear Edelstein effect [61], optical and photocurrent responses [70, 71]. To identify contrasting differences between the two non-collinear phases of EuIn_2As_2 studied here, we computed the Edelstein effect. Our results reveal a distinct out-of-plane polarized spin density with a significantly larger response in the pure-helix phase compared to the broken-helical phase, which could serve as a probe of the magnetic transition, which could also guide the experimental efforts in identifying the actual magnetic ground state of this compound [66]. Furthermore, our findings also show a giant non-relativistic Edelstein effect in the pure-helix phase of EuIn_2As_2 , akin to recent reports of highly efficient spin-to-charge

magnetic order to have even-parity.

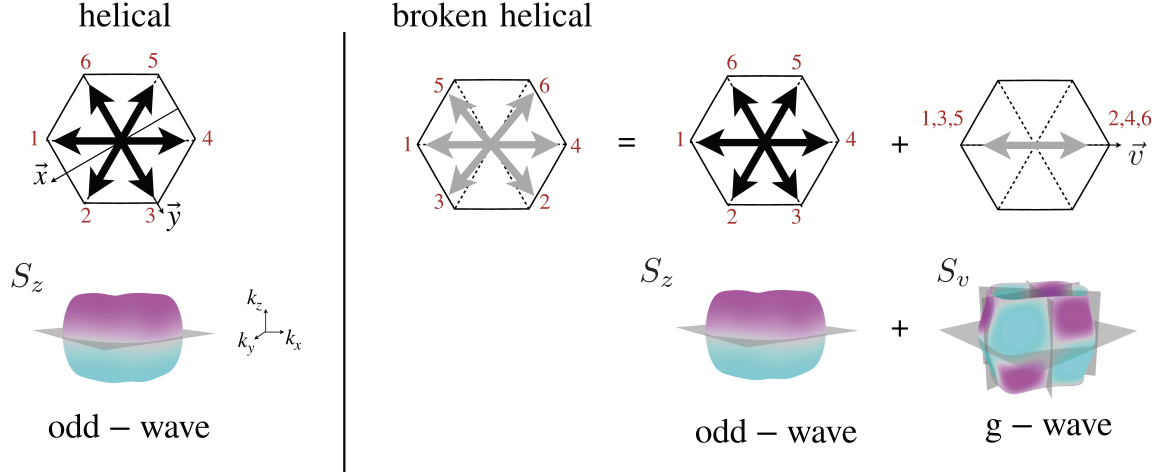


Figure 2: **Exchange-induced magnetic orderings of two non-collinear phases reported in EuIn_2As_2** : (Left) The pure helical magnetic configuration exhibits an effective \mathcal{T} -symmetric p-wave S_z order with a single nodal plane in momentum-space, however, only in the non-relativistic regime. (Right) The broken-helical phase hosts a mixed p-wave S_z order and an in-plane g -wave S_v order. The coloured red numbers indicate the index of the ferromagnetic layers within the six magnetic layers of the unit cell.

conversion in p-wave magnets [61].

The identification of an odd-wave and g -wave order in EuIn_2As_2 opens exciting research directions for exploring the interplay of unconventional magnetism, topology, and superconductivity in this compound [72, 73]. In addition, we show that *spin point groups* are a useful instrument for describing unconventional magnetic orders in non-collinear systems, even in materials where SOC can be strong.

Outline of the Thesis

This Thesis is structured as follows:

In Chapter 1, we introduce two symmetry frameworks for characterizing magnetic crystals, *magnetic symmetries* and *spin symmetries* and we discuss how these symmetries shape the electronic structure in momentum-space. We review the symmetry considerations under which the Kramers spin degeneracy holds in compensated magnets. Within the spin symmetries approach, we review how to construct the corresponding spin point groups for magnetic materials with collinear and non-collinear spin textures, a toolkit later applied to characterize the non-collinear configurations of EuIn_2As_2 . We also review the theoretical framework of band topology, with a particular emphasis on topological phases reported in compensated magnets, and discuss the symmetry-based indicators used to diagnose the non-trivial topology. Finally, we review the theory of magnetic topological quantum chemistry, which we have used to determine the topological phases of EuCd_2As_2 .

In Chapter 2, we review the density functional theory (DFT), and discuss the distinct key approximations taken into account to calculate the electronic band structures of our model systems. We also review how to construct a tight-binding model using atom-centered Wannier functions from the DFT energy bands, which we then use to calculate surface states and transport responses.

In Chapter 3 we examine the topology of the collinear antiferromagnetic EuCd_2As_2 , with and without strain effects. We combine a symmetry and topology analysis based on *magnetic symmetries*, with relativistic electronic band structure calculations and momentum-resolved surface states.

In Chapter 4 we explore the effects of exchange in the band structure of non-collinear compensated EuIn_2As_2 . We identify the magnetic orderings in momentum-space via spin symmetry analysis and verify our findings with non-relativistic electronic band structure calculations. We also discuss the non-relativistic linear Edelstein effect in this compound.

In the conclusion we summarize the main findings of this Thesis and provide an outlook regarding the materials studied here.

Chapter 1

Topology and symmetries of compensated magnets

"Symmetry arguments are often the most powerful tools for predicting or understanding the behavior of solids."

— Ashcroft & Mermin (Solid State Theory)

The foundational role of symmetries in condensed matter physics began with the classification of all possible periodic arrangements of atoms in crystals, leading to the identification of 230 *crystallographic space groups*. Changes in the crystal symmetries also played a crucial role in understanding phase transitions, known as the Landau's theory, formulated during the 1930s [74]. As the field advanced, topology emerged as a new avenue for classifying phases of matter, introducing an additional label – topological invariant – a quantized index that characterizes topological phases, which remain robust against small perturbations [75–77]. These invariants turned out to be intimately related to the crystal symmetries [28, 78]. In contrast to Landau's theory, distinct topological phases of matter can preserve the same symmetry group.

In the study of magnetic systems, the recent development of magnetic topological quantum chemistry [29], based on *magnetic space groups*, has introduced a complete set of symmetry-based indicators for classifying magnetic topological phases. More recently, however, *spin space groups* [53, 54, 79], have become the new protagonist for classifying magnetic phases, particularly in systems with unconventional compensated magnetic orderings [55, 57, 57, 80].

In this Chapter, we review and compare these two symmetry frameworks, *magnetic space groups* and *spin space groups*, and apply them to classify two collinear compensated orders in our candidate systems, EuCd_2As_2 and EuIn_2As_2 . We will discuss the symmetry constraints imposed on the electronic structure. Later in the Chapter, we will revisit important concepts in band topology and symmetry-based indicators focusing in compensated magnets.

1.1 Bloch's Theorem and the Reciprocal space

In commensurate crystalline structures, the atoms are arranged in a strictly periodic pattern, forming what is known as a *Bravais lattice*. In such systems, the position of the atoms \mathbf{R}_n can be decomposed as a linear combination of a set of three primitive lattice vectors $\mathbf{a}_1, \mathbf{a}_2, \mathbf{a}_3$, such that

$$\mathbf{R}_n = n_1\mathbf{a}_1 + n_2\mathbf{a}_2 + n_3\mathbf{a}_3, \quad (1.1)$$

where $\mathbf{n} = (n_1, n_2, n_3)$ and each n_i denote any integer. This formalism, however, is not applicable to incommensurate crystals, in which the long-range periodicity requires more than three n_i indices.

The periodic arrangement of the atoms induces a periodic potential, $V(\mathbf{r})$ that inherits the crystal's symmetries, satisfying $V(\mathbf{r} + \mathbf{R}_n) = V(\mathbf{r})$. As electrons propagate through the crystal, they are subject to this periodic potential. Consequently, the single-electron Hamiltonian \mathcal{H} can be written as,

$$\mathcal{H}(\mathbf{r}) = \frac{\mathbf{p}^2}{2m} + V(\mathbf{r}), \quad (1.2)$$

where \mathbf{p} denotes the electron's momentum and m the electron's mass.

The solution of this Hamiltonian through the Schrödinger equation can be achieved by mapping the periodic lattice to the *reciprocal space* using a Fourier transform. In the reciprocal space, the eigenvectors of \mathcal{H} are determined through the Bloch wavefunctions, as formulated in the *Bloch's theorem*. These wavefunctions consist of plane waves modulated by a function that is periodic within the unit cell.

Theorem 1.1.1 (Bloch's Theorem) *Given a periodic potential $V(\mathbf{r})$, the eigenvectors of the Hamiltonian \mathcal{H} , such that $\mathcal{H}|\psi_{n\mathbf{k}}\rangle = E_{n\mathbf{k}}|\psi_{n\mathbf{k}}\rangle$, can be written in the form*

$$\psi_{n\mathbf{k}} = e^{i\mathbf{k}\cdot\mathbf{r}} u_{n\mathbf{k}}(\mathbf{r}) \quad \text{with} \quad u_{n\mathbf{k}}(\mathbf{r}) = u_{n\mathbf{k}}(\mathbf{r} + \mathbf{R}_n), \quad (1.3)$$

where $\psi_{n\mathbf{k}}$ denote the Bloch wavefunctions, $e^{i\mathbf{k}\cdot\mathbf{r}}$ corresponds to a plane wave for a given wavevector \mathbf{k} , and $E_{n\mathbf{k}}$ represents the energy associated with the n -th electronic band at momentum \mathbf{k} .

To understand the structure of the Bloch wavefunctions in Eq.1.3, we start by defining the translation operator $\hat{T}_{\mathbf{R}}$, which transforms in real-space as $\hat{T}_{\mathbf{R}} f(\mathbf{r}) = f(\mathbf{r} + \mathbf{R})$. A group defined by all the translation operators forms an *Abelian* group. According to group theory, all the irreducible representations (irreps) of an *Abelian* group are one-dimensional [81]. The one-dimensional matrix representation assigned to each translation operator then can be written in the form $e^{ik_i r_i}$, where k_i labels each of the irreps. From that, one can demonstrate that the phase vector $e^{i\mathbf{k}\cdot\mathbf{R}}$ is an

eigenvalue of $\hat{T}_{\mathbf{R}}$,

$$\hat{T}_{\mathbf{R}}\psi_k(\mathbf{r}) = e^{i\mathbf{k}\cdot\mathbf{R}}\psi_k(\mathbf{r}) = \psi_k(\mathbf{r} + \mathbf{R}). \quad (1.4)$$

Finally, from the periodicity of $\mathcal{H}(\mathbf{r})$, we can conclude that $\hat{T}_{\mathbf{R}}$ commutes with the Hamiltonian, i.e., $[\mathcal{H}(\mathbf{r}), \hat{T}_{\mathbf{R}}] = 0$, which can be shown from

$$\hat{T}_{\mathbf{R}} \left(\mathcal{H}(\mathbf{r})\psi(\mathbf{r}) \right) = \mathcal{H}(\mathbf{r} + \mathbf{R})\psi(\mathbf{r} + \mathbf{R}) = \mathcal{H}(\mathbf{r}) \hat{T}_{\mathbf{R}}\psi(\mathbf{r}), \quad (1.5)$$

suggesting that the eigenfunctions of $\hat{T}_{\mathbf{R}}$ can also be chosen as simultaneous eigenfunctions of \mathcal{H} . As a result, the Eq. 1.3 follows from Eq. 1.4.

For a crystal of dimensions $\{L_1, L_2, L_3\}$ under open boundary conditions, the wavevector label k_i , which represents translations along each lattice vector direction are quantized $k_i = 2\pi \frac{m}{L_i}$, where m is an integer. The set of all these vectors $\mathbf{k} = (k_1, k_2, k_3)$ define the first *Brillouin zone* in the reciprocal space.

Analogous to the *Bravais lattice*, any reciprocal space vector can be decomposed as a linear combination of primitive reciprocal lattice vectors \mathbf{b}_i as

$$\mathbf{K}_m = m_1\mathbf{b}_1 + m_2\mathbf{b}_2 + m_3\mathbf{b}_3. \quad (1.6)$$

The reciprocal vector \mathbf{K}_m exhibits the same translational periodicity as the *Bravais lattice*, meaning $e^{i\mathbf{k}_m\cdot(\mathbf{r}+\mathbf{R}_n)} = e^{i\mathbf{k}_m\cdot\mathbf{r}}$, which leads to the ortho-normality relation, $\mathbf{k}_m \cdot \mathbf{R}_n = 2\pi n$, equivalent to $\mathbf{a}_i \cdot \mathbf{b}_j = 2\pi\delta_{ij}$. The primitive reciprocal lattice vectors can then be determined as

$$\mathbf{b}_1 = \frac{2\pi}{V_{\text{cell}}} \mathbf{a}_2 \times \mathbf{a}_3, \quad \mathbf{b}_2 = \frac{2\pi}{V_{\text{cell}}} \mathbf{a}_3 \times \mathbf{a}_1, \quad \mathbf{b}_3 = \frac{2\pi}{V_{\text{cell}}} \mathbf{a}_1 \times \mathbf{a}_2 \quad (1.7)$$

where $V_{\text{cell}} = \mathbf{a}_1 \cdot (\mathbf{a}_2 \times \mathbf{a}_3)$ corresponds to the volume of the unit cell.

1.1.1 Symmetry constraints on the electronic structure

The crystal symmetries play a fundamental role in describing a material's electronic properties, as they dictate the way in which the electronic wavefunctions ψ_{nk} behave in the momentum-space.

In the simplest scenario, neglecting exchange and spin-orbit coupling effects, the full symmetry group of the single-electron Hamiltonian,

$$\mathcal{H} = \frac{\mathbf{p}^2}{2m} + V(\mathbf{r}),$$

belong to one of the 230 *crystallographic space groups* (SGs), whose elements are of the form $\{R|\tau\}$, with R a point group operator and τ a fractional translation operator.

An important intrinsic interaction that must be considered to properly describe the electronic structure of crystalline materials is the spin-orbit coupling (SOC), a relativistic interaction that arises from the orbital motion of the electron within the

atomic potential. This orbital motion generates an effective magnetic field, $\mathbf{B} = -\mathbf{v}/c \times \mathbf{E}$, which then interacts with the electron's spin, resulting in the spin-orbit coupling interaction.

The single-electron Hamiltonian including SOC effects can be expressed as,

$$\mathcal{H}(\mathbf{r}) = \frac{\mathbf{p}^2}{2m} + V(\mathbf{r}) + \frac{1}{2m^2c^2} (\nabla V(\mathbf{r}) \times \mathbf{p}) \cdot \boldsymbol{\sigma}, \quad (1.8)$$

where the last term represents the spin-orbit coupling contribution. The symmetries of this Hamiltonian are described by the *double space groups* (DSGs), whose symmetry elements are applied simultaneously on both the lattice and the spin degrees of freedom [82, 83].

1.2 Magnetic materials: A symmetry perspective

For crystals with local magnetic moments, the single-electron Hamiltonian ignoring SOC effects is given by

$$\mathcal{H}(\mathbf{r}) = \frac{\mathbf{p}^2}{2m} + V(\mathbf{r}) + S(\mathbf{r}) \cdot \boldsymbol{\sigma}. \quad (1.9)$$

Here, the exchange-interaction term $\mathcal{H}_{\text{mag}} = S(\mathbf{r}) \cdot \boldsymbol{\sigma}$ captures the interaction between the local magnetic moments and the electron's spin. $S(\mathbf{r})$ denotes the magnetic field generated by the local magnetic moments. The symmetries of this Hamiltonian are described by the *spin space groups* (SSGs) [53, 54], whose elements simultaneously applied on the spin and lattice, can be different.

However, when SOC is taken into account:

$$\mathcal{H}(\mathbf{r}) = \frac{\mathbf{p}^2}{2m} + V(\mathbf{r}) + S(\mathbf{r}) \cdot \boldsymbol{\sigma} + \frac{1}{2m^2c^2} (\nabla V(\mathbf{r}) \times \mathbf{p}) \cdot \boldsymbol{\sigma}. \quad (1.10)$$

In this case, the symmetry operations are instead described by the 1651 *magnetic space groups* (MSGs) [81, 84] that extend the conventional space groups to include magnetic order by introducing an additional antiunitary operator, the time-reversal symmetry \mathcal{T} .

1.2.1 Magnetic space groups

A magnetic space group, denoted as \mathcal{M} , is a finite group of symmetry operators of the form $\{R|\tau\}$, similar notation than *space groups*. However, these operators transform not only the lattice but also the spins. There 1651 MSGs extend the conventional 230 *crystallographic space groups* by incorporating symmetry transformations combined with time-reversal \mathcal{T} symmetry. This new operator plays the role of reversing the spin directions and reversing as well the momentum vector.

Time reversal symmetry

The *time reversal* operator in principle acts by reversing the direction of time t into $-t$, which is equivalent to reversing all the velocities of a system. Two important properties of \mathcal{T} are, *commutation* with the Hamiltonian as long as it does not include magnetic order, $[\mathcal{T}, \mathcal{H}] = 0$, and its nature as an *antiunitary* operator, meaning $\mathcal{T}\mathcal{T}^\dagger = -\mathbb{1}$.

When neglecting the spin or treating it as *scalar*, $\mathcal{T} = \mathcal{K}$, with \mathcal{K} denoting the complex conjugation operator. In this case, \mathcal{T} reverses only the momentum $\mathbf{k} \rightarrow -\mathbf{k}$ in the reciprocal space. However, when SOC is included, $\mathcal{T} = \mathcal{K}\sigma_y$, with σ_y a Pauli matrix operator. Here, \mathcal{T} not only reverses the momentum $\mathbf{k} \rightarrow -\mathbf{k}$, but also the spin, $\boldsymbol{\sigma} \rightarrow -\boldsymbol{\sigma}$ in momentum-space.

Type	Magnetic space group
\mathcal{M}_I	\mathcal{G}
\mathcal{M}_{II}	$\mathcal{G} + \mathcal{T}\mathcal{G}$
\mathcal{M}_{III}	$\mathcal{H} + \mathcal{T}(\mathcal{G} - \mathcal{H})$
\mathcal{M}_{IV}	$\mathcal{G} + \mathcal{T}\tau\mathcal{G}$

Table 1.1: **Table of Magnetic Space Group Types:** The first column indicates the type of magnetic space group. The second column presents the corresponding notation, where \mathcal{G} denotes the parent crystallographic space group, and \mathcal{H} represents its halving subgroup.

MSGs are classified into four types based on the role of \mathcal{T} , see Table 1.1. \mathcal{M}_I does not contain \mathcal{T} as a group element itself and corresponds to the conventional crystallographic 230 space groups. This group describes ferromagnetic and antiferromagnetic materials. \mathcal{M}_{II} includes \mathcal{T} as a point symmetry in real-space, therefore it typically describes paramagnetic and diamagnetic materials. \mathcal{M}_{III} is constructed as the halving subgroup \mathcal{H} of \mathcal{G} and the remaining half elements $\mathcal{G} - \mathcal{H}$ combined with \mathcal{T} . Since the complement set $\mathcal{G} - \mathcal{H}$ is not a group itself, \mathcal{T} is broken in real-space. This group is suited to magnetic materials with a variety of spin orderings, an example is the collinear order of EuIn_2As_2 , shown in Fig. 1.1(b). The non-magnetic and magnetic unit cell within this group have the same dimensions. Finally, \mathcal{M}_{IV} is constructed by connecting opposite spin sublattices by the non-symmorphic time-reversal symmetry $\mathcal{T}\tau$. It applies exclusively to compensated magnets, however not all compensated magnets are Type IV. An example of Type IV MSG is the collinear EuCd_2As_2 , shown in Fig. 1.1(a), where the magnetic unit cell doubles the non-magnetic one.

Kramer spin-degeneracy

It was long assumed, that, without SOC, collinear magnets with compensated magnetic order exhibit a spin-degenerate electronic structure across the entire momentum-space.

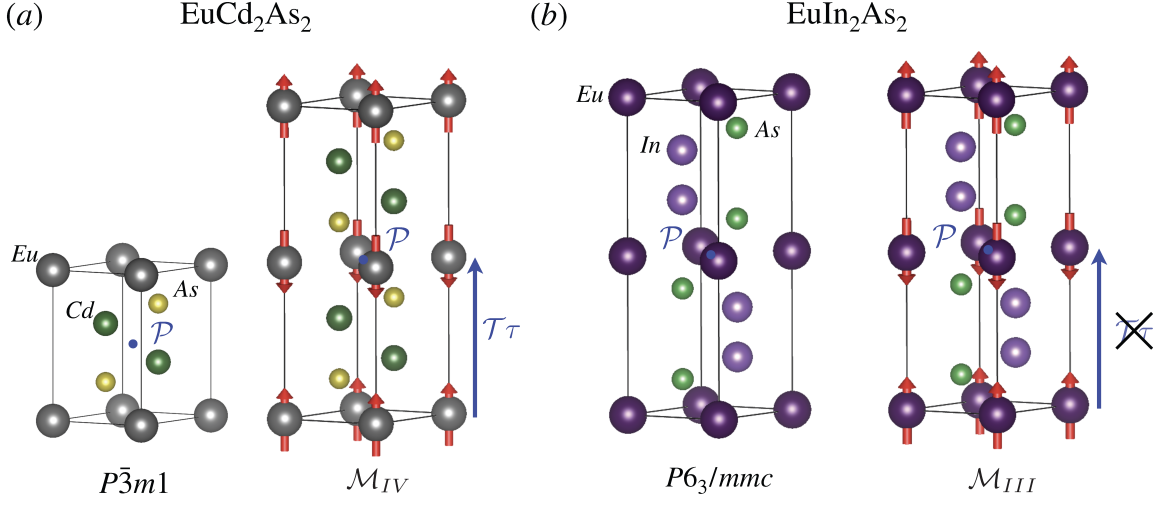


Figure 1.1: Non-magnetic (left) and collinear compensated (right) unit cells of tetragonal compounds (a) EuCd_2As_2 and (b) EuIn_2As_2 are shown with their respective space groups indicated below. Although both materials seem to share similar composition and magnetism, the position of their non-magnetic atoms are different, resulting in distinct space groups. The opposite spin-sublattices in EuCd_2As_2 are connected by $\mathcal{T}\tau$, whereas in EuIn_2As_2 $\mathcal{T}\tau$ is broken.

While this holds true for some collinear magnets, such as CuMnAs [15, 21], it doesn't apply for others like MnTe [56]. This spin-degeneracy, often referred to as *Kramers degeneracy*, is protected by combined symmetries \mathcal{PT} or $\mathcal{PT}\tau$, and it remains even in the presence of spin-orbit coupling.

Proof: Given a state $\phi_{\mathbf{k}}$ with energy $E_{\mathbf{k}}$. If the corresponding Hamiltonian is invariant under \mathcal{PT} symmetry, then $[H_{\mathbf{k}}, \mathcal{PT}] = 0$. Consequently,

$$H_{\mathbf{k}}\phi_{\mathbf{k}} = H_{\mathbf{k}}\mathcal{PT}\psi_{\mathbf{k}} = \mathcal{P}T H_{\mathbf{k}}\psi_{\mathbf{k}} = E_{\mathbf{k}}\phi_{\mathbf{k}}, \quad (1.11)$$

resulting in $\phi_{\mathbf{k}}$ an eigenstate with the same energy as $\psi_{\mathbf{k}}$, being $E_{\mathbf{k}}$. Now, we only need to prove that $\phi_{\mathbf{k}}$ and $\psi_{\mathbf{k}}$ are orthogonal. Since \mathcal{PT} is antiunitary, it holds $(\mathcal{PT})^2 = -1$,

$$\langle \phi_{\mathbf{k}}, \psi_{\mathbf{k}} \rangle = -\langle \mathcal{PT}\psi_{\mathbf{k}}, \mathcal{PT}\phi_{\mathbf{k}} \rangle = -\langle \psi_{\mathbf{k}}, \phi_{\mathbf{k}} \rangle^* = -\langle \phi_{\mathbf{k}}, \psi_{\mathbf{k}} \rangle, \quad (1.12)$$

then $\langle \phi_{\mathbf{k}} | \psi_{\mathbf{k}} \rangle = 0$, indicating the states $\psi_{\mathbf{k}}$ and $\phi_{\mathbf{k}}$ are degenerate states for any \mathbf{k} vector. q.e.d.

The electronic structure of collinear compensated EuCd_2As_2 will exhibit Kramers spin-degeneracy as it preserves the $\mathcal{PT}\tau$ symmetry. In contrast, the collinear compensated EuIn_2As_2 preserves only the spatial inversion \mathcal{P} symmetry, while breaking \mathcal{T} symmetry, meaning spin-split bands are allowed. Recent studies [10, 56, 57] have shown that *spin space groups* provide a more suitable framework than magnetic space groups for describing the spin-split bands of compensated magnets with broken \mathcal{PT}

symmetry.

1.2.2 Spin space groups

Spin space groups (SSGs), denoted as \mathcal{G}_s , have been theoretically formulated by Litvin in the 1970s [53, 54], their group elements are represented as pairs of transformations $[s_i||g_i|\tau]$, where s_i acts exclusively on the spin-space and $\{g_i|\tau\}$ acts exclusively on the real-space. Both operators can be proper or improper rotations, and they can have different rotation axes and angles.

A full spin space group can be decomposed as a direct product between the spin-only group \mathbf{r}_{so} and the non-trivial spin space group \mathbf{G}_s [53],

$$\mathcal{G}_s = \mathbf{r}_{\text{so}} \times \mathbf{G}_s. \quad (1.13)$$

This decomposition is done in such a way that \mathbf{G}_s consist solely of unitary symmetry operators, whereas by construction \mathbf{r}_{so} includes the antiunitary operators and pure spin transformations of the form $[R||E|\mathbf{0}]$, which involve no translation.

Spin-only group

In non-magnetic crystals, the absence of any spin-dependent term in the Hamiltonian leads to define the spin-only group as

$$\mathbf{r}_{\text{so}}^{\text{non}} = \text{SO}(3) \times \mathbb{Z}_2^T, \quad (1.14)$$

where $\text{SO}(3)$ represents the group of all continuous spin-space rotations, and $\mathbb{Z}_2^{C_{2\perp}\mathcal{T}} = \{[E||E], [\mathcal{T}||\mathcal{T}]\}$ contains the identity and the time-reversal operation.

In magnetically ordered crystals, the spin-only group depends exclusively on the spin arrangement type [53]. For collinear spin arrangements, where all the spins are aligned either parallel or antiparallel, the spin-only group,

$$\mathbf{r}_{\text{so}}^{\text{coll}} = \text{SO}(2) \rtimes \mathbb{Z}_2^{C_{2\perp}\mathcal{T}} \quad (1.15)$$

is expressed as the semidirect product between $\text{SO}(2) = [\mathbf{C}_\infty||E]$ the group of continuous spin rotations around the collinearity axis, and the group $\mathbb{Z}_2^{C_{2\perp}\mathcal{T}} = \{[E||E], [C_{2\perp}\mathcal{T}||\mathcal{T}]\}$. Here, $C_{2\perp}$ represents a two-fold spin rotation around any axis perpendicular to the axis of collinearity. In collinear magnets, the spin-only group acts effectively as inversion on the electronic structure, forcing centrosymmetric bands, even in non-centrosymmetric crystals. Similarly, it enforces even-parity spin polarization $S(\mathbf{k}) = S(-\mathbf{k})$, which effectively breaks \mathcal{T} in momentum-space – unless Kramers spin degeneracy is enforced, in which case \mathcal{T} is preserved.

In collinear magnets, $\mathbf{r}_{\text{so}}^{\text{coll}}$ enforces an even-parity order of the spin polarization, $S(\mathbf{k}) = S(-\mathbf{k})$, leading to the \mathcal{T} symmetry-breaking of the electronic structure in momentum-space.

In contrast, for non-collinear spin arrangements, the absence of a common spin quantization axis breaks $SO(2)$ symmetry. Consequently, the spin-only group in the coplanar case is reduced to

$$\mathbf{r}_{\text{so}}^{\text{cop}} = \mathbb{Z}_2^{C_{2\perp}\mathcal{T}}. \quad (1.16)$$

Here, $C_{2\perp}$ represents a two-fold rotation around the axis perpendicular to the coplanar spins. As the spin is treated as a 3D vector in the non-collinear case, $\mathbf{S} = (S_x, S_y, S_z)$, the spin-only group $\mathbf{r}_{\text{so}}^{\text{cop}}$ alone enforces an odd-parity (antisymmetric in momentum reversal $\mathbf{k} \rightarrow -\mathbf{k}$) spin polarization for the out-of-plane spin component $S_{\perp}(\mathbf{k}) = -S_{\perp}(-\mathbf{k})$, and an even-parity (symmetric in momentum-reversal) spin polarization for the in-plane spin components $S_{\parallel}(\mathbf{k}) = S_{\parallel}(-\mathbf{k})$. For the non-coplanar case, \mathbf{r}_{so} corresponds to the trivial group $\{E\}$, composed of only the identity operator.

Spin translation group

The normal subgroup $\mathbf{b} \subset \mathbf{B}$ is commonly referred to as the spin translation group [85] and just like the spin-only group, it plays an important role on imposing certain characteristics on the electronic structure. In collinear systems, \mathbf{b} corresponds to the trivial group only in the case of ferromagnets, altermagnets and \mathcal{PT} antiferromagnets [57]. However, for $\mathcal{T}\tau$ antiferromagnets, $\mathbf{b} = \{[E||E], [C_2||E]\}$, and it imposes the Kramers spin degeneracy over the entire momentum-space.

In non-collinear coplanar systems, \mathbf{b} enforces the vanishing of the in-plane spin polarization of the electronic structure, i.e., $\langle S_{\parallel} \rangle = 0$. Interestingly, this effect enforces a collinear spin polarization in momentum-space arising from a system with a non-collinear coplanar spin arrangement in the real-space. A notable example of this phenomenon, are the recently discovered p-wave magnets [63, 80], a class of $\mathcal{T}\tau$ -symmetric and \mathcal{PT} -symmetry-breaking materials exhibiting an odd-parity-wave magnetism. In this particular case, the antisymmetric spin ordering of the electronic structure is enforced by the combined spin-only group $\mathbf{r}_{\text{so}}^{\text{cop}}$ and the spin translation group \mathbf{b} , which results in the antiunitary $[\mathcal{T}||\mathcal{T}|\tau]$ symmetry that enforces a \mathcal{T} -symmetric electronic structure for all spin components, $\mathbf{S}(\mathbf{k}) = -\mathbf{S}(-\mathbf{k})$, even when including SOC. An important distinction from even-parity-wave magnets, is that odd-parity ones exhibit a p- or f-wave anisotropy (one or three spin un-polarized nodal planes), and they do preserve \mathcal{T} symmetry in momentum-space.

Non-trivial point group \mathbf{R}_s

If we neglect the translations of the non-trivial spin space group \mathbf{G}_s , the new elements $[s_i||g_i]$ define the non-trivial spin point group \mathbf{R}_s . The set of all g_i elements constitute the point group \mathbf{G} , and the set of all s_i elements constitute the point group \mathbf{B} . To construct the non-trivial spin point group \mathbf{R}_s that belongs to the family of \mathbf{G} and \mathbf{B} , one first needs to select two normal subgroups, $\mathbf{r} \subset \mathbf{G}$ and $\mathbf{b} \subset \mathbf{B}$ such that the quotient groups \mathbf{G}/\mathbf{r} and \mathbf{B}/\mathbf{b} are isomorphic between each other [53]. The normal subgroup \mathbf{r}

is composed of all right-hand terms of elements $[E||r]$ of \mathbf{R}_s , and \mathbf{b} is composed of all left-hand terms of elements $[b||E]$ of \mathbf{R}_s . We note, that the normal subgroup \mathbf{b} includes pure spin transformations combined with real-space translations, which differs from the spin-only group \mathbf{r}_{so} which involves no translations.

The groups \mathbf{G} and \mathbf{B} can be written as coset decomposition as,

$$\mathbf{G} = \mathbf{r} + G_2 \mathbf{r} + \cdots + G_n \mathbf{r}, \quad (1.17)$$

$$\mathbf{B} = \mathbf{b} + B_2 \mathbf{b} + \cdots + B_n \mathbf{b}. \quad (1.18)$$

Finally, by pairing each $B_i b$ term with $G_i r$ via the isomorphism $\mathbf{G}/\mathbf{r} \cong \mathbf{B}/\mathbf{b}$, the non-trivial spin point group \mathbf{R}_s is constructed as

$$\mathbf{R}_s = [\mathbf{b}||\mathbf{r}] + [B_2 \mathbf{b}||G_2 \mathbf{r}] + \cdots + [B_n \mathbf{b}||G_n \mathbf{r}]. \quad (1.19)$$

A complete list of all possible non-trivial spin point groups, for the specific case where \mathbf{b} is trivial, can be found in [54].

Classification of collinear magnets based on \mathbf{R}_s

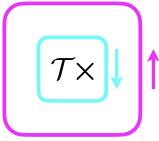
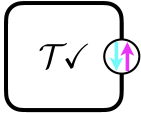
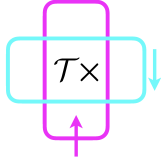
Ferromagnets	Antiferromagnets	Altermagnets
$\mathbf{R}_s^I = [E \mathbf{G}]$	$\mathbf{R}_s^{II} = [E \mathbf{G}] + [C_2 \mathbf{G}]$	$\mathbf{R}_s^{III} = [E \mathbf{H}] + [C_2 \mathbf{G} - \mathbf{H}]$
		

Table 1.2: **Non-relativistic collinear compensated magnetic phases.** The second row corresponds to the representation of non-trivial spin point groups for three distinct collinear phases, respectively. \mathbf{G} denotes the parent crystallographic point group, \mathbf{H} its halving point group and C_2 a two-fold spin rotation that flips the spin on the opposite direction. The third row display the energy iso-surfaces, indicating if time-reversal symmetry is protected or broken in the momentum-space.

The non-trivial spin point groups \mathbf{R}_s have been recently employed to classify collinear magnetic phases [56, 57], summarized in Table. 1.2. The group \mathbf{R}_s^I characterizes conventional ferromagnets, where the symmetries of the form $[E||\mathbf{G}]$ preserve the crystallographic point group symmetries and they do not impose spin-degeneracy at any k-point, resulting in a spin-split electronic structure featuring an isotropic s-wave order in the entire momentum-space. The second group \mathbf{R}_s^{II} characterizes conventional antiferromagnets (AFMs) where Kramers spin-degeneracy on the electronic structure is enforced by the spin symmetry $[C_2||E]$. This group includes collinear magnets with the opposite spin sublattices connected either by $[C_2||E|\tau]$ with τ a spatial translation or

by $[C_2||\bar{E}]$ with \bar{E} the real-space inversion. The antiferromagnetic EuCd_2As_2 belongs to the first case, while CuMnAs to the latter. Finally, the third class $\mathbf{R}_s^{\text{III}}$, corresponds to a new compensated magnetic phase called altermagnetism [56, 57]. In contrast to AFMs, the altermagnetic phase lifts the Kramers spin-degeneracy resulting in spin-split bands but not in the entire momentum-space. In this class, the subset $[E||\mathbf{H}]$ indicates only a subgroup of the crystallographic point group \mathbf{G} is preserved, resulting in an anisotropic spin-split electronic structure, featuring a d-, g-, or i-wave order, each of them indicating the number of spin-degenerate nodal planes 2, 4, and 6, respectively. The energy iso-surface of the altermagnet example, display a d-wave order, i.e., two nodal planes. The remaining set $[C_2||\mathbf{G} - \mathbf{H}]$ of $\mathbf{R}_s^{\text{III}}$ connects atoms between opposite spin-sublattices and protects the zero net magnetization. Notably, altermagnets combine characteristics typical of both conventional ferromagnets (spin-split bands) and antiferromagnets (compensated order). To date, several material candidates have been identified to host altermagnetism. Among the most prominent are RuO_2 [86, 87], Mn_5Si_3 [88], and $\text{KV}_2\text{Se}_2\text{O}$ [89] as d-wave AMs, and MnTe [90, 91] and CrSb [92, 93] as g-wave AMs.

Collinear g-wave altermagnet EuIn_2As_2

By determining the non-trivial spin point group \mathbf{R}_s of collinear compensated EuIn_2As_2 , we show that its spin-splittings exhibit a g-wave altermagnetic order. To determine \mathbf{R}_s , we first obtained the full set of spin space symmetry operations using the *spinspg* package [94]. By analyzing all the symmetry operators, we identified the point groups $\mathbf{G} = 6/mmm$, $\mathbf{B} = 2$, and the normal subgroups $\mathbf{r} = \bar{3}m$, and $\mathbf{b} = 1$ being the trivial group. We then express \mathbf{G} and \mathbf{B} as coset decompositions like in Eq. 1.17 and 1.18:

$$\begin{aligned}\mathbf{G} &= \bar{3}m + C_{6z} \bar{3}m, \\ \mathbf{B} &= E + C_2.\end{aligned}$$

From the pairing of each coset, we obtain \mathbf{R}_s :

$${}^2_6/{}^2m^2m^1m = [E||\bar{3}m] + [C_2||C_{6z} \bar{3}m] = [E||\mathbf{H}] + [C_2||\mathbf{G} - \mathbf{H}]. \quad (1.20)$$

The group name, based on Litvin's spin group notation [54], captures the information of the spin point group generators $[C_2||C_{6z}]$, $[C_2||m_z]$, $[C_2||m_x]$, and $[E||m_y]$. This group contains 24 elements. The second subset notation indicates the altermagnetic phase of this compound with a g-wave anisotropy characterized by four transposing mirror symmetries $[C_2||m_z]$, $[C_2||m_v]$, $[C_2||m_{v'}]$, and $[C_2||m_{v''}]$.

To conclude this section, we summarize the various symmetry frameworks relevant to characterize the Hamiltonians depending on the relative energy scales of the crystal field, exchange and spin-orbit coupling effects, as shown in Fig. 1.2. In magnetically

ordered systems, introducing SOC reduces the spin space group to the magnetic space group. Thus, SSGs can be a very valuable framework to isolate the effects arising exclusively from exchange and crystal fields. Notably, exchange-induced spin-splittings typically range from 100 meV to 1eV, which are generally larger than the spin-splittings induced by relativistic spin-orbit interaction, usually in the range of μeV to 100 meV.

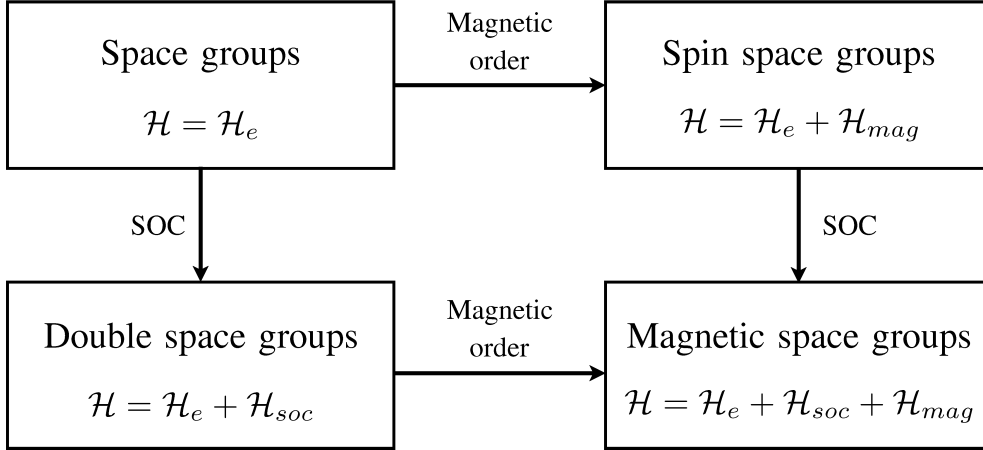


Figure 1.2: Diagram illustrating the appropriate symmetry formalisms to capture all symmetry operations of different single-electron Hamiltonians [55, 79].

1.3 Topological band theory

Over the past decade, topology has become one of the most active research areas in condensed matter physics, leading to the discovery of a wide variety of topological phases of matter. Remarkably, these phases not only provide a platform to explore high-energy physics phenomena [95], but their robustness against external perturbations also makes them attractive for potential applications in quantum computing [96, 97] and spintronics [12, 14].

Topology classifies phases of matter introducing an additional label known as *topological invariant*, a quantized index that captures global properties of the wavefunctions across the entire Brillouin zone. Unlike the theory of symmetry-breaking formulated by Landau [74], distinct topological phases of matter can preserve the same symmetries and have the same order parameter.

The concept of topological invariants was first introduced in the context of the quantum Hall effect, a phenomenon observed in a two-dimensional electron gas under a strong magnetic field [98], whose Hall conductivity $\sigma_{\text{AHC}} = Ce^2/h$ was found to be quantized, with the index C restricted to integer values. This index was later identified with the *Chern number*, a topological Berry-phase invariant associated with the Landau levels [99, 100].

In a 2D system, the Chern number of an entire band is defined as [101],

$$C_n = \frac{1}{2\pi} \int_{\text{BZ}} \Omega_n(\mathbf{k}) d^2k, \quad (1.21)$$

where $\Omega_n(\mathbf{k})$ is the *Berry curvature*, which can be obtained as $\Omega_n(\mathbf{k}) = \nabla_{\mathbf{k}} \times \mathbf{A}_n(\mathbf{k})$, with $\mathbf{A}_n(\mathbf{k})$ the *Berry connection*,

$$\mathbf{A}_n(\mathbf{k}) = \langle u_n(\mathbf{k}) | i \nabla_{\mathbf{k}} u_n(\mathbf{k}) \rangle. \quad (1.22)$$

Here, $|u_n(\mathbf{k})\rangle$ denotes the periodic part of the Bloch wavefunctions. Interestingly, the Berry curvature can be viewed as a fictitious magnetic field in momentum-space. Equation 1.21 evidence the connection between the topological invariant and the system's wavefunctions across the entire Brillouin zone.

In addition to evaluating the bulk topological invariant, the presence of gapless boundary states serves as a signature of non-trivial topology – phenomenon known as the *bulk-boundary correspondence* [102, 103]. These boundary states are robust as long as the symmetries that protect the bulk topological state are also preserved on the surface. In the following section, we will discuss the different classes of topological phases, their corresponding symmetry-based indicators and the key symmetries that protect these states.

1.3.1 Topological insulators

Topological insulators are materials that remain insulating in the bulk while supporting conducting electronic states at their gapless boundary states. A well-known example within this family is the 2D Chern insulator introduced by Haldane [75], whose chiral edge states, as illustrated in Fig. 1.3(a), are topologically protected by a non-zero bulk Chern number.

In general, two insulators belong to the same topological class as long as their corresponding Hamiltonians can be continuously deformed into one another without closing any energy band gap [101, 102, 104]. A strong indicator of possible non-trivial topology in an insulating band structure is the presence of *band inversion* around the band gap, as shown in Fig. 1.3(b), a phenomenon that often takes place due to strong spin-orbit coupling effects [105]. However, band inversion alone does not guarantee a non-trivial topology, to confirm the topological nature of a material, it is essential to compute the corresponding topological invariant.

The topological classification via the Chern number only applies to 2D spinless systems with broken time-reversal \mathcal{T} . By introducing the spin, Kane and Mele [76] introduced a new \mathbb{Z}_2 topological invariant for \mathcal{T} -invariant systems, such as non-magnetic materials. However, when inversion symmetry \mathcal{P} is also present – ensuring Kramers degenerate bands – the \mathbb{Z}_2 invariant can be further simplified and expressed in terms

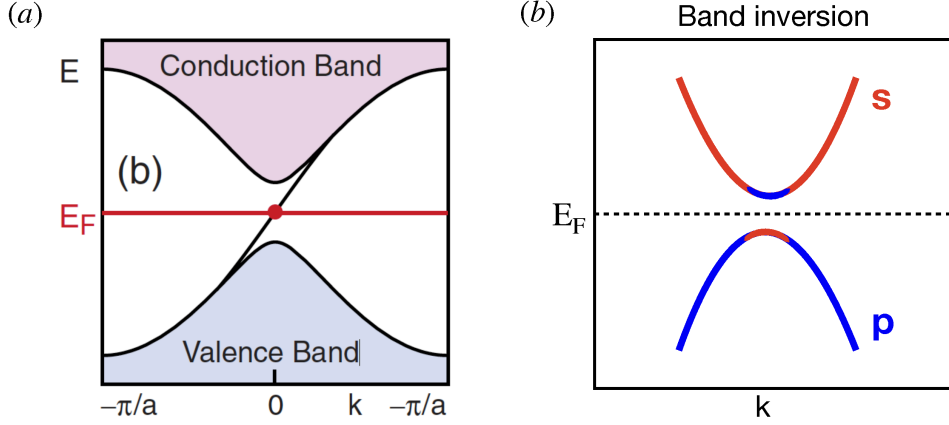


Figure 1.3: (a) Figure extracted from Ref. [102]: The electronic structure of a semi-infinite strip resulting from solving the Haldane model, illustrating a single edge state connecting the valence and conducting bands. (b) Schematics of the band inversion, showing the swapping of the s and p orbital characters.

of the parity eigenvalues [106],

$$(-1)^\nu = \prod_k^{\text{TRIM}} \prod_m^{N_{\text{occ}}/2} \xi_{nk}. \quad (1.23)$$

Here, ν denotes the \mathbb{Z}_2 invariant, k labels the time-reversal invariant momentum (TRIM) points in the Brillouin zone, m runs over the occupied pairs of Kramers degenerate bands, and $\xi_{nk} = \pm 1$ are the corresponding parity eigenvalues of the Kramers energy pairs. A value of $\nu = 1$ indicates a topological insulator with gapless surface states protected by \mathcal{T} symmetry, while $\nu = 0$ a trivial insulator.

In 3D systems with local magnetization, where \mathcal{T} is broken, non-trivial topological phases can still exist. While the breaking of \mathcal{T} no longer protects the surface states against disorder, some surface states may remain protected by additional crystalline symmetries, or they may become gapped, giving rise to a magnetoelectric effect [107].

Axion insulators

An axion insulator is a 3D topological insulator characterized by the presence of a quantized magnetoelectric response with an effective action of the form [18, 19, 107, 108],

$$S_\theta = \frac{\theta e^2}{4\pi^2 \hbar c} \int d\mathbf{r} dt \mathbf{E} \cdot \mathbf{B}, \quad (1.24)$$

where \mathbf{E} and \mathbf{B} are external electric and magnetic fields, e the electron charge, c the speed of light, and the index θ the axion angle. This index mimics the axion field introduced to solve the strong charge-parity problem in the context of quantum chromodynamics [109]. Remarkably, the axion, widely regarded as a potential dark

matter candidate, has not yet been experimentally detected. Axion insulators therefore offer a promising platform for its detection [18, 110].

The term $\mathbf{E} \cdot \mathbf{B}$ is odd under time-reversal symmetry, the combined $\mathcal{T}\tau$, inversion, and mirror symmetries, transforming as $\mathbf{E} \cdot \mathbf{B} \rightarrow -\mathbf{E} \cdot \mathbf{B}$. To preserve the invariance of the action S_θ under these symmetries, the condition $\theta \rightarrow -\theta$ must be satisfied, which enforces θ to be quantized: $\theta = 0$ for trivial insulators, and $\theta = \pi$ for axion insulators [19, 107].

In addition to the condition $\theta = \pi$, a characteristic feature of axion insulators is the presence of a half-quantized anomalous Hall conductivity (AHC), $\pm e^2/2h$, arising exclusively in the gapped surface states [108]. The initial search for axion insulators began in \mathcal{T} -invariant systems, where \mathcal{T} -symmetry-breaking perturbation were required to gap the otherwise gapless surface states [111].

Magnetic centrosymmetric systems instead provide a more convenient platform for realizing the axion insulator phase, since \mathcal{T} is broken by the local magnetization, and gapped surface states can exist intrinsically without the need for additional perturbations [112]. In the absence of \mathcal{T} but preserving inversion \mathcal{P} symmetry, the axion angle θ can be reduced to a parity-based invariant $\mathbb{Z}_4 = 0, 2$, defined as [113],

$$\mathbb{Z}_4 = \sum_k^{\text{TRIM}} \frac{n_k^- - n_k^+}{2} \text{ mod } 4, \quad (1.25)$$

where $n(k)^\pm$ are the occupied states with even/odd parity eigenvalues at the time-reversal invariant momentum (TRIM) points in the Brillouin zone. A value of $\mathbb{Z}_4 = 2$ corresponds to an axion insulator, while $\mathbb{Z}_4 = 0$ indicates a trivial insulator.

Topological crystalline insulators

Topological crystalline insulators (TCIs) constitute a class of topological phases of matter in which crystalline symmetries determine the bulk topology and, consequently, protect the conducting surface states [114, 115].

In the presence of mirror symmetry, one can define the topological invariant known as the *mirror Chern number* [114, 116]. Within the 2D mirror-symmetric plane, it is given by

$$n_M = \frac{n_{+i} - n_{-i}}{2}, \quad (1.26)$$

where $n_{\pm i}$ denotes the Chern numbers of the occupied bands with mirror eigenvalues $\pm i$. A non-zero mirror Chern number indicates the existence of protected surface states, manifesting as gapless Dirac cones located on surfaces that preserve the mirror symmetry, otherwise the surface states will be fully gapped.

These metallic surface states protected by crystalline symmetries have shown to exhibit high tunability under external electric fields [117] and applied strains [118–120]. Such control opens a pathway towards potential applications like topological

transistors in which conduction can be switched on and off by externally tuning the crystalline symmetry.

Higher-order topological insulators

Higher-order topological insulators (HOTIs) represent a topological phase in which boundary states are localized at hinges or corners rather than on surfaces, giving rise to lower-dimensional modes protected by the non-trivial bulk topology [121–124].

Hinge states can be chiral, meaning they can propagate unidirectionally, similar to the conducting edge states in 2D Chern insulators, \mathcal{T} -symmetry-breaking systems. Such modes propagate at the interface between two gapped surfaces with opposite mass terms [107]. They have been predicted in axion insulators [111, 125], including the compensated EuIn₂As₂ [25], and the ferromagnetic Sm-doped Bi₂Se₃ [126].

In contrast, helical hinge states consist of Kramers pairs of counterpropagating modes, analogous to the 2D Kane-Mele model [76] of the quantum spin Hall effect in \mathcal{T} -symmetric systems. The first material candidate where the HOTI phase was stabilized under uni-axial strain was the topological crystalline insulator SnTe [123].

Chiral hinge states are specially attractive for device applications, as they provide one-dimensional, dissipationless robust current channels [127]. When both surface and hinge states are gapped, the non-trivial bulk topology can still manifest in the form of corner states carrying fractional charge [121].

1.3.2 Weyl and Dirac semimetals

Topological semimetals constitute a class of quantum materials in which the bulk electronic spectrum is fully gapped along the entire Brillouin zone, as in conventional insulators, except at one or a few isolated points, lines, or planes where the valence and conduction bands touch near the Fermi level.

The Weyl semimetal phase is characterized by twofold-degenerate band touching points in momentum-space, known as *Weyl points*. In their vicinity, the energy dispersion is linear and can be captured by the effective Hamiltonian [128, 129],

$$\mathcal{H}_W(\mathbf{k}) = \pm \hbar v_F \mathbf{k} \cdot \boldsymbol{\sigma}. \quad (1.27)$$

where v_F denotes the Fermi velocity and $\boldsymbol{\sigma}$ is the vector of Pauli matrices. This Hamiltonian describes Weyl points in a crystal, in analogy with the massless relativistic Weyl fermions with right-handed (+) or left-handed (−) chirality.

Weyl points can be viewed as effective monopole sources of Berry curvature in momentum-space. Their non-trivial topology is characterized in analogous way to the Chern number defined in Eq. 1.21, but with the integration performed over a closed surface enclosing the Weyl point rather than the entire Brillouin zone. The corresponding topological invariant takes quantized values of ± 1 , defining the chirality

of the Weyl point [130]. Due to periodicity, the net Berry flux integrated over the entire Brillouin zone must vanish, that is, the total Chern number is zero. Consequently, Weyl points always come in pairs with opposite chirality and can only be created or annihilated in pairs. They can generally occur in momentum-space as long as the \mathcal{P} , or \mathcal{T} , or both are broken. A feature of the non-trivial bulk topology in Weyl semimetals is the emergence of Fermi arcs connecting the surface projections of Weyl points with opposite chirality [131].

Material realization of the Weyl semimetal phase include non-collinear compensated magnets [23, 131], noncentrosymmetric non-magnetic crystals [132] and ferromagnetic systems [133, 134]. In addition, more recently, spin-polarized Weyl points and Fermi arcs have been reported in altermagnets [135, 136].

The Dirac semimetal phase is characterized by fourfold-degenerate band touching points, known as *Dirac points*, around which the energy spectrum exhibits a linear dispersion [137, 138]. Such a phase requires the presence of Kramers degeneracy to ensure the double degeneracy of the bands. The emergence of a Dirac point in momentum-space can be described using the following 4×4 Hamiltonian [128, 129, 139]

$$\mathcal{H}_D(\mathbf{k}) = \begin{pmatrix} \hbar v_F \mathbf{k} \cdot \boldsymbol{\sigma} & m \\ m & -\hbar v_F \mathbf{k} \cdot \boldsymbol{\sigma} \end{pmatrix}, \quad (1.28)$$

where \mathbf{k} is measured with respect to the location of the Dirac point, $\pm \hbar v_F \mathbf{k} \cdot \boldsymbol{\sigma}$ describing two Weyl points with opposite chirality, and m the mass term. For $m = 0$, the Hamiltonian describes the Dirac point, in analogy with the relativistic massless Dirac equation, and it can be viewed as the overlapping of two Weyl points with opposite chirality, hence by breaking either inversion \mathcal{P} or \mathcal{T} symmetry could lead to the Weyl semimetal phase. It is important to note that the Chern number associated with the Dirac point is zero, indicating it is not topologically protected in the same way as the Weyl points.

While accidental Dirac points can appear at quantum critical points, they are typically unstable. Nevertheless, stable and symmetry-protected Dirac points can exist if additional crystalline symmetries are present, such as non-symmorphic [15, 21, 140] or rotational symmetries [138, 141]. A general classification of stable 3D Dirac semimetals in non-magnetic systems with rotational symmetries was first proposed by Yang and Nagaosa [138], an analogue classification for magnetic systems was later proposed by Hua G. et.al. [39]. Both frameworks identify two classes of Dirac points: The first class with pair of Dirac points along the rotation axis and away the time reversal invariant momentum points (TRIM). They typically arise from band inversion when conduction and valence bands belong to different irreducible representation of the symmetry line, preventing hybridization. Within this class, double Fermi arcs at the surface connecting the projected Dirac nodes are a clear signature of its non-trivial topology in the bulk. Furthermore, the second class allows only a single Dirac point appearing exactly

at a TRIM point on the rotation axis [137].

The first experimental realization of 3D stable DPs belong to the first class and were reported in the non-magnetic Na_3Bi [142–144] and Cd_3As_2 [145] compounds. Within amgnetic materials, only systems with compensated magnetic order have so far been found to host the Dirac semimetal phase. Notable examples include the \mathcal{PT} -symmetric Type III MSG compound CuMnAs [15], and the $\mathcal{PT}\tau$ -symmetric Type IV MSG EuCd_2As_2 [24, 39].

Dirac semimetals – specially those in compensated magnets – offer a platform for device applications, since their zero net magnetization can enable manipulation of the Dirac fermions without generating stray magnetic fields. Prominent examples include the electric control of Dirac quasiparticles trough Néel vector reorientation [12, 21] and the realization of colossal magnetoresistance [146, 147].

1.3.3 Magnetic topological quantum chemistry

Magnetic topological quantum chemistry (MTQC) provides a complete theory of band topology and symmetry-based indicators for crystals with comme-surate magnetic order [29]. Within this theory one can derive for every magnetic space group (MSG), the small corepresentations at high-symmetry k-points in the Brillouin zone (BZ), the elementary band corepresentations (EBRs), compatibility relations, and more, which are useful to identify trivial and topological states.

A set of energy bands in momentum-space that transform under a corepresentation of the MSG that originates from localized (magnetic) Wannier orbitals in real-space is called *magnetic band representation* (MBR). Because MSGs contain antiunitary symmetry operators (such as time-reversal combined with spatial symmetry operations), one must work with corepresentations instead of representations, which are exclusive to unitary operators. If a band corepresentation cannot be decomposed as a direct sum of other band corepresentations, it is called an *elementary* band corepresentation (EBR) [28]. In the MTQC framework, a set of EBRs forms a basis of trivial insulators. Thus, a stable topological insulator or topological semimetal corresponds to the case where its occupied bands cannot transform in a direct sum of magnetic EBRs, indicating that they are not adiabatically connected to an atomic insulator.

Next, we use the MTQC tools available on the Bilbao Crystallographic Server [148] to determine whether a pair of bands cross or are gapped along a high-symmetry k-path. In the following, we analyze into detail the electronic band structure of the antiferromagnetic EuCd_2As_2 with $\mathbf{N}||(\text{001})$ along the $\Gamma - A$ path, shown in Fig. 1.4(a), referred as case (a). First, we obtain the band corepresentations (coreps) of the magnetic little group at the Γ and A points using the code IrRep [83, 149]. The coreps of the selected bands near the Fermi level are $\bar{\Gamma}_8$ and $\bar{\Gamma}_6\bar{\Gamma}_7$ and \bar{A}_4 and \bar{A}_5 . Next, using the compatibility relations [29, 30], we relate the coreps at Γ and A :

$$\begin{aligned}
\bar{\Gamma}_6\bar{\Gamma}_7(2) &\rightarrow \bar{\Delta}_4\bar{\Delta}_5(2) \\
\bar{\Gamma}_8(2) &\rightarrow \bar{\Delta}_6(2) \\
\bar{A}_4(2) &\rightarrow \bar{\Delta}_4\bar{\Delta}_5(2) \\
\bar{A}_5(2) &\rightarrow \bar{\Delta}_6(2)
\end{aligned}$$

Here, Δ denotes any intermediate k-point between Γ and A . For example, the relation $\bar{\Gamma}_8 \rightarrow \bar{\Delta}_6$ indicates that the corep $\bar{\Gamma}_8$ at Γ is connected to the corep $\bar{\Delta}_6$ at Δ .

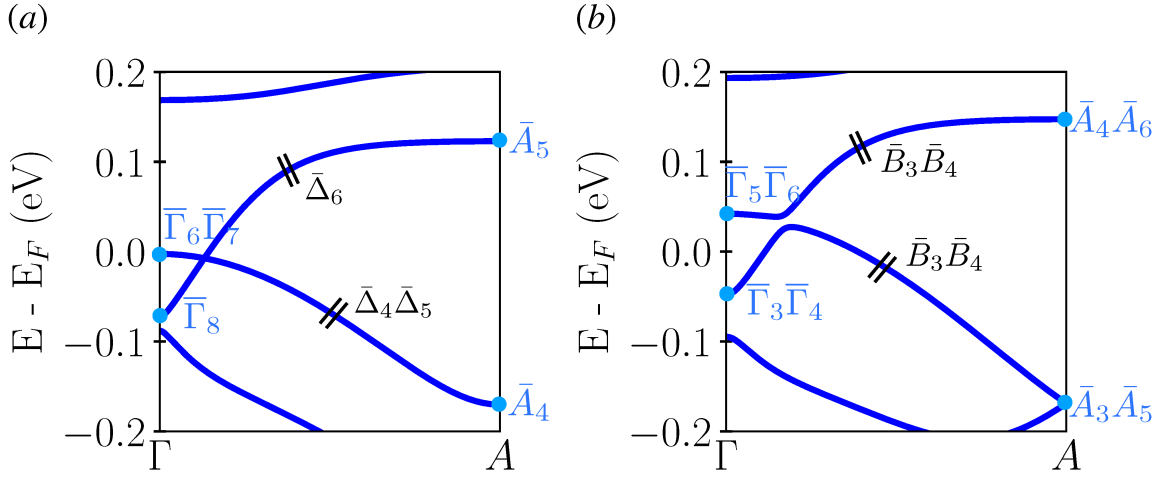


Figure 1.4: Band connectivity along the $\Gamma - A$ k-path via the compatibility relations for the (a) MSG $P_c\bar{3}c1$ (No. 165.96) corresponding to the antiferromagnetic EuCd_2As_2 with Néel vector orientation $\mathbf{N} \parallel (001)$, and the (b) MSG C_c2/m (No. 12.63) corresponding to $\mathbf{N} \parallel (100)$.

Along such a high-symmetry line, a band cannot change its corep. Thus, a band originating from $\bar{\Delta}_6$ at Γ cannot terminate in $\bar{\Delta}_4\bar{\Delta}_5$ at A . The possible band connectivities are shown in Fig. 1.4, where in case (a) a fourfold degenerate band crossing is symmetry-enforced, resulting in a *enforced semimetal*, whereas in case (b) the bands near the Fermi level at the intermediate k-point B transform as the same corepresentation $\bar{B}_3\bar{B}_4$, allowing a band gap.

1.4 Summary

In this chapter, we have introduced the fundamental concepts of symmetry and topology relevant to the study of topological phases of matter in magnetic materials. We began by discussing the different symmetry frameworks used to describe magnetic crystals, emphasizing the spin space group formalism, which allows us to isolate the effects arising exclusively from exchange and crystal fields. We then provided an overview of various topological phases, their corresponding topological invariants, the key symmetries that protect these states, and the magnetic topological quantum chemistry

framework, which offers a systematic approach to identify topological phases in crystals with commensurate magnetic order, important concepts which will be helpful for understanding Chapter 3.

Chapter 2

First principles electronic theory

"The power of simple models, the power of stripping things down — [Anderson] taught me the power of reducing everything to the simplest possible idea and following it to where it could go"

— Duncan Haldane

A microscopic understanding of the electronic structure of real materials – including metals, semiconductors and insulators – is essential not only for the interest of fundamental physics, but also for predicting unique responses relevant to technological applications and the development of next-generation devices. All real materials are inherently interacting many-body systems, and determining their actual electronic structure has long been considered a challenging task, as solving the associated Schrödinger equation involves an enormous Hilbert space and requires substantial computational resources.

A major breakthrough came in the mid-1960s when W. Kohn and L. J. Sham introduced "density functional theory" (DFT) [150, 151]. This innovative approach further simplified the problem, making it possible to access the ground-state properties of interacting electron systems by solely determining the electron density, which can be derived within an effective single-particle framework [152], thereby reducing significantly the computational costs. Nowadays, DFT has become the preferred method for predicting the electronic, magnetic and structural properties of real materials in material science and chemistry.

In this Chapter, we will present the theoretical foundation of DFT, its numerical implementation for collinear and non-collinear magnets. In addition, we will describe the Wannier interpolation technique that we use to construct effective Hamiltonians that we use for further post-processing to compute the surface states and Kubo linear responses.

2.1 Density functional theory

To understand the general formulation of DFT, we begin by introducing the many-body Hamiltonian that we aim to solve by using the Schrödinger equation. For simplicity, neglecting the spins, this Hamiltonian can be written as

$$\mathcal{H} = \sum_{\mu} \left(-\frac{\hbar^2}{2M_{\mu}} \nabla_{\mu}^2 + \sum_{\nu > \mu} V_I(R_{\mu} - R_{\nu}) \right) + \sum_i \left(-\frac{\hbar^2}{2m} \nabla_i^2 + \sum_{j > i} \frac{e^2}{|r_i - r_j|} + \sum_{\mu} V(r_i - R_{\mu}) \right).$$

The first set of brackets accounts for the nuclear contribution, including the kinetic energy of a nucleus with mass M_{μ} and the interaction between nuclei at positions R_{μ} and R_{ν} . The second set of brackets describes the electron gas, including the kinetic energy of an electron with mass m , the interaction between electrons and between electron at position r_i and nuclei at position R_{μ} . While solving this Hamiltonian might seem very challenging, additional approximations can simplify the problem, such as the Born-Oppenheimer approximation, or *adiabatic* approximation, that treats the nuclei as fixed atoms, based on the fact that they are much heavier and move significantly slower than the electrons. As a result, the kinetic contribution of the nuclei can be neglected, allowing us to solve only the electronic Hamiltonian:

$$\mathcal{H}^{\text{el}} = \sum_i \left(-\frac{\hbar^2}{2m} \nabla_i^2 + \sum_{j > i} \frac{e^2}{|r_i - r_j|} + \sum_{\mu} V_{\text{ion}}(r_i - R_{\mu}) \right). \quad (2.1)$$

Solving this electronic Hamiltonian within density-functional theory relies on two fundamental results. The Hohenberg Kohn theorem that states the ground-state energy of the Hamiltonian \mathcal{H}^{el} can be written as a functional of the electron density $n(\mathbf{r})$ [150]:

$$E[n] = T[n] + \int n(\mathbf{r}) V_{\text{ion}}(\mathbf{r}) d\mathbf{r} + \frac{1}{2} \int \int \frac{n(\mathbf{r})n(\mathbf{r}')}{|\mathbf{r} - \mathbf{r}'|} d\mathbf{r}d\mathbf{r}' + E_{\text{xc}}[n], \quad (2.2)$$

where $T[n]$ is the kinetic energy of the non-interacting electrons, the third term is the Hartree contribution that represents the Coulomb energy from the electronic cloud, and $E_{\text{xc}}[n]$ the exchange-correlation energy functional, which is generally unknown but can be approximated.

2.1.1 Non-relativistic Kohn-Sham equations

The second fundamental result of DFT is the mapping of a system of N interacting electrons onto an auxiliary system of fictitious N non-interacting electrons that, in most cases, reproduces the same ground-state electron density [152]. These single-particle

Schrödinger equations are known as the Kohn-Sham equations:

$$h|\psi_i\rangle = \left(-\frac{\hbar^2}{2m}\nabla^2 + V_{\text{eff}}(\mathbf{r})\right)|\psi_i\rangle = \varepsilon_i |\psi_i\rangle, \quad (2.3)$$

where $|\psi_i\rangle$ represents the single-particle wavefunction with eigenenergy ε_i . The total effective potential V_{eff} , in which the non-interacting electrons move is

$$V_{\text{eff}} = V_{\text{ion}} + \int \frac{n(\mathbf{r}')}{|\mathbf{r} - \mathbf{r}'|} d\mathbf{r}' + V_{\text{xc}}. \quad (2.4)$$

It combines the ionic potential, the classical Hartree potential (mean-field Coulomb interaction), and the exchange-correlation potential

$$V_{\text{xc}}(\mathbf{r}) = \frac{\delta E_{\text{xc}}[n]}{\delta n(\mathbf{r})}, \quad (2.5)$$

which incorporates the remaining many-body effects.

For non-magnetic materials where the spins are neglected, the electron density can be defined as follows:

$$n(\mathbf{r}) = \sum_i^N |\psi_i(\mathbf{r})|^2. \quad (2.6)$$

The Kohn-Sham equations provide a self-consistent algorithm for determining the ground-state energy of a many-electron system. The process begins with an initial guess for the electron density $n(\mathbf{r})$, from which one constructs the Kohn-Sham Hamiltonian and then solves it to obtain the new wavefunctions; these, in turn generate the new electron density for the next iteration. This cycle is repeated until the input and output densities converge within an specified tolerance.

Several codes implement DFT, differing mainly in the basis set used to represent the Kohn-Sham wavefunctions $|\psi_i\rangle$. In this work, we use the Vienna ab initio simulation package (VASP) [153, 154]. In Section 2.1.2 we discuss details of the specific approximations implemented in VASP to construct the effective potentials and the Kohn-Sham wavefunctions.

Collinear magnets

To incorporate spin polarization, we first consider the case of magnetic materials with *collinear* spin degrees of freedom. In collinear magnets, all spins share a common quantization axis, allowing the spin-up and spin-down subspaces to be treated independently. The electron density can then be defined as,

$$n(\mathbf{r}) = n_{\uparrow}(\mathbf{r}) + n_{\downarrow}(\mathbf{r}) = \sum_{\alpha} \sum_i^N |\psi_{i\alpha}(\mathbf{r})|^2, \quad (2.7)$$

where N is the total number of electrons, and $\alpha = \{\uparrow, \downarrow\}$ labels the two spin polarizations. In this framework, two independent sets of Kohn-Sham equations must be solved, one for each spin channel,

$$\left(-\frac{\hbar^2}{2m}\nabla^2 + V_{\text{eff}}[n_\alpha](\mathbf{r})\right)|\psi_{i,\alpha}\rangle = E_i |\psi_{i,\alpha}\rangle. \quad (2.8)$$

Noncollinear magnets

For non-collinear systems, a vector magnetization density is introduced within VASP [154]. The total electron density is then defined as

$$n_{\alpha\beta}(\mathbf{r}) = \left(\sum_{\alpha} n_{\alpha\alpha}(\mathbf{r}) \delta_{\alpha\beta} + \vec{m}(\mathbf{r}) \cdot \vec{\sigma}_{\alpha\beta}\right)/2, \quad (2.9)$$

where the part proportional to the unit matrix corresponds to the charge density and the term proportional to the vector of Pauli matrices $\vec{\sigma} = (\sigma_x, \sigma_y, \sigma_z)$ is the magnetization density $\vec{m}(\mathbf{r})$. The Pauli matrices are defined in ¹.

Constraint in the magnetization

Converging to a noncollinear magnetic configuration is often challenging, in some cases because such a configuration does not correspond to a minimum energy state or because of the intrinsic complexity of the spin arrangement. To help with the convergence, VASP incorporated an iterative method that imposes constraints on the magnetic moments [155]. In this approach, a penalty energy term E_p is added to the total energy functional $E = E_0 + E_p$, where E_0 is the usual DFT energy and the penalty energy,

$$E_p = \sum_{\mu} \lambda \left(|\mathbf{M}_{\mu}^F| - \hat{\mathbf{e}}_{\mu} \cdot \mathbf{M}_{\mu}^F \right). \quad (2.11)$$

with λ a Lagrange multiplier applied to each atomic site μ , $\hat{\mathbf{e}}_{\mu}$ a unit vector pointing in the direction of the desired magnetic moments, and \mathbf{M}_{μ}^F is the integrated magnetic moment of each atomic site, defined as

$$\mathbf{M}_{\mu}^F = \int_{\Omega_{\mu}} \vec{m}(\mathbf{r}) F_{\mu}(|\mathbf{r} - \mathbf{r}_{\mu}|) d\mathbf{r}, \quad (2.12)$$

where Ω_{μ} is a sphere of radius R_{μ} centered in the atom μ . Here, $\vec{m}(\mathbf{r})$ represents the magnetization density and F_{μ} is a normalized function that smoothly decays to zero at the boundary of the sphere Ω_{μ} . The sphere's radius R_{μ} is specified in VASP via the tag RWIGS, the Wigner-Seitz radii.

¹

$$\sigma_x = \begin{pmatrix} 0 & 1 \\ 1 & 0 \end{pmatrix}, \quad \sigma_y = \begin{pmatrix} 0 & -i \\ i & 0 \end{pmatrix}, \quad \sigma_z = \begin{pmatrix} 1 & 0 \\ 0 & -1 \end{pmatrix} \quad (2.10)$$

The penalty energy in Eq. 2.11 introduces an additional penalty potential in the Kohn-Sham equations,

$$V_\mu(\mathbf{r}) = 2\lambda \left(|\mathbf{M}_\mu^F| - \hat{\mathbf{e}}_\mu \cdot \mathbf{M}_\mu^F \right) F_\mu(|\mathbf{r} - \mathbf{r}_\mu|) \cdot \vec{\sigma}, \quad (2.13)$$

where $\vec{\sigma}$ is the vector of Pauli matrices.

As seen from Eq. 2.11 and 2.13, both the penalty energy and the corresponding potential vanish when each magnetic moments \mathbf{M}_μ^F is aligned with the target direction $\hat{\mathbf{e}}_\mu$. Furthermore, Ref. [155] demonstrates that the penalty energy term decreases with increasing λ according to,

$$E_p \propto 1/\lambda, \quad (2.14)$$

which underscores the importance of checking convergence with respect to λ until E_p falls below the electronic energy criterion used to for the DFT energy E_0 .

Figure. 2.1(a) illustrates such a convergence test for the electronic structure calculation of the helical EuIn_2As_2 , in which both the direction and the size of the magnetic moments were constrained. The results confirm the inverse proportionality between E_p and λ , in agreement with Eq. 2.14. Figure 2.1(b) further shows the simultaneous convergence of the total integrated magnetization towards the compensated state while increasing λ .

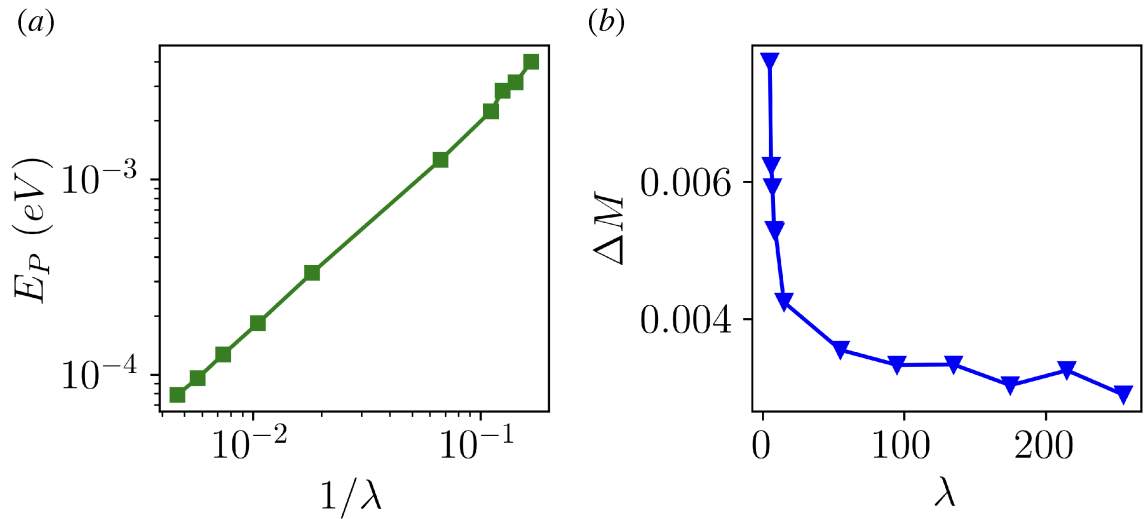


Figure 2.1: **Constraint on the magnetization in the electronic structure calculation of helical EuIn_2As_2 :** (a) Penalty energy as a function of $1/\lambda$. (b) Difference between the total integrated magnetization calculated in the unit cell and the desired compensated magnetization.

VASP provides three different schemes for constraining the magnetic moments. In the electronic structure calculations of EuIn_2As_2 presented in Chapter 4, we constraint only the direction of the magnetic moments, which led to a rapid convergence already

for small λ values.

2.1.2 Potential and wavefunction approximations

Generalized gradient approximation (GGA)

Several methods exist to treat the exchange–correlation effects within density functional theory (DFT) [156]. The most widely used approximation is the local density approximation (LDA) [152]:

$$E_{\text{xc}}^{\text{LDA}}[n] = \int n(\mathbf{r})\varepsilon_{\text{xc}}(n(\mathbf{r})) d\mathbf{r}, \quad (2.15)$$

where $\varepsilon_{\text{xc}}(n(\mathbf{r}))$ represents the exchange–correlation energy. In this approach, the inhomogeneous electron density is treated as a collection of infinitesimal regions with homogeneous density $n(\mathbf{r})$. LDA is particularly well suited for systems resembling a homogeneous electron gas, such as metals. For spin-polarized calculations, the local spin density approximation (LSDA) is used. It is evaluated in the same way as Eq. 2.15, except that the exchange–correlation energy $\varepsilon_{\text{xc}}(n_{\uparrow}(\mathbf{r}), n_{\downarrow}(\mathbf{r}))$ now depends on the spin-up and spin-down densities.

For systems with inhomogeneous charge distributions, the generalized gradient approximation (GGA) provides a better description, as it incorporates not only the local density $n(\mathbf{r})$ but also its spatial gradients $\nabla n(\mathbf{r})$:

$$E_{\text{xc}}^{\text{GGA}}(\mathbf{r}) = \int n(\mathbf{r}) \varepsilon_{\text{xc}}(n(\mathbf{r}), \nabla n(\mathbf{r})) d(\mathbf{r}), \quad (2.16)$$

Although GGA significantly improves upon LDA, it is known to substantially underestimate the band gaps of semiconductors and insulators [64]. We will use the Perdew Burke Ernzerhof (PBE) implementation of GGA [157] in VASP.

DFT + U approximation

While LDA and GGA provide an accurate description of itinerant systems, where the valence electrons are delocalized and their correlations are usually screened, they are inadequate for materials with partially filled d or f shells, in which electrons are more localized and strongly correlated. To account for the strong Coulomb repulsion in such systems, a Hubbard U correction is required. The generalized DFT+U energy functional is given by [158],

$$E^{\text{DFT+U}}[n, \hat{n}] = E^{\text{DFT}}[n] + E^{\text{U}}[\hat{n}] - E_{\text{dc}}[\hat{n}], \quad (2.17)$$

where n is the total electron density, and \hat{n} is the on-site occupation matrix of the localized d or f orbitals. The second term, E^{U} , represents the Hubbard correction derived within the mean-field Hartree-Fock approximation, and the last term, E_{dc} is

a double-counting energy term that removes the on-site Coulomb repulsion already included in the LDA/GGA exchange-correlation functional.

Different kinds of DFT+U exist, differing only on how the double-counting correction is treated [159, 160]. We adopt the rotationally invariant approach implemented by Dudarev et. al., [160], for which the DFT+U energy functional is,

$$E^{\text{DFT+U}} = E^{\text{DFT}} + \frac{(\bar{U} - \bar{J})}{2} \sum_{\sigma} \left(\sum_m n_{m,m}^{\sigma} - \sum_{m,m'} n_{m,m'}^{\sigma} n_{m',m}^{\sigma} \right), \quad (2.18)$$

where $n_{m,m'}^{\sigma}$ is the occupation matrix with the indices m, m' as the projections of the angular momentum (for a d orbital with $l = 3$, the projections $m, m' = \{-3, -2, -1, 0, 1, 2, 3\}$). In this method, the last term represents the double-counting correction, and it depends only on the difference $\bar{U} - \bar{J}$, with \bar{U} and \bar{J} are spherically averaged Coulomb and Hund's parameters.

When static localization no longer applies and dynamical charge or spin fluctuations dominate, more advanced methods such as the dynamical mean-field theory (DMFT) [161, 162] are more suitable.

Projected-augmented-wave method (PAW)

To solve the Kohn-Sham equations, besides approximating the exchange-correlation functional, it is necessary to select an appropriate basis set for the Kohn-Sham wavefunction $|\Psi_i\rangle$. Several approximations have been developed to represent this basis efficiently, aiming to recover the true one-electron Kohn-Sham wavefunction in the full Coulomb potential, referred as the all-electron wavefunction (AE).

For the simplest case of nearly free electrons in a weak periodic potential, the AE wavefunction can be expanded as a series of plane waves. However, since the potential varies sharply near the atomic nuclei as $1/r$, the wavefunction exhibits rapid oscillations inside these core regions, and an accurate plane-wave representation would require a large basis of plane waves. To overcome this difficulty, pseudopotential methods were developed in combination with a plane-wave basis set [163, 164], in which the potential inside a chosen cutoff radius r_c is replaced by a smoother pseudopotential with the same scattering properties. A corresponding pseudowavefunction $|\tilde{\psi}_i\rangle$ is constructed so that it exactly matches the AE wavefunction for $r > r_c$, while for $r < r_c$ it is smooth and nodeless and it satisfies a norm-conservation rule that enforces the integrated charge of $|\tilde{\psi}_i\rangle$ and the AE wavefunction within r_c are identical [164]. Vanderbilt later improved this method by relaxing this norm-conservation condition, allowing a lower plane-wave basis set and then reducing the computational cost, a method known as the ultrasoft pseudopotentials (USPP) [165]. However, constructing these pseudopotentials is a difficult task.

Blöchl has developed a simple method, called the projector augmented-wave method (PAW) [166, 167], in which the AE wavefunctions are derived from the pseudo (PS)

wavefunctions by a linear transformation:

$$|\psi_n\rangle = |\tilde{\psi}_n\rangle + \sum_i \left(|\phi_i\rangle - |\tilde{\phi}_i\rangle \right) \langle \tilde{p}_i | \tilde{\psi}_n \rangle, \quad (2.19)$$

where $|\tilde{\psi}_n\rangle$ and $|\tilde{\phi}_i\rangle$ are the PS wavefunction and partial wave. The AE partial wave is denoted by $|\phi_i\rangle$, and the projector functions $|\tilde{p}_i\rangle$ are constructed as

$$\langle \tilde{p}_i | \tilde{\phi}_j \rangle = \delta_{ij}. \quad (2.20)$$

Inside the PAW spheres enclosing the atomic sites, every (pseudo) AE wavefunction can be expanded into (pseudo) AE partial waves $\psi_n(\mathbf{r}) = \sum_i c_i |\phi_i\rangle$. The AE partial waves ϕ_i are defined as the solutions of the radial Schrödinger equation multiplied by spherical harmonics. Outside the spheres, the smooth pseudo-wavefunctions are already identical to the all-electron ones.

This method is currently implemented in VASP, more details are found in Ref. [167].

2.1.3 Relativistic Kohn-Sham equations

The inclusion of spin-orbit coupling (SOC) in VASP is carried out within the PAW framework [168]. As SOC acts predominantly in the close vicinity of the nuclei, its effects outside the PAW sphere can be neglected. Consequently, the SOC contribution to the Hamiltonian can be reduced to an AE one-center contribution:

$$\tilde{\mathcal{H}}_{\text{SOC}} = \sum_{ij} |p_i\rangle \langle \phi_i | H_{\text{SOC}} | \phi_j \rangle \langle p_j|. \quad (2.21)$$

The SOC operator $H_{\text{SOC}}^{\alpha\beta} \propto \vec{\sigma}^{\alpha\beta} \cdot \mathbf{L}$ couples the spin operator $\vec{\sigma} = (\sigma_x, \sigma_y, \sigma_z)$ to the angular momentum $\vec{L} = \vec{\mathbf{r}} \times \vec{\mathbf{p}}$.

In practice, VASP treats SOC employing two-component spinor wavefunctions $|\tilde{\psi}_n^\alpha\rangle$, allowing noncollinear spin densities. The action of the SOC operator on these spinors is evaluated as

$$|\tilde{\psi}_n^\alpha\rangle = \sum_{\alpha\beta} H_{\text{SOC}}^{\alpha\beta} |\tilde{\psi}_n^\beta\rangle, \quad (2.22)$$

where the indices α and β label the spin-up and spin-down components.

2.2 Wannier interpolation method

The Wannier interpolation method provides a powerful framework for constructing *maximally localized Wannier functions* (MLWFs) by projecting the Bloch wavefunctions obtained from DFT (or other *ab initio*) calculations onto a set of localized real-space basis [169–171]. Within this new localized basis, one can build an effective tight-binding Hamiltonian, which enables an efficient interpolation of both the electronic

band structure and wavefunctions onto a denser k-point mesh. Such interpolation technique is particularly useful for calculating transport responses that require a fine sampling of the Brillouin zone, such as the anomalous Hall conductivity or Boltzmann transport responses. In the following, we summarize the formalism as implemented in the Wannier90 package [169].

Once we obtain the eigenvalues $E_{n\mathbf{q}}$ and wavefunctions $\psi_{n\mathbf{q}}$ from the *ab initio* calculation on a coarse momentum-space q-mesh, we can construct a set of M Wannier functions per unit cell as

$$|\mathbf{R}n\rangle = \frac{V}{(2\pi)^3} \int_{\text{BZ}} d\mathbf{k} e^{-i\mathbf{q}\cdot\mathbf{R}} \sum_{m=1}^N U_{mn}(\mathbf{q}) |\psi_m(\mathbf{q})\rangle, \quad (2.23)$$

where $M \leq N$ with the number of Wannier functions being typically chosen to be smaller than the number of bands N , \mathbf{R} labels the lattice vectors. The integral is performed over the first Brillouin zone (BZ) with V as the volume of the unit cell. The matrix $U_{mn}(\mathbf{q})$ is a unitary matrix, which is iteratively refined by minimizing the total quadratic spread of the Wannier functions with respect to their centers,

$$\Omega = \sum_{n=1}^M \langle \mathbf{0}n | r^2 | \mathbf{0}n \rangle - \langle \mathbf{0}n | \mathbf{r} | \mathbf{0}n \rangle^2. \quad (2.24)$$

Using the localized Wannier functions, one can define a set of Bloch-like wavefunctions $\psi_n(\mathbf{k})$ in the Wannier gauge by employing an inverse Fourier transformation,

$$|\psi_{n\mathbf{k}}^{\text{W}}\rangle = \sum_{\mathbf{R}} e^{i\mathbf{k}\cdot\mathbf{R}} |\mathbf{R}n\rangle, \quad (2.25)$$

which vary smoothly with \mathbf{k} , unlike the original Bloch wavefunctions $\psi_{n\mathbf{q}}$. The Hamiltonian in the Wannier gauge is

$$H_{mn}^{\text{W}}(\mathbf{k}) = \sum_{\mathbf{R}} e^{i\mathbf{k}\cdot\mathbf{R}} H_{mn}^{\text{W}}(\mathbf{R}) = \sum_{\mathbf{R}} e^{i\mathbf{k}\cdot\mathbf{R}} \langle \mathbf{0}n | H | \mathbf{R}m \rangle. \quad (2.26)$$

Diagonalization with respect to the unitary matrix $U(\mathbf{k})$:

$$H^H(\mathbf{k}) = U^\dagger(\mathbf{k}) H^{\text{W}}(\mathbf{k}) U(\mathbf{k}). \quad (2.27)$$

leads to the eigenenergies and eigenstates in the Hamiltonina gauge:

$$|\psi_n^H(\mathbf{k})\rangle = \sum_m U_{nm} |\psi_m^{\text{W}}(\mathbf{k})\rangle. \quad (2.28)$$

The previous description of the method assumes a set of isolated bands across the entire Brillouin zone. If the bands of interest instead overlap and hybridize with other bands, forming so-called *entangled bands*, Wannier90 applies a disentanglement step.

In this step an energy window (*frozen window*) is first chosen containing all relevant states, and then performs a variational algorithm to select, at each \mathbf{k} point, an optimal M -dimensional Bloch subspace [171]. Once this new Bloch manifold is defined, the standard Wannier interpolation procedure is used to construct the localized Wannier functions.

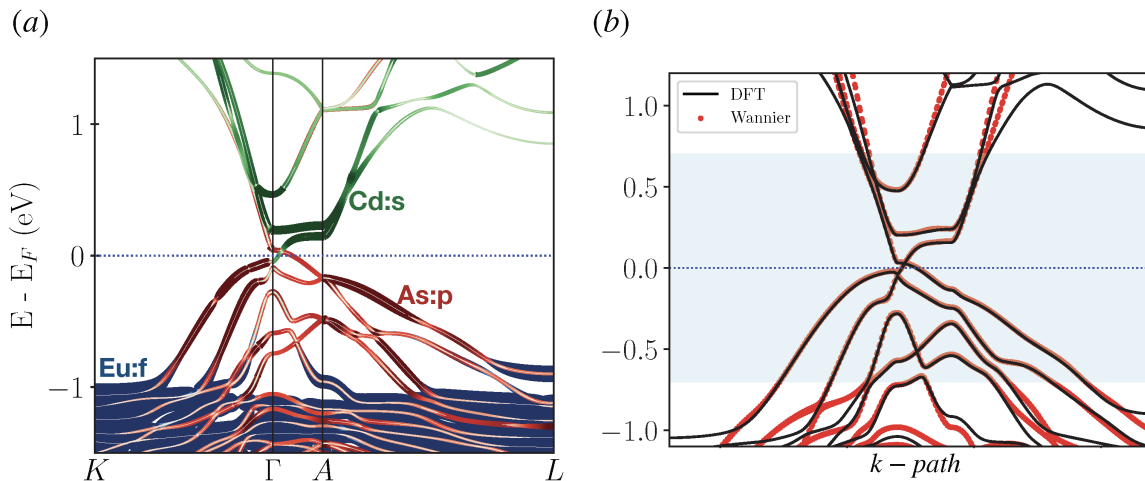


Figure 2.2: **Disentanglement of the energy bands of antiferromagnetic EuCd_2As_2 :** (a) Orbital projection of the electronic structure, showing Cd-s and As-p states dominating near the Fermi level, while localized Eu-f states dominate along the flat bands. (b) Comparison between DFT bands and Wannier bands by projecting the Cd-s and As-p orbitals within the frozen energy window, highlighted in light-blue.

In Fig. 2.2 (b), we show the Wannier bands obtained to capture the band-crossing near the Fermi level in the antiferromagnetic phase of EuCd_2As_2 , constructed solely through the disentanglement step. The resulting Wannier bands accurately reproduce the DFT bands within the frozen energy window, which was chosen to include only the Cd-s and As-p states while excluding the Eu-f states, the orbital composition is shown in Fig. 2.2(a). In some cases, constructing the MLWFs are required to accurately reproduce the DFT bands. However, it is generally advisable to limit the number of Wannier interpolation steps, as excessive iterations can break symmetries because the spread minimization does not enforce the space group symmetries. However, symmetrization of the Wannier Hamiltonian is possible using the Wannsymm code [172] or WannierTools [173].

2.3 Surface state calculations

Here, we introduce the mathematical methods implemented in WannierTools [173], which we used to calculate the surface state spectrum. The initial step is to define the bulk crystal as the stacking of a finite number of principal layers along the axis perpendicular to the surface of interest [174, 175], as seen in Fig. 2.3(a). A principal

layer is defined as a group of atomic planes arranged such that only nearest-neighbor interactions between principal layers is sufficient, as shown in Fig. 2.3(b). Since the slab system is periodic along the two-dimensional plane parallel to the surface, the two-dimensional wave vector \mathbf{k}_{\parallel} serves as a good quantum number, allowing to reduce the system to a one-dimensional slab system for each value of wave vector \mathbf{k}_{\parallel} . The Hamiltonian for the slab system consisting of N principal layers is given by,

$$\mathcal{H}_{slab}(\mathbf{k}_{\parallel}) = \begin{pmatrix} \mathcal{H}_{00} & \mathcal{H}_{01} & 0 & \cdots \\ \mathcal{H}_{10} & \mathcal{H}_{11} & \mathcal{H}_{12} & \cdots \\ 0 & \mathcal{H}_{21} & \mathcal{H}_{22} & \cdots \\ \vdots & \vdots & \vdots & \ddots \\ , & & & \end{pmatrix} \quad (2.29)$$

where \mathcal{H}_{mm} represents the hopping parameters between atomic planes within the m -th principal layer, while $\mathcal{H}_{m-1,m}$ denotes the hopping parameters between nearest-neighbor principal layers. The top surface hamiltonian correspond to $m = 0$ and the bottom surface to $m = N - 1$.

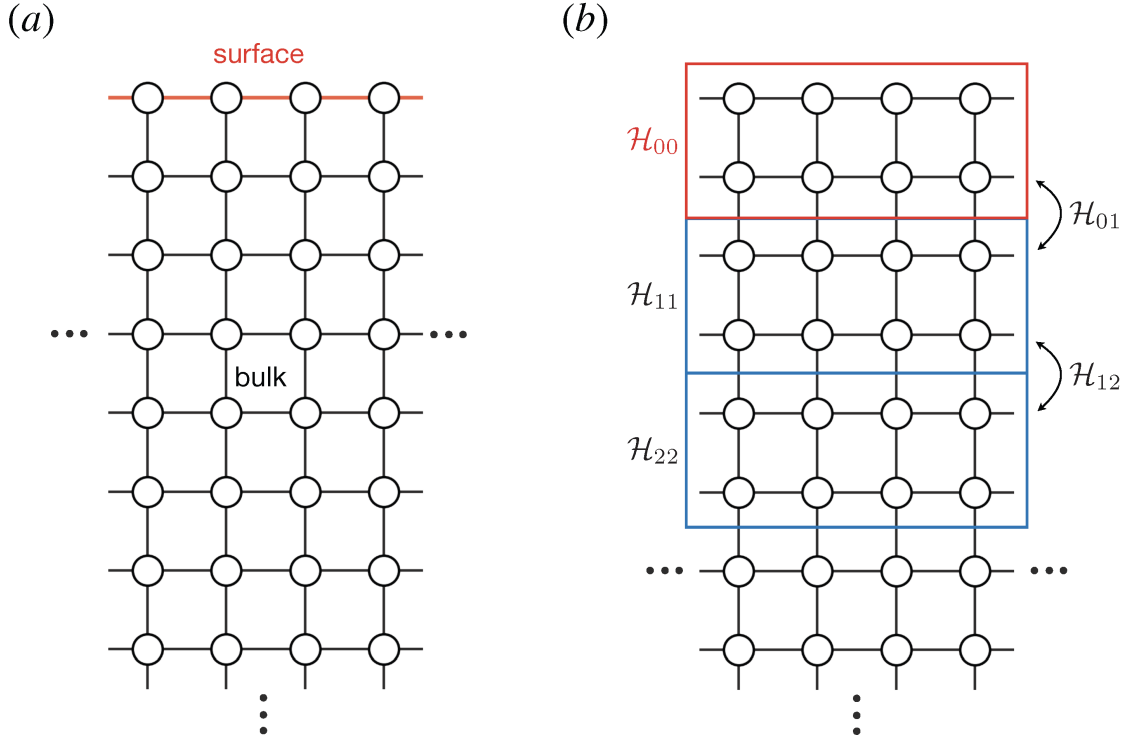


Figure 2.3: (a) Schematic representation of a 3D bulk cubic lattice, where the circles correspond to the atoms and the red line specifies the surface of interest. (b) The slab system, a finite stacking of N layers along the axis perpendicular to the surface. For this case, each principal layer consist of 2 atomic planes.

Instead of solving the entire Hamiltonian in Eq. 2.29 to identify the electronic states localized at the surface, one can employ the iterative method proposed by Sancho et al.

[175, 176] to compute the surface Green function $G_s = G_{00}(\omega)$. The surface spectrum function can be then obtained from the imaginary part of the surface green function,

$$A(\mathbf{k}, \omega) = -\frac{1}{\pi} \text{Im} \text{Tr} G_s(\mathbf{k}_{\parallel}, \omega + i\eta). \quad (2.30)$$

This iterative method consist of replacing the initial slab system with an effective slab where the lattice constant is doubled at each step. Additionally, with each iteration, the number of atomic layers used to represent a principal layer doubles, while the interaction between these new effective layers becomes progressively weaker. After n iterations, each effective principal layer corresponds to 2^n initial principal layers. Further details of the algorithm are provided in [175, 176]. Within WannierTools, an important parameter to ensure convergence is the number of atomic layers N_p used to define the principal layer. As more delocalized Wannier functions extend their hopping interactions over larger distances, they require a large N_p . Selecting too small N_p can lead to innacurate surface states or distorted Fermi-arc dispersions, while a large N_p only increases computational cost.

Finally, these calculated surface states can be directly compared with experiments. In particular, the angle-resolved photoemission spectroscopy (ARPES) is suitable for such comparisons, as it probes only the outermost atomic layers, and is therefore intrinsically surface sensitive, providing momentum-resolved information of the surface states of 3D topological insulators and semimetals [177].

Computational details within VASP

Self-consistent calculation:

A self-consistent calculation requires four essential input files: POSCAR, POTCAR, INCAR, and KPOINTS. POSCAR specifies the crystal structure (lattice vectors and atomic coordinates). POTCAR contains the pseudopotentials for each atomic species within the PAW potential created with the GGA=PBE functional. KPOINTS specifies the k-points used to sample the Brillouin zone. INCAR contains all the computational parameters, such as the plane-wave energy cutoff (ENCUT), type of potential, convergence thresholds, inclusion of SOC, DFT+U type, etc. Since we study the non-relativistic electronic structure of EuIn_2As_2 , we switch off the symmetrization with ISYM=-1, as VASP uses only the unitary part of the corresponding magnetic space group to symmetrize. In addition, we switch off the SOC with LSORBIT=False while keeping a non-collinear calculation setting LONCOLLINEAR=True.

VASP first reads the structural information in POSCAR and the atomic potentials in POTCAR to build the initial Kohn-Sham Hamiltonian. Using the parameters set in INCAR and the k-point mesh in KPOINTS, the code then performs a self-consistent cycle: starting from an initial guess for the electron density, it iteratively solves the Kohn-Sham equations until the total energy and charge density converge to the desired

accuracy set by the flag EDIFF in the file INCAR.

Convergence test:

Although the self-consistent calculation may converge electronically for a given set of parameters, it is crucial to ensure global convergence with respect to two parameters: the ENCUT and the k-point sampling of the Brillouin zone. An insufficient ENCUT can lead to inaccurate total energies, forces, and stresses, while an insufficiently dense k-grid can affect both total energies and derived properties such as magnetic moments. In Fig. 2.4, we show the systematic convergence test for the antiferromagnet EuCd_2As_2 , showing that well converged energies are achieved for ENCUT= 550 eV and a k-grid of roughly $22 \times 22 \times 6$.

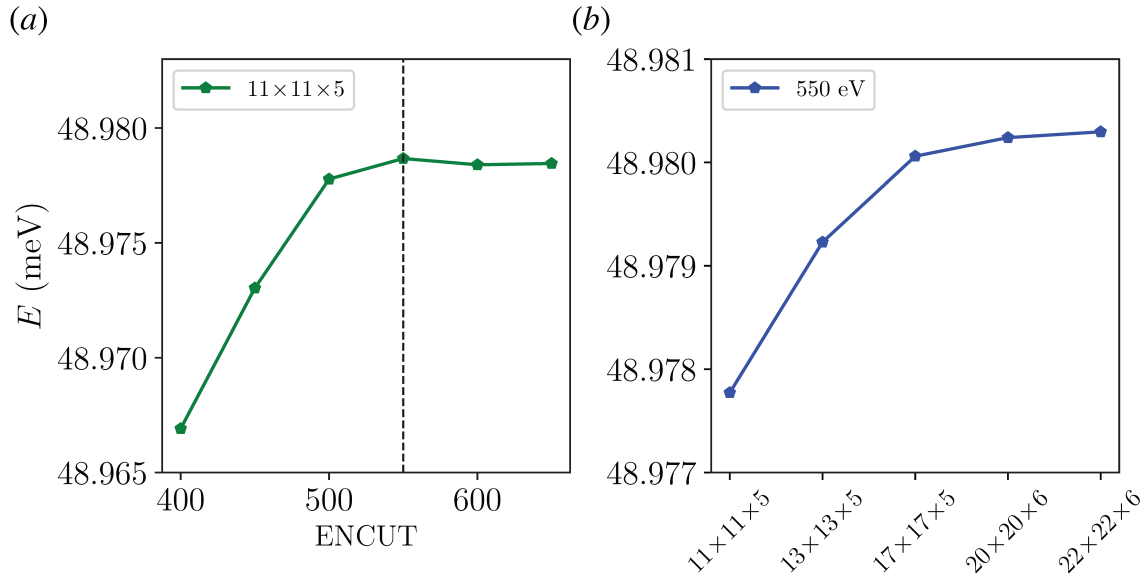


Figure 2.4: Convergence test of the total energy of antiferromagnetic EuCd_2As_2 . We first converged the ENCUT using a fixed $11 \times 11 \times 5$ k-grid, and then, keeping the converged ENCUT, refined the k-point mesh to achieve full convergence.

2.4 Summary

In this Chapter, we reviewed the implementation of density functional theory in VASP. We discuss the key approximations required to solve the Kohn-Sham equations, including exchange-correlation functionals, the use of pseudopotentials to treat the core electrons through an effective potential, and the incorporation of the Hubbard correction required in strongly correlated systems. We also review the Wannier interpolation method, which enables the construction of an effective Hamiltonian that accurately reproduces the bulk electronic bands, and serves as the foundation for further post-processing, such as transport responses. In addition, we described the surface state calculations that we will use to investigate the bulk-boundary correspondence in the topological EuCd_2As_2 , and outlined additional methods used to achieve convergence

for the non-collinear electronic structure of EuIn_2As_2 .

Chapter 3

Strain control of band topology in collinear EuCd_2As_2

"Anyone who has never made a mistake has never tried anything new."

— Albert Einstein

Eu-based compounds have attracted considerable attention as they host a rich variety of topological phases arising from the interplay between the electronic topology and the intrinsic magnetization of Eu atoms [25, 26, 39–45]. Among them, the magnetic semimetal EuCd_2As_2 , which orders antiferromagnetically under ambient conditions [38, 178], has been particularly attractive as it has been theoretically predicted to realize the Dirac and axion insulator phases, depending on the Néel vector orientation [24, 39, 47]. Beyond magnetic-field control of its bulk topology [48, 49], lattice deformations – through strain [34, 39] – and hydrostatic pressure [37, 50] have also proven to be very effective for tuning its electronic topology in a continuous and precise manner.

In this chapter, we explore how a set of in-plane shear strains influence the band topology and surface states of two collinear antiferromagnetic phases of EuCd_2As_2 . Our approach combines a symmetry analysis based on magnetic space groups with first-principles calculations that include spin-orbit coupling effects.

3.1 Crystal structure of collinear AFM EuCd_2As_2

EuCd_2As_2 crystallizes in a hexagonal centrosymmetric structure, belonging to the space group $P\bar{3}m1$ (No. 164). Its crystal structure consists of Cd_2As_2 bilayers located in between hexagonal layers of Eu atoms, as illustrated in Fig. 3.1(a-b). The primitive unit cell is highlighted in Fig. 3.1(a), and it contains 5 atoms.

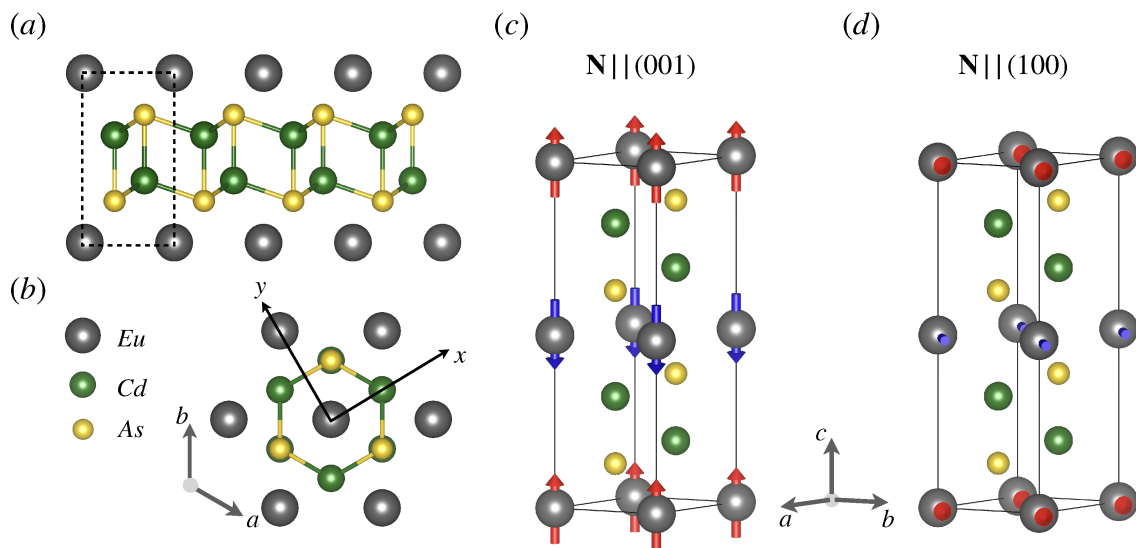


Figure 3.1: **Crystal structure of EuCd_2As_2 :** (a) Side view of the non-magnetic structure, in which the As_2Cd_2 bilayers are located in between layers of Eu atoms. The gray, green, and yellow represent Eu, Cd and As atoms, respectively. The dotted square corresponds to the primitive unit cell. (b) Top view, showing the hexagonal layer of Eu atoms. (c) The magnetic unit cell of the out-of-plane spin configuration with a Néel vector orientation along the c -axis (001), and (d) the in-plane spin configuration with a Néel-vector orientation along (100). The directions (001) and (100) are written as a function of the Cartesian coordinates. The lattice vectors are: $\mathbf{a} = \frac{a}{2} \hat{\mathbf{x}} - \frac{\sqrt{3}a}{2} \hat{\mathbf{y}}$, $\mathbf{b} = \frac{a}{2} \hat{\mathbf{x}} + \frac{\sqrt{3}a}{2} \hat{\mathbf{y}}$, and $\mathbf{c} = c \hat{\mathbf{z}}$.

At ambient pressure and below $T_N = 9.5$ K, the Eu moments adopt a collinear A-type antiferromagnetic (AFM) configuration, in which the Eu layers align ferromagnetically in the ab plane, and these layers stack antiferromagnetically along c , with the Néel vector preferentially lying in the ab plane [38, 178], as shown in Fig. 3.1(d). The magnetic unit cell doubles the non-magnetic unit cell along the c -axis, as a consequence of the $\mathcal{T}\tau$ symmetry that relates the opposite spin sublattices, where $\tau = \{0\ 0\ 1/2\}$ is a fractional translation. An out-of-plane A-type AFM order with the magnetic moments aligned along the c axis, illustrated in Fig. 3.1(c), has also been investigated via *ab initio* calculations and reported to host the Dirac semimetal phase [24, 39]. This configuration is energetically very close to the in-plane AFM state, with a magnetic anisotropy of roughly 1 meV, and Ref. [39] further suggests that lattice deformations can tune the Néel vector orientation.

To ensure reliable electronic structure calculations, we first relaxed the crystal structures using VASP so that the starting configurations don't include residual stresses or forces. A structure is considered relaxed when the magnitude of every atomic force falls below a chosen threshold. In our calculations, we set the residual forces to be smaller than 0.01 eV/Å. The experimental and the fully relaxed lattice parameters together with the Cd and As positions are listed in Table 3.1, showing a good agreement

between measured and computed values.

EuCd ₂ As ₂	experimental values	relaxed values
a [Å]	4.450	4.508
c [Å]	7.350	7.404
z Cd ($2d$)	0.633	0.634
z As ($2d$)	0.247	0.246

Table 3.1: Experimental and relaxed lattice parameters of EuCd₂As₂, including the fractional coordinate z of the Cd and As atoms at the Wyckoff position ($2d$). The experimental lattice parameters were taken from Ref. [179].

3.2 The Dirac semimetal phase in the out-of-plane AFM EuCd₂As₂

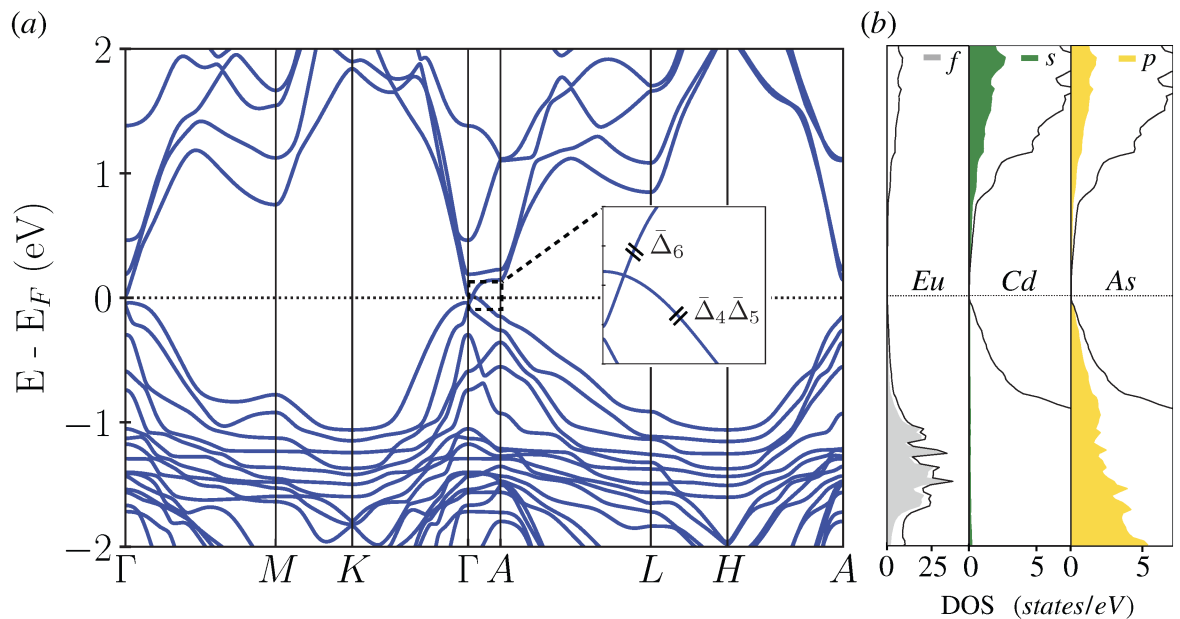


Figure 3.2: **GGA+U+SOC electronic band structure of EuCd₂As₂ with a Néel vector along (001)**: (a) Doubly-degenerate bands along the high symmetry k-points. The right inset plot shows a zoomed-in view of the energy bands along $\Gamma - A$, highlighting a fourfold degenerate band crossing – a enforced Dirac point – arising from the forbidden mixing of bands belonging to different irreducible corepresentations, $\bar{\Delta}_6$ and $\bar{\Delta}_4\bar{\Delta}_5$. (b) Density of states of the dominant orbital contributions in the corresponding energy window.

We begin by analyzing the symmetries of the out-of-plane AFM state. This state belongs to the Type-IV magnetic space group (MSG) $P_c\bar{3}c1$ (No. 165.96), whose symmetry generators are the non-symmorphic time-reversal symmetry $\mathcal{T}' = \mathcal{T}\tau$, inversion

\mathcal{P} , a threefold rotation C_{3z} , and a two-fold screw rotation $\{C_{2x}|0\ 0\ 1/2\}$. Since this state preserves the combined \mathcal{PT}' symmetry, with $(\mathcal{PT}')^2 = -1$, Kramers spin degeneracy is enforced across the entire momentum-space, as discussed in Chapter 1.

We proceed to calculate the electronic band structure including spin-orbit coupling effects, and treating the on-site correlations in Eu-f orbitals with a Hubbard $U = 5$ eV, chosen to match the position of the flat bands reported by ARPES measurements [24, 47]. The energy bands along the high-symmetry k-path, shown in Fig. 3.2(a), are mostly gapped except for a single Dirac point along the $\Gamma - A$ line. Since inversion symmetry is preserved in this phase, a pair of Dirac points must occur along the k_z axis, as illustrated in Fig. 3.3(a). The density of states (DOS) in Fig. 3.2 (b) reveal the flat bands located at -1 eV below the Fermi level are primarily of Eu 4f character, while the states near the Fermi level are mainly contributed by the Cd s and As p orbitals.

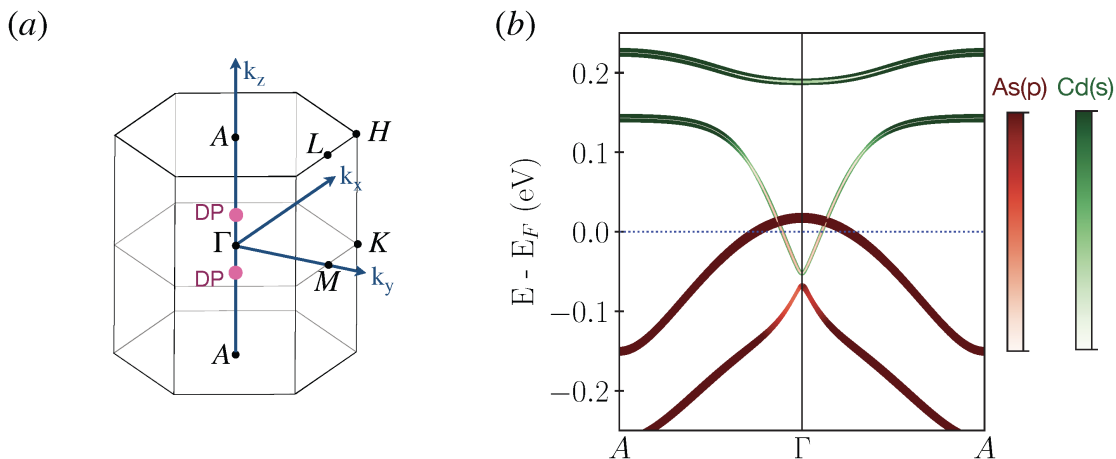


Figure 3.3: (a) Hexagonal Brillouin zone and the pair of Dirac points along the k_z axis. (b) The Cd (s) and As (p) orbital composition along the $A - \Gamma - A$ k-path.

According to the classification of stable 3D Dirac semimetals [39], conventional antiferromagnets with $\mathcal{T}\tau$ symmetry require a uniaxial rotation symmetry to stabilize a pair of Dirac points along its rotational axis. Here, in the out-of-plane AFM order, the three-fold rotation symmetry C_{3z} plays this role, protecting the pair of Dirac points along the k_z . This symmetry forbids hybridization between the doubly degenerate conduction and valence bands along $\Gamma - A$ as they transform according to different irreducible corepresentations (coreps) [34], labeled as $\bar{\Delta}_6$ and $\bar{\Delta}_4\bar{\Delta}_5$. We calculated the coreps using the Python code `irrep` [149] in combinations with the topological quantum chemistry (MTQC) [28, 29] tools implemented in the Bilbao Crystallographic Server, details are provided in Section 1.3.3. Within MTQC, such symmetry-enforced crossings are classified as *enforced semimetals*, indicating the presence of a stable 3D Dirac semimetal phase in the out-of-plane AFM order of EuCd_2As_2 .

Because the Dirac semimetal state is gapless, defining a bulk topological invariant

is subtle. Instead, we infer the non-trivial topology from the surface spectrum. Dirac semimetals typically exhibit two Fermi arcs connecting the pair of Dirac points, as each Dirac point can be viewed as two overlapping Weyl points with opposite chirality; however, these surface arcs are considered to be very fragile as they are not topologically protected [180].

To compute the surface states, we first construct an effective tight-binding Hamiltonian with Wannier90 [169], using the dominant orbitals near the Fermi level, the p orbitals of As atoms and the s orbitals of Cd atoms, as shown Fig. 3.3(b). We then evaluate the surface states using the iterative Green's function method with WannierTools [173], more details are provided in Section 2.3. The side surface (010), displayed in Fig. 3.4, shows two Fermi Arcs connecting the projected bulk Dirac points, in agreement with previous reports [39].

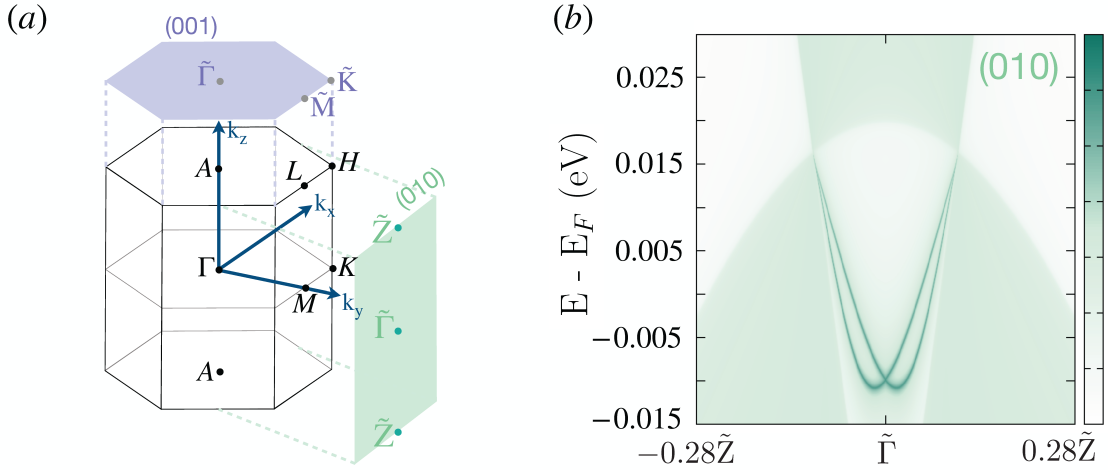


Figure 3.4: (a) The hexagonal Brillouin zone, and the (001) and (010) surfaces, used to calculate the surface spectrum. (b) The momentum-resolved surface spectrum along the $Z - \Gamma - Z$ path of the (010) face. It shows two Fermi arcs connecting the pair of bulk Dirac points.

3.3 Higher-order topological insulator phase in the in-plane AFM EuCd_2As_2

When the magnetic moments are pointing in-plane, EuCd_2As_2 belongs to the MSG C_c2/m (No. 12.63), whose generators are \mathcal{T}' , \mathcal{P} , and C_{2x} . The combined \mathcal{PT}' symmetry is preserved, enforcing Kramers degeneracy through the momentum-space. Evidently, in this configuration, the threefold rotation C_{3z} symmetry that protected the pair of Dirac points in the out-of-plane AFM order is broken, leading to a band gap opening of approximately 10 meV at the Dirac points, as shown in the energy bands in Fig. 3.5(a). This band gap arises because the relevant bands now transform under the same irreducible corepresentation, $\bar{B}_3\bar{B}_4$, preventing the existence of symmetry-enforced band

crossings.

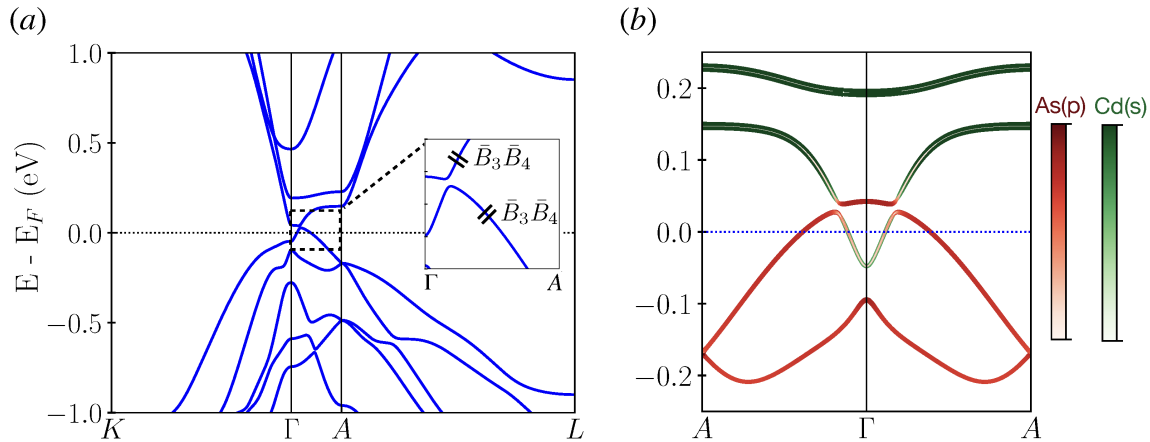


Figure 3.5: **GGA+U+SOC electronic band structure of EuCd_2As_2 with a Néel vector along (100)** : (a) Energy bands along the path $K-\Gamma-A-L$. The inset shows the zoomed-in of the energy bands along $\Gamma-A$, displaying a band gap of 10 meV. (b) Band-inversion between the Cd s and As p orbitals.

The presence of band inversion between the Cd s and As p orbitals, shown in Fig. 3.5(b), suggests a non-trivial topology in the bulk. Using MTQC, we evaluate the symmetry indicators, classifying the in-plane AFM phase as an axion insulator, characterized by the parity-based invariant $\eta_{AI} = 2$, consistent with previous reports [24]. In addition, the MSG C_c2/m also preserves the mirror symmetry $M_x = \mathcal{P}C_{2x}$, and we know from Section 1.3.1 that insulators with mirror symmetries can be classified by a mirror Chern number. Using the IrRep code [149], we obtain an additional non-trivial symmetry indicator $\delta_{2m} = 1$ from our *ab initio* calculations, indicating the difference of mirror Chern numbers at $k_x = 0$ and $k_x = \pi$, thereby classifying this AFM order as a topological crystalline insulator (TCI) as well. From the bulk-boundary correspondence in TCIs, mirror-protected gapless Dirac cones appear on surfaces that preserve the mirror symmetry, as seen in Fig. 3.6(a,b): on the (001) and (010) surfaces. Besides gapless surface states protected by crystalline symmetries, surfaces in $\mathcal{T}\tau$ topological insulators remain gapless as long as the surface also preserves $\mathcal{T}\tau$; however, such states are generally not robust against disorder [77].

A key experimental signature to detect the axion insulator phase is a half-quantized anomalous Hall conductivity (AHC) that appears only on gapped surfaces [108, 111]. EuCd_2As_2 has two natural cleavage surfaces, the (001) and (101) surfaces [46]. Reference [24] proposes a gapped surface state on the (101) surface as both the \mathcal{T}' and mirror M_x are broken there. In addition, previous first-principles calculations reveal that applying uniaxial strain in the in-plane direction can also open a band gap on the (001) surface [39].

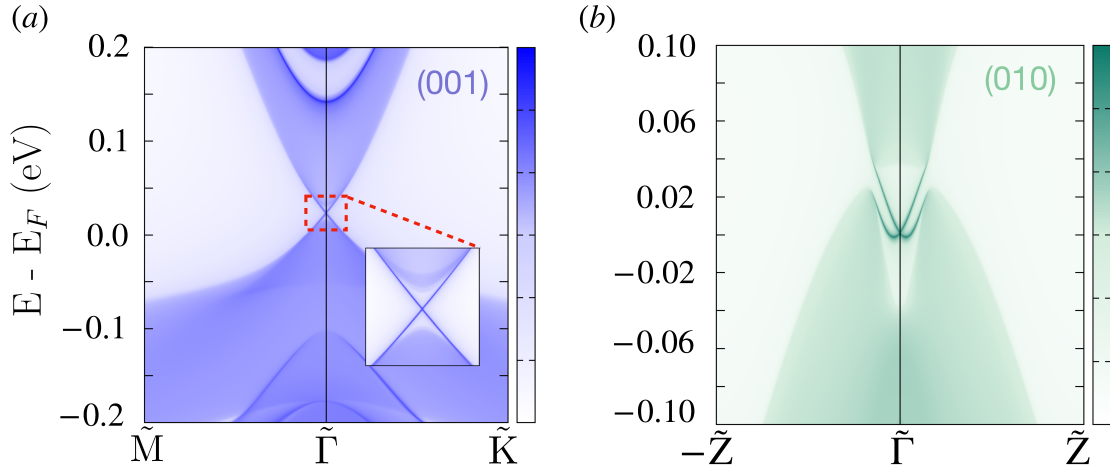


Figure 3.6: (a) The momentum-resolved surface spectrum along the $M - \Gamma - K$ path on the (001) surface, and (d) along the $Z - \Gamma - Z$ path on the (010) surface. Both spectrums show gapless surface states connecting the conduction and valence bands.

3.4 Band topology under shear strain

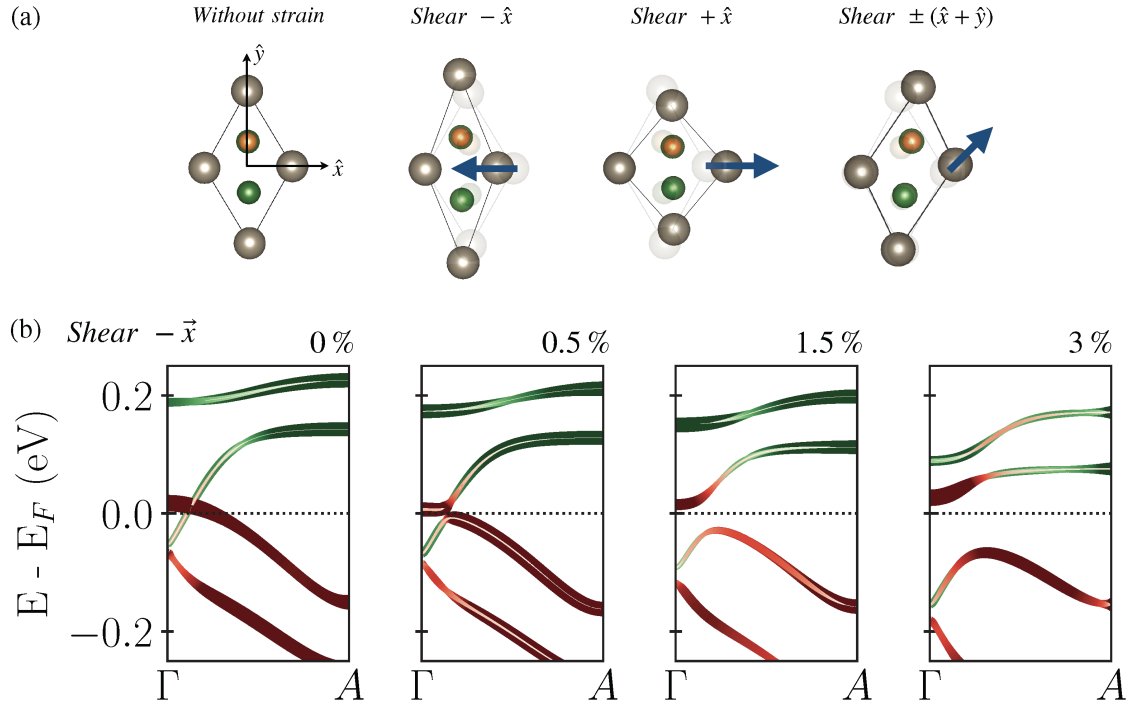


Figure 3.7: (a) Schematic illustration of the shear strain applied in three distinct in-plane directions, showing a top view of the deformation of the EuCd_2As_2 unit cell. (b) Energy bands of the out-of-plane AFM order including orbital composition of Cd-s (green) and As-p (red) orbitals along the $\Gamma - A$ path under shear strain applied along the $-x$ direction.

We apply shear strain along three different in-plane directions: $+\vec{x}$, $-\vec{x}$, and $\pm(\vec{x} + \vec{y})$, these deformations can be visualized in Fig.3.7(a). The strain strength is determined by the percentage change in the lattice parameters. For each of the strained cases, after applying the corresponding deformation, we relaxed only the internal atomic positions. In Fig. 3.7(b), we show the energy bands of the out-of-plane AFM order under increasing the shear strain along $-x$. A gap opens at the Dirac point at small strain values and increases with further deformation, while the band inversion between the Cd s and As p orbitals still remains.

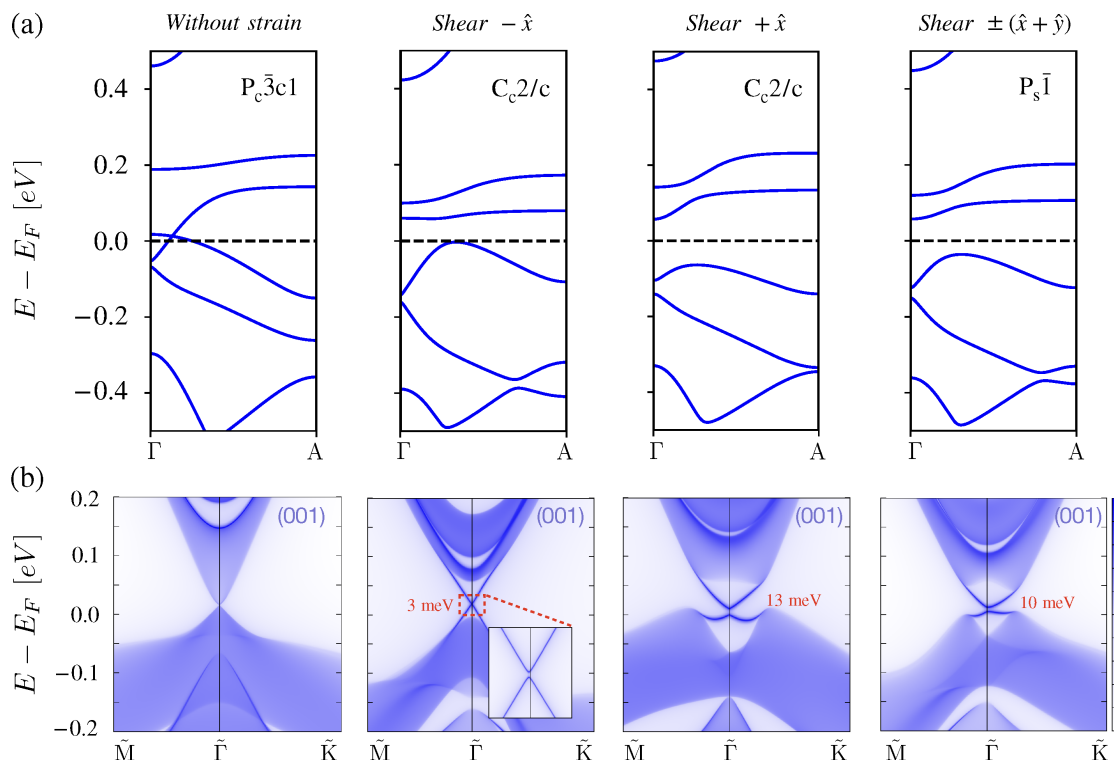


Figure 3.8: **GGA+SOC+U electronic structure of the unstrained and strained out-of-plane AFM order:**. (a) Energy bands along the $\Gamma - A$ path. The magnetic space group (MSG) are given at the top right. (b) The momentum-resolved surface spectrum for the unstrained (left panel) and strained (middle and right panels) structures along the $M-\Gamma-K$ path on the (001) surface.

We apply a 3% lattice deformation to compute the surface states. Beginning with the out-of-plane AFM order, in Fig. 3.8(a) we compare the un-strained and strained electronic structures. Under both positive (along $+x$) and negative (along $-x$) shear strain modulations, the MSG of the system lowers to C_c2/c (No. 15.90), whose generators are \mathcal{T}' , inversion \mathcal{P} , and a two-fold screw rotation $C_{2x} = \{C_{2x}|0\ 0\ 1/2\}$. In both cases a gap opens on the (001) surface, the positive shear modulation along $+x$ produces the larger gap of 13 meV. Thi gap arises from the breaking of \mathcal{T}' induced by the open boundary conditions imposed along the c -axis used for the calculation of the (001) surface spectrum. Applying diagonal shear strains further lower the magnetic

symmetries to $P_s\bar{1}$ (No. 2.7), whose generators include only \mathcal{T}' , and inversion \mathcal{P} . For all cases, a gapless surface states on the (001) surface is guaranteed, as this surface preserves \mathcal{T}' .

All the three strained cases for the out-of-plane AFM order up to 3% lattice deformation are classified as axion insulators, characterized by the topological invariant $\eta_{4I} = 2$. This transition from the Dirac semimetal phase to the axion insulator phase can be realized with a smaller percentage change in the lattice parameters than the 3% case examined here.

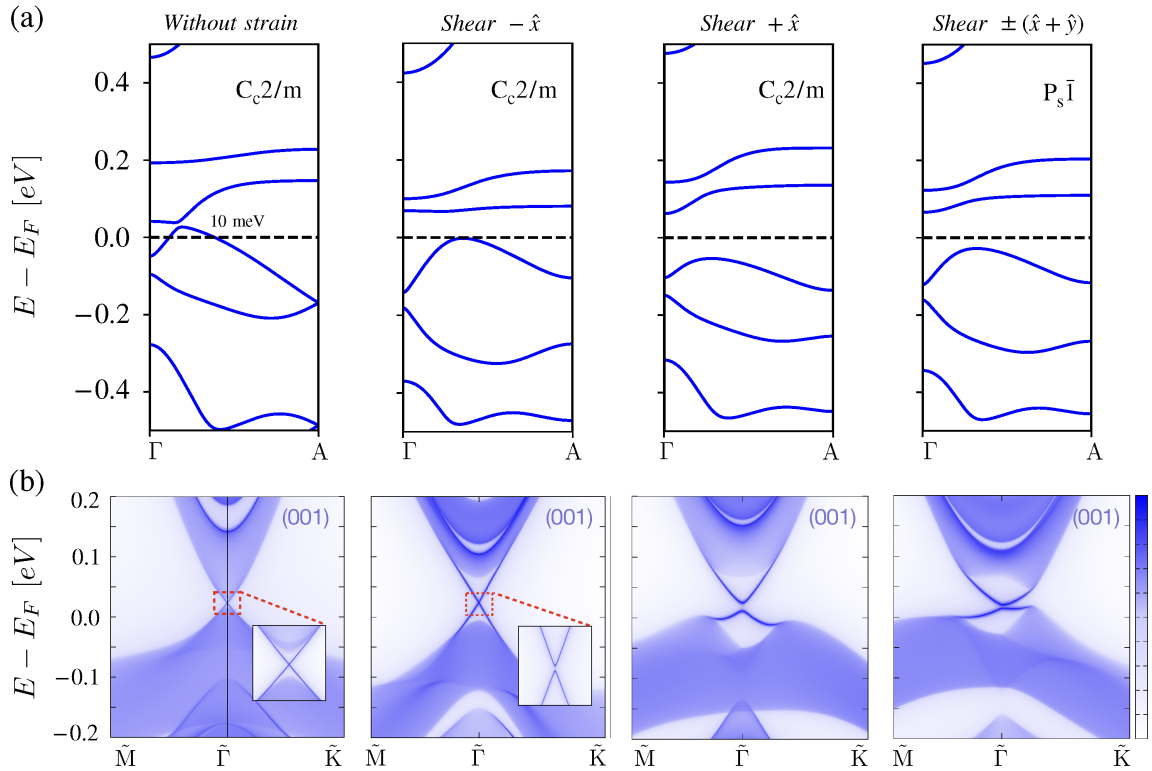


Figure 3.9: **GGA+SOC+U Electronic structure of the unstrained and strained in-plane AFM order:** (a) Energy bands along $\Gamma - A$. The magnetic space group (MSG) are given at the top right. (b) The momentum-resolved surface spectrum for the unstrained (left panel) and strained (middle and right panels) structures along the $M-\Gamma-K$ path on the (001) surface.

Applying shear strain to the in-plane AFM order lowers the magnetic symmetries to C_c2/m , and $P_s\bar{1}$, while preserving the axion-insulator phase. Although the bulk topology remains unchanged, all shear strains drive the (001) surface from a gapless Dirac state to a gapped one, as shown in Fig. 3.9. In both AFM configurations, shear along $+x$ produces particularly a large surface gap, making them readily resolvable by angle-resolved photoemission spectroscopy measurements.

3.5 Summary

In this Chapter, we examine the band topology of the collinear AFM phases of EuCd_2As_2 . We confirm through first principles calculations and symmetry analysis a Dirac semimetal phase protected by a C_{3z} symmetry in the out-of-plane AFM order, and a topological crystalline insulator phase that coexists with a topological crystalline insulator phase with in the in-plane AFM order. We then explored the effects of in-plane shear strains in both AFM configurations. For the out-of-plane AFM order, all shear strains break the C_{3z} symmetry, gap the bulk Dirac points and drive the system into the axion insulator phase. In the in-plane AFM order, the axion insulator phase persists under strain; however, the (001) cleavage surface undergoes a transition from gapless to gapped surface states, opening a route to observe hinge modes along those edges.

Chapter 4

Exchange-dominated physics in non-collinear EuIn_2As_2

"Nothing in life is to be feared, it is only to be understood. Now is the time to understand more, so that we may fear less.."

— Marie Curie

First-principles studies initially proposed EuIn_2As_2 as a promising axion insulator candidate while assuming a compensated collinear magnetic order [25, 181, 182]. However, experimental studies later revealed a more complex non-collinear structure, including a pure "helical" and a "broken-helical" phases [40, 65, 66]. Owing to the strong spin-orbit coupling, characteristic of Eu-based compounds, magnetic space groups have been mostly used to study these phases, especially to explore their topological properties [26, 40, 183].

In parallel, the emerging field of altermagnetism [56, 57] – as a new compensated collinear order with alternating spin-split bands – has driven the search for candidate materials. Among them, the compensated collinear phase of EuIn_2As_2 has been identified as an altermagnet based on first principles calculations, reporting spin-splittings reaching up to 150 meV [64], indicating exchange is strong in this compound, as recently confirmed by nuclear magnetic resonance measurements [67]. Spin space groups offer a suitable framework to capture the effects of exchange on the electronic structure, and have also been very aluable for investigating helical magnetic systems [55, 79, 184, 185], as they consider additional symmetries beyond those captured by the conventional magnetic space groups.

Motivated by the rich landscape of magnetic structures encompassing the helical and broken-helical phases, in this Chapter we combine a spin symmetry analysis and first-principles calculations, aiming to uncover exchange-driven features in the electronic structures that may influence the transport properties of EuIn_2As_2 .

4.1 Magnetic configuration

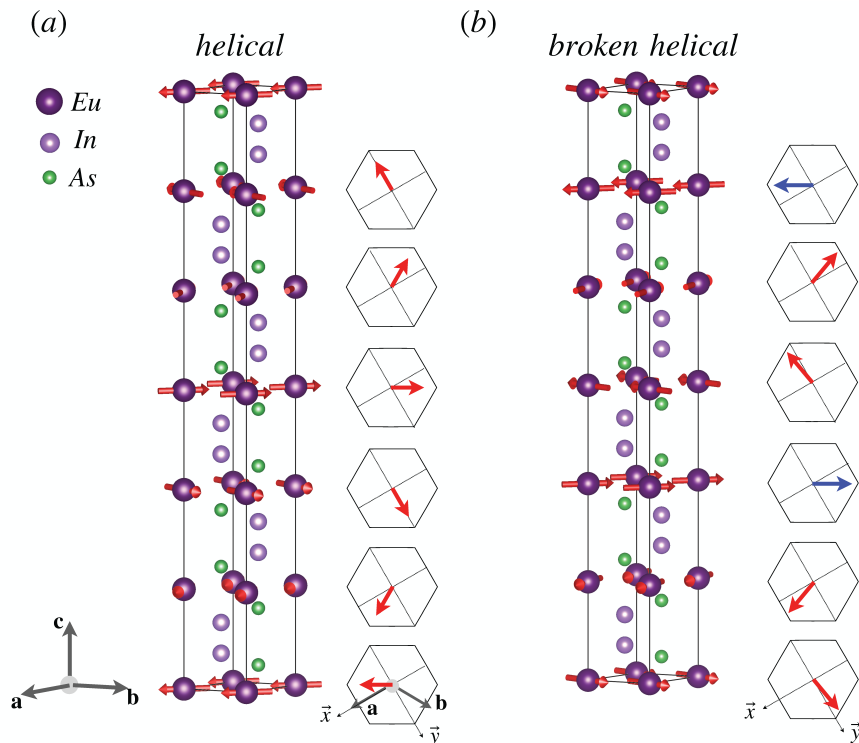


Figure 4.1: **Non-collinear coplanar magnetic textures of EuIn_2As_2 .** (a) The helical phase, with neighboring magnetic layers connected by 60° rotation along \hat{z} . (b) The broken-helical phase, with two symmetry-independent Eu magnetic sub-lattices. The red-red sublattices are connected by 80° and the red-blue spin sublattices by 130° . The lattice vectors are $\mathbf{a} = a\hat{x}$, $\mathbf{b} = -a\frac{\sqrt{3}}{2}\hat{x} + \frac{a}{2}\hat{y}$, and $\mathbf{c} = c\hat{z}$.

The crystalline structure of EuIn_2As_2 belongs to the centrosymmetric $P6_3/mmc$ space group and consists of alternating triangular layers of Eu atoms and In_2As_2 layers stacked along the c direction, as shown in Fig. 4.1. The commensurate "helical" and "broken-helical" magnetic phases were first identified by neutron diffraction [40] and then confirmed by x-ray scattering [65]. At $T_{N_1} = 17.6(2)$ K, a single propagation vector is reported $\mathbf{Q}_1 = (0, 0, 1/3)$, corresponding to the helical phase, shown in Fig. 4.1(a). This phase is characterized by magnetic moments on neighboring layers connected by 60° rotation along \hat{z} . At lower temperatures, the broken-helical phase emerges at $T_{N_2} = 16.2(1)$ K, where two propagation vectors were observed, $\mathbf{Q}_1 = (0, 0, 1/3)$ and $\mathbf{Q}_2 = (0, 0, 1)$, the helical and a collinear compensated order, respectively. This phase features a two symmetry-independent Eu magnetic sub-lattices, highlighted in red and blue in Fig. 4.1(b). The color blue also indicates the orientation of the collinear \mathbf{Q}_2 axis. The magnetic configurations of these phases were extracted from MAGNDATA [186]. Recent optical measurements combined with magnetic group-theory analysis still support the broken-helical phase in EuIn_2As_2 , although, the pure helix state has instead been reinterpreted as an amplitude modulated collinear order [66].

4.2 Non-trivial spin point group classification

Helical phase

We begin by identifying the spin point group associated with each of the studied phases. To do that, we use the *spinspg* package [94] to obtain all the spin space group symmetries. After factorizing out the translational subgroup of the Bravais lattice ¹ and keeping only the unitary symmetries, we obtain 72 spin space group symmetries of the form $[s_i|g_i]$. Here, the operator s_i acts exclusively on the spin-space, while the crystallographic operator $g_i = \{r_i|t_i\}$ acts on the real-space only, and consists of a point group operator r_i combined with a fractional translation t_i . By grouping the spin space group symmetries into subsets according to the type of t_i , the non-trivial spin space group results,

$$\begin{aligned} \mathcal{G}_s^H = & [E|3m|0] + [C_{2v}|\mathcal{P} \cdot 3m|0] + [C_{6z}|6mm - 3m|\tau] + \\ & [C_{2u''}|\mathcal{P} \cdot (6mm - 3m)|\tau] + [C_{3z}|3m|2\tau] + [C_{2v'}|\mathcal{P} \cdot 3m|2\tau] + \\ & [C_{2z}|6mm - 3m|3\tau] + [C_{2u}|\mathcal{P} \cdot (6mm - 3m)|3\tau] + [C_{3z}^{-1}|3m|4\tau] + \\ & [C_{2v''}|\mathcal{P} \cdot 3m|4\tau] + [C_{6z}^{-1}|6mm - 3m|5\tau] + [C_{2u'}|\mathcal{P} \cdot (6mm - 3m)|5\tau] . \end{aligned}$$

In this notation, the sets of symmetries applied on the real-space involve the point groups $6mm = \{E, C_{2z}, C_{3z}, C_{3z}^{-1}, C_{6z}, C_{6z}^{-1}, m_u, m_{u'}, m_{u''}, m_v, m_{v'}, m_{v''}\}$, its halving subgroup $3m = \{E, C_{3z}, C_{3z}^{-1}, m_u, m_{u'}, m_{u''}\}$, and the complement set $6mm - 3m = \{C_{6z}, C_{6z}^{-1}, C_{2z}, m_v, m_{v'}, m_{v''}\}$. Here, $C_{n\hat{n}}$ denotes a n -fold rotation around the \hat{n} -axis, and $m_{\hat{n}}$ denotes a mirror on the plane normal to \hat{n} , the axes are defined in Fig. 4.2. All translation operators are integer multiples of $\tau = (0, 0, \frac{1}{6}c)$, with c as the magnitude of the lattice vector $\mathbf{c} = c\hat{\mathbf{z}}$.

¹For a given set of lattice vectors $\{\mathbf{a}_1, \mathbf{a}_2, \mathbf{a}_3\}$, the translational group of the Bravais lattice is defined as $\mathbf{T} = \{[E|t_{\mathbf{R}}], \mathbf{R} = n_1\mathbf{a}_1 + n_2\mathbf{a}_2 + n_3\mathbf{a}_3 | n_1, n_2, n_3 \in \mathbb{Z}\}$

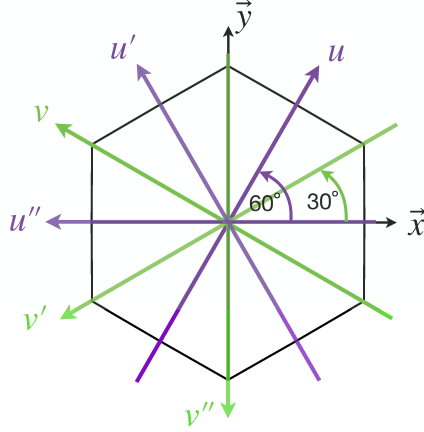


Figure 4.2: Six in-plane axes, $\{u, u', u''\}$ (green), and $\{v, v', v''\}$ (violet), where each pair $\{u, v\}$, $\{u', v'\}$, and $\{u'', v''\}$ consists of orthogonal axes.

Following the procedure to construct the non-trivial spin point group \mathbf{R}_s according to Litvin [53, 54], we first identify the crystallographic point group $\mathbf{G} = 6/mmm$ that includes all real-space symmetries with its corresponding normal subgroup $\mathbf{r} = 3m$. Then, we identify the point group that includes all spin-space symmetries, $\mathbf{B} = 622 = \{E, C_{3z}, C_{3z}^{-1}, C_{6z}, C_{6z}^{-1}, C_{2z}, C_{2v}, C_{2v'}, C_{2v''}, C_{2u}, C_{2u'}, C_{2u''}\}$ and its normal subgroup $\mathbf{b} = 3 = \{E, C_{3z}, C_{3z}^{-1}\}$, which is extracted from the spin translation group $\{[E||E|0], [C_{3z}||E|2\tau], [C_{3z}^{-1}||E|4\tau]\}$.

Next, we write \mathbf{G} and \mathbf{B} as a coset decomposition with respect to their normal subgroups, given by

$$\begin{aligned}\mathbf{G} &= \mathbf{r} + C_{2z} \mathbf{r} + C_{2x} \mathbf{r} + C_{2y} \mathbf{r}, \\ \mathbf{B} &= \mathbf{b} + C_{2z} \mathbf{b} + C_{2y} \mathbf{b} + C_{2x} \mathbf{b}.\end{aligned}$$

From the isomorphism between \mathbf{G}/\mathbf{r} and \mathbf{B}/\mathbf{b} , the cosets $G_i\mathbf{r}$ and $B_i\mathbf{b}$ are mapped on each other; pairing these corresponding cosets yields to the non-trivial spin point group of the helical phase:

$$\begin{aligned}{}^3_1 2_z 6 / {}^2_x m^1 m^2 z m &= [\mathbf{b}||E] \times \left\{ [E||\mathbf{r}] + [C_{2z}||C_{2z}\cdot\mathbf{r}] \right. \\ &\quad \left. + [C_{2y}||C_{2x}\cdot\mathbf{r}] + [C_{2x}||C_{2y}\cdot\mathbf{r}] \right\},\end{aligned}$$

The extra term 3_1 at the beginning represents the spin translation group. From the notation of the group name, we can extract the symmetry generators of the spin point group, which are $[C_{3z}||E]$, $[C_{2z}||C_{6z}]$, $[C_{2x}||m_z]$, $[E||m_x]$, and $[C_{2z}||m_y]$.

Broken helical

This more complex magnetic configuration, results in a smaller non-trivial spin space group with only 24 elements [94], organized as

$$\mathcal{G}_s^B = [E||3m] + [C_{2z}||(\overline{6}mm - 3m)|3\tau] + [C_{2v}||\mathcal{P} \cdot 3m|4\tau] + [C_{2u}||\mathcal{P} \cdot (\overline{6}mm - 3m)|\tau].$$

The crystallographic point group and its normal subgroup remain $\mathbf{G} = 6/mmm$ and $\mathbf{r} = 3m$. On the other hand, the spin counterpart has been reduced to the point group $\mathbf{B} = 222 = \{E, C_{2z}, C_{2v}, C_{2u}\}$ with its normal subgroup $\mathbf{b} = 1$ as the trivial group, indicating the spin-translation symmetries are broken. The coset decomposition of \mathbf{G} and \mathbf{B} is given by,

$$\begin{aligned} \mathbf{G} &= \mathbf{r} + C_{2z} \mathbf{r} + C_{2u} \mathbf{r} + C_{2v} \mathbf{r}, \\ \mathbf{B} &= E + C_{2z} + C_{2v} + C_{2u}. \end{aligned}$$

That leads to the non-trivial spin point group of the broken-helical phase:

$${}^2_z 6 / {}^2_u m^1 m^2_z m = [E||3m] + [C_{2z}||C_{2z} \cdot 3m] + [C_{2v}||C_{2u} \cdot 3m] + [C_{2u}||C_{2v} \cdot 3m].$$

The name of the group is independent of the axes choice. Here, we chose the u, v, z as they characterize the magnetic structure of the broken-helical. This group corresponds to the spin point group No. 478 of Table 1 in Ref. [54]. Its generators are $[C_{2z}||C_{6z}], [C_{2u}||m_z], [E||m_x]$, and $[C_{2z}||m_y]$. We note that this group has a similar structure than the pure helical phase, except for the absence of the spin translation group ${}^3_z 1$.

4.3 The helical phase

The spin point group of the helical phase can be constructed as the direct product between the non-trivial spin point group and the spin-only group, which is given by

$$\mathbf{R}_s^H = {}^3_z 1 {}^2_z 6 / {}^2_x m^1 m^2_z m \times \mathbb{Z}_2^{[C_{2z}\mathcal{T}||\mathcal{T}]}, \quad (4.1)$$

where $\mathbb{Z}_2^{[C_{2z}\mathcal{T}||\mathcal{T}]} = \{[E||E], [C_{2z}\mathcal{T}||\mathcal{T}]\}$ denotes the spin-only group characteristic of non-collinear coplanar magnets.

The generator $[C_{3z}||E]$ of the spin-translation group ${}^3_z 1$ acts exclusively within the spin-space, enforcing a purely out-of-plane spin polarization in the band structure, i.e., $\langle S_x \rangle = 0$ and $\langle S_y \rangle = 0$. On the other hand, the generator $[C_{2z}\mathcal{T}||\mathcal{T}]$ of the spin-only group, also known as coplanar symmetry, enforces an antisymmetric S_z spin

polarization, featuring an odd-parity-wave order, such that

$$S_z(k_x, k_y, k_z) \xrightarrow{[C_{2z}\mathcal{T}|\mathcal{T}]} -S_z(-k_x, -k_y, -k_z), \quad (4.2)$$

indicating the spin polarization S_z is perfectly antisymmetric under momentum reversal, $\mathbf{k} \rightarrow -\mathbf{k}$, in the non-relativistic limit. Additionally, the symmetry $[C_{2z}||C_{2z}]$, which transforms the S_z spin polarization as

$$S_z(k_x, k_y, k_z) \xrightarrow{[C_{2z}||C_{2z}]} S_z(-k_x, -k_y, k_z), \quad (4.3)$$

in combination with the coplanar symmetry, one gets

$$S_z(k_x, k_y, k_z) \xrightarrow{[C_{2z}\mathcal{T}|\mathcal{T}]} -S_z(k_x, k_y, -k_z), \quad (4.4)$$

which enforces a single spin-unpolarized plane at $k_z = 0$, since $S_z = 0$ for all k_x and k_y , if $k_z = 0$. Then leading to the existence of a p-wave order in the helical phase.

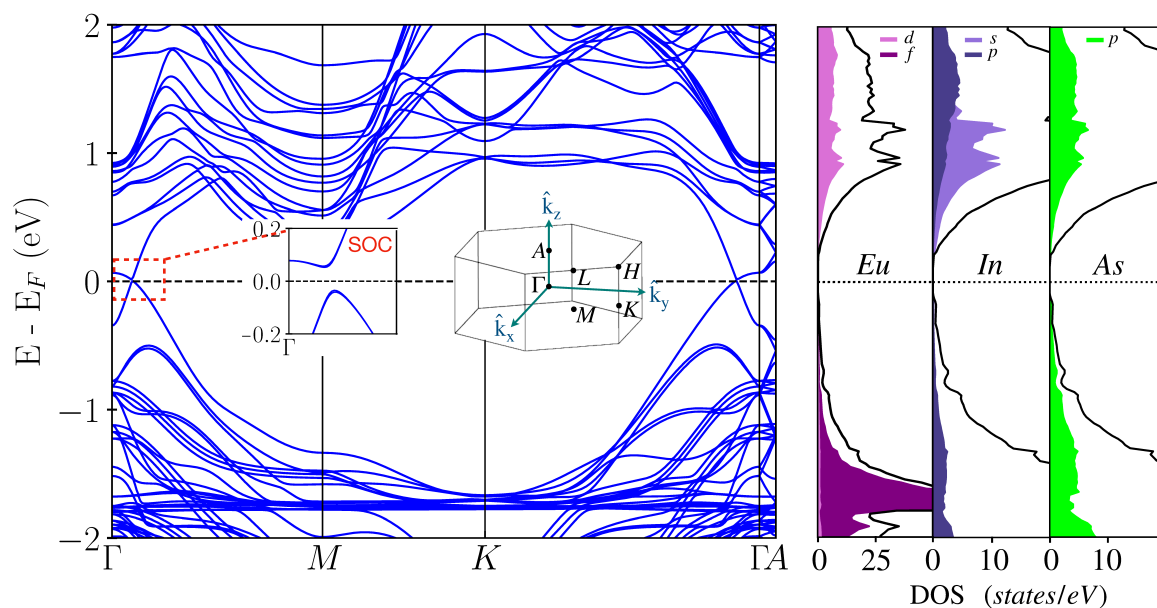


Figure 4.3: **GGA+U electronic structure of pure helical phase:** (Left) Energy bands along high-symmetry k -points, neglecting SOC. The inset shows a zoomed-in view of the bands near the Fermi level including SOC effects, resulting in a band gap of approximately 100 meV. (Right) Density of states, highlighting the orbital contribution within the selected energy window.

To capture the effect of all the spin symmetries on the electronic structure of the helical phase, we construct a two-band hamiltonian based on the spin point group generators. This effective model characterizes the energy dispersion and spin polarization around Γ ,

$$h(\mathbf{k}) = \left(A (k_x^2 + k_y^2) + B k_z^2 \right) \sigma_0 + C k_z \sigma_z. \quad (4.5)$$

Here, σ_0 denotes a 2×2 identity matrix, while σ_z represents the Pauli matrix along the [001] direction. This effective hamiltonian is governed by two main contributions, a quadratic spin-independent term in k , and a linear term $k_z \sigma_z$ that captures the p-wave spin polarization.

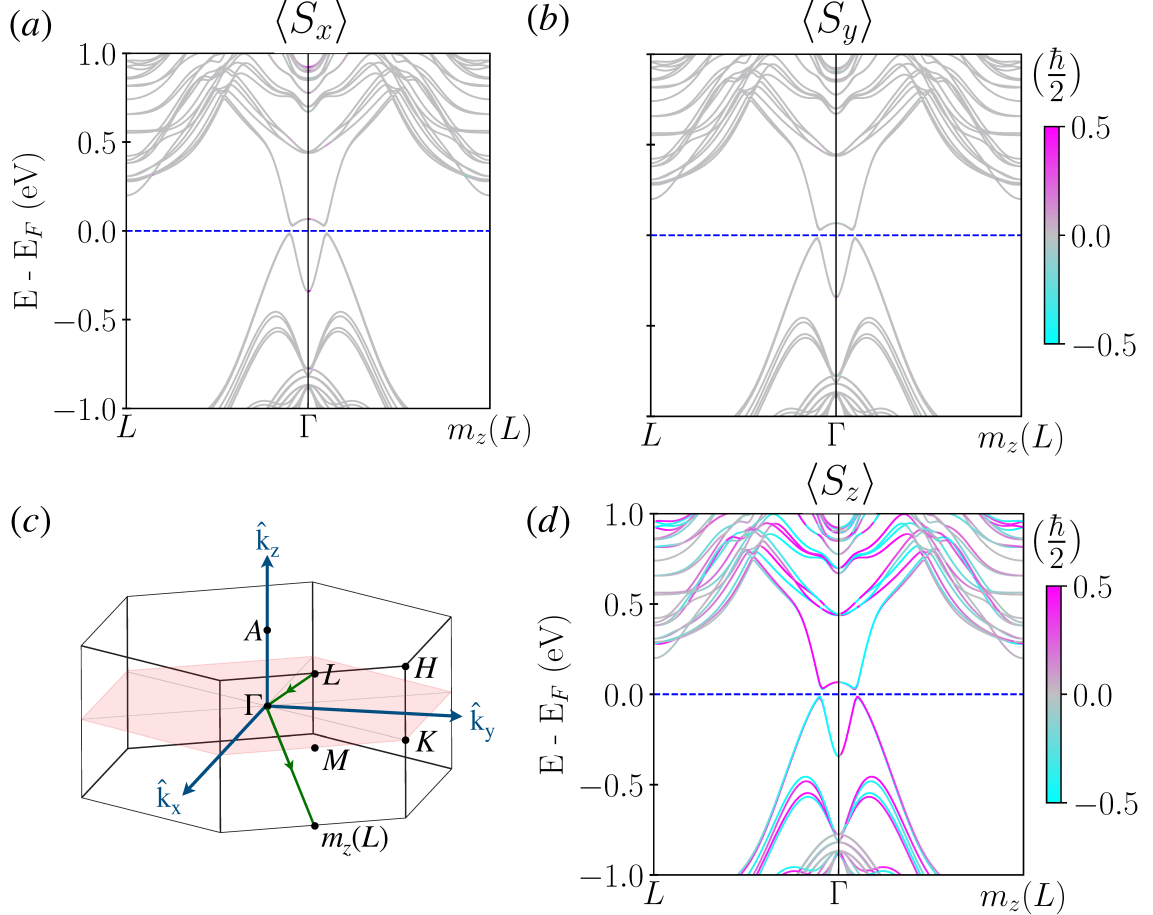


Figure 4.4: **GGA+U electronic structure of the helical phase without SOC:** Spin-polarized energy bands along the k-path $L - \Gamma - m_z(L)$, showing a collinear S_z spin polarization. (c) Hexagonal first Brillouin zone (1BZ), highlighting in red, the unpolarized nodal plane at $k_z = 0$ allowed for S_z , and highlighting in green the selected k-path.

Next, to validate our spin symmetry analysis, we perform a non-relativistic spin-polarized electronic structure calculations within density-functional theory (DFT) [153, 167]. The self-consistent calculations were carried out using constraints in the magnetic moment's directions [155]. To capture the non-relativistic effects, both the spin-orbit coupling and the symmetrization were switched off. In addition, we included a Hubbard U of 5 eV to account for the strongly localized Eu 4f orbitals.

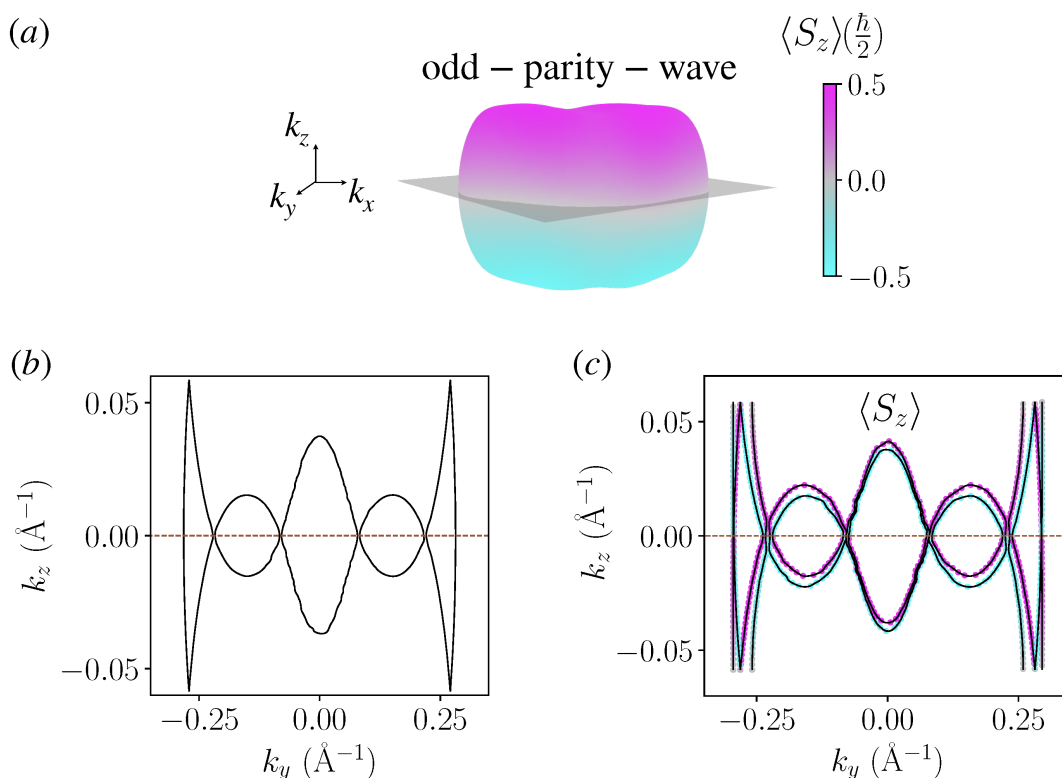


Figure 4.5: **Non-relativistic energy iso-surfaces of the pure helical order:** (a) Side view of the S_z spin-polarized energy iso-surface at $E = -0.60\text{eV}$, featuring a bulk odd-parity-wave order. (b) Energy iso-surface along the $k_x = 0$ plane for the non-magnetic state and (c) for the helical state. For comparison, the non-magnetic unit cell has been tripled along the z -axis.

We start by analyzing the electronic structure along the standard high-symmetry k-points of the hexagonal Brillouin zone (BZ). The energy bands in Fig. 4.3 show two band-crossings near the Fermi level along the $\Gamma - M$ and $\Gamma - K$ paths. Although \mathcal{PT} symmetry is broken, we observe degenerate bands along the $\Gamma - M - K - \Gamma$ path, and we observe the lifting of the bands degeneracy along the $\Gamma - A$ path. Including SOC opens a gap of around 100 meV near the Fermi level and it further splits the flat bands located around $E = -1.8$ eV, which are predominantly of Eu-f character. The orbital contribution of the electronic structure is shown on Fig. 4.3(right).

In Fig. 4.4 we plot the energy bands for each spin component along the k-path $L - \Gamma - m_z(L)$, where $m_z(L)$ is the mirror image of L -point with respect to the $k_z = 0$ plane, as indicated with the green arrows in Fig. 4.4(c). This path is particularly useful to visualize the spin-split bands, as it crosses the spin-unpolarized nodal plane at $k_z = 0$. The energy bands reveal a non-zero spin polarization exclusively for S_z , we also observe the alternating of the spin polarization upon crossing the Γ point, with spin splittings reaching up to 100 meV within the considered energy window. Since symmetrization was disabled in our DFT calculations, the negligible small values of the in-plane spin polarization, S_x and S_y , observed near the Γ point constitute numerical

artifacts. Our calculations also show that the energy scale of exchange and spin-orbit coupling in the helical phase are in the same order of magnitude.

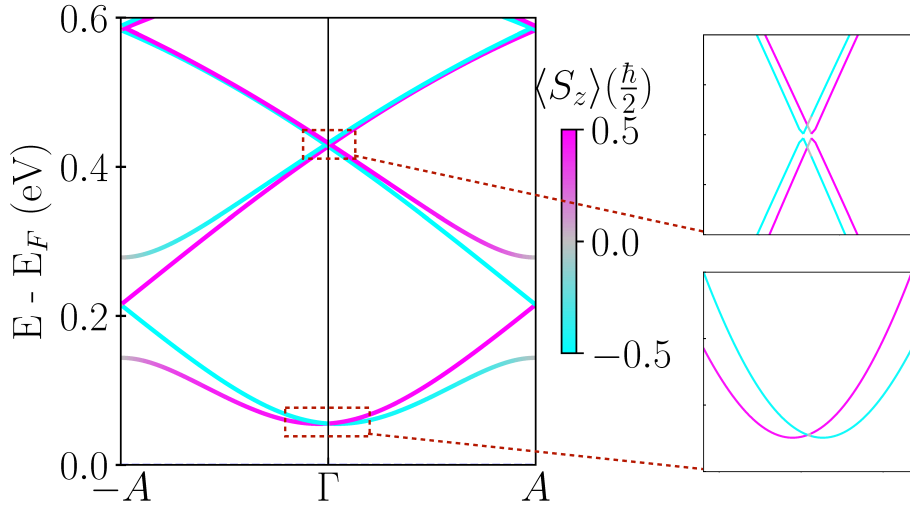


Figure 4.6: **Linear energy dispersion of the pure helical state:** S_z spin polarized energy bands along the $A - \Gamma - A$ path. The smaller panels on the right provide a zoomed-in of selected energy regions, revealing a dominant linear energy dispersion near Γ .

The p-wave character of the S_z spin polarization is illustrated in the energy iso-surface calculation in Fig. 4.5(a). In this figure, one can identify the spin-unpolarized plane as well as the alternating of the S_z spins, which are related by the coplanar symmetry $[C_{2z}\mathcal{T}||\mathcal{T}]$, effectively acting as \mathcal{T} in the momentum-space. Furthermore, by comparing the energy iso-surface of the non-magnetic state (Fig 4.5(b)) and the helical phase (Fig 4.5(c)), we confirm that the spin splittings primarily originate from the exchange interaction between local magnetic moments and itinerant electrons.

The characteristic linear energy dispersion near Γ associated with the p-wave order is visible along the $A - \Gamma - A$ path, as shown in Fig. 4.6. In contrast, for paths that deviate significantly from k_z , such as the $L - \Gamma - m_z(L)$ path, the energy dispersion is dominated by the quadratic term in Eq. 4.5.

We point out that the mechanism responsible for generating an antisymmetric S_z spin polarization in the helical phase differs from the materials studied in [63, 80]. The main distinction is that those materials preserve $\mathcal{T}\tau$, which enforces a linear dispersion at the Γ point, and an antisymmetric spin polarization for all spin components, which is preserved even when SOC effects are included. In contrast, in the helical phase, where $\mathcal{T}\tau$ is broken, only the coplanar symmetry $[C_{2z}\mathcal{T}||\mathcal{T}]$ guarantees an antisymmetric spin polarization for the S_z component, while the in-plane spin components exhibit a symmetric spin polarization. However, there is an additional symmetry $[C_{3z}||E]$ that forces the in-plane components to vanish, resulting in an effective antisymmetric and collinear spin polarization in momentum space, but only in the SOC free limit. Another

key distinction would be that, in $\mathcal{T}\tau$ p-wave magnets only time-reversal even responses would be allowed, while in other systems— where \mathcal{T} is not a symmetry element of the point group — time reversal odd responses (such as anomalous Hall effect or piezomagnetism) can be potentially present.

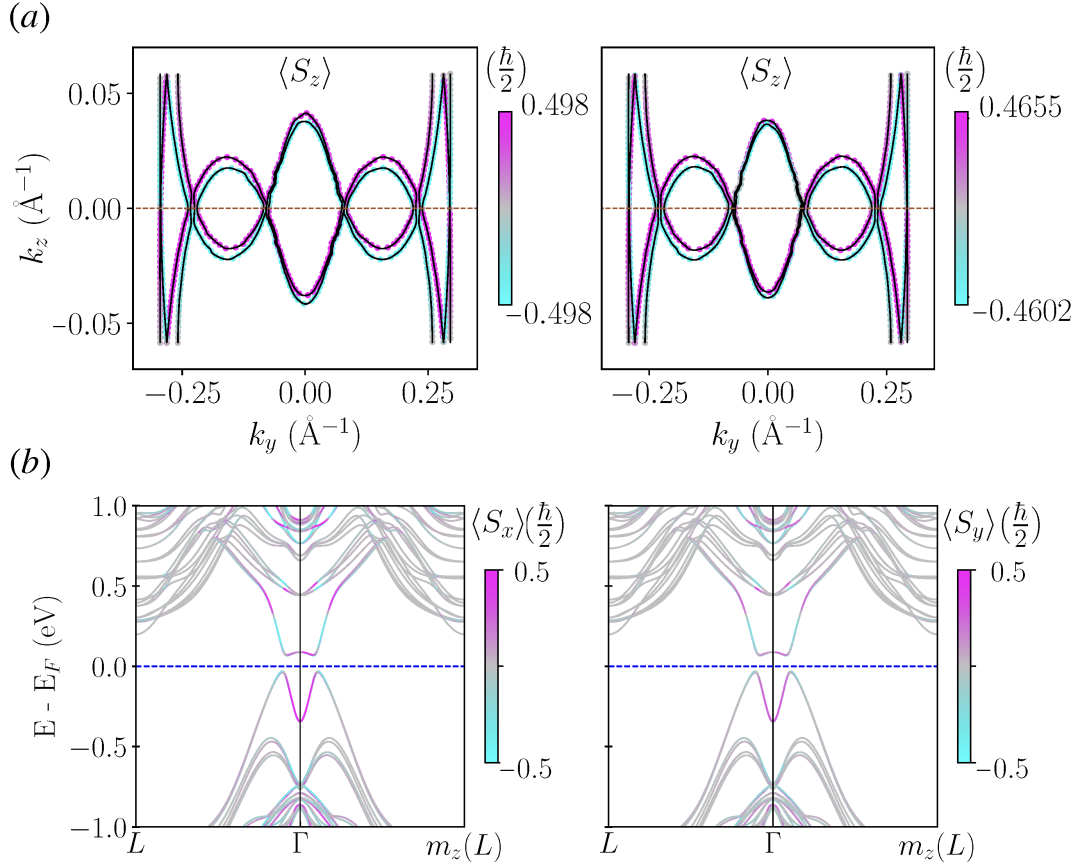


Figure 4.7: **GGA+U+SOC electronic structure of pure helical state:** (a) Comparison between the S_z spin-polarized energy iso-surfaces along the $k_x = 0$ plane and at energy $E = E_F - 0.60$ eV between the case without SOC (left) and with SOC (right). In the non-relativistic regime, the antisymmetric out-of-plane spin polarization is protected by the coplanar symmetry $[C_{2z}\mathcal{T}||\mathcal{T}]$. (b) In-plane spin polarized energy bands along the $L - \Gamma - m_z(L)$ path.

Including SOC effects on the electronic structure calculations, shows that the S_z p-wave order and the magnitude of the spin-split bands remain mostly unchanged; however, a closer inspection of the S_z spin expectation values reveal a subtle breaking of the antisymmetric order, as shown in Fig. 4.7(a,b), which is expected since $[C_2\mathcal{T}||\mathcal{T}]$ is no longer preserved. In addition, the breaking of the spin-translation symmetry $[C_{3z}||E]$ now allows an in-plane spin polarization, as shown in Fig. 4.7.

4.4 The broken-helical phase

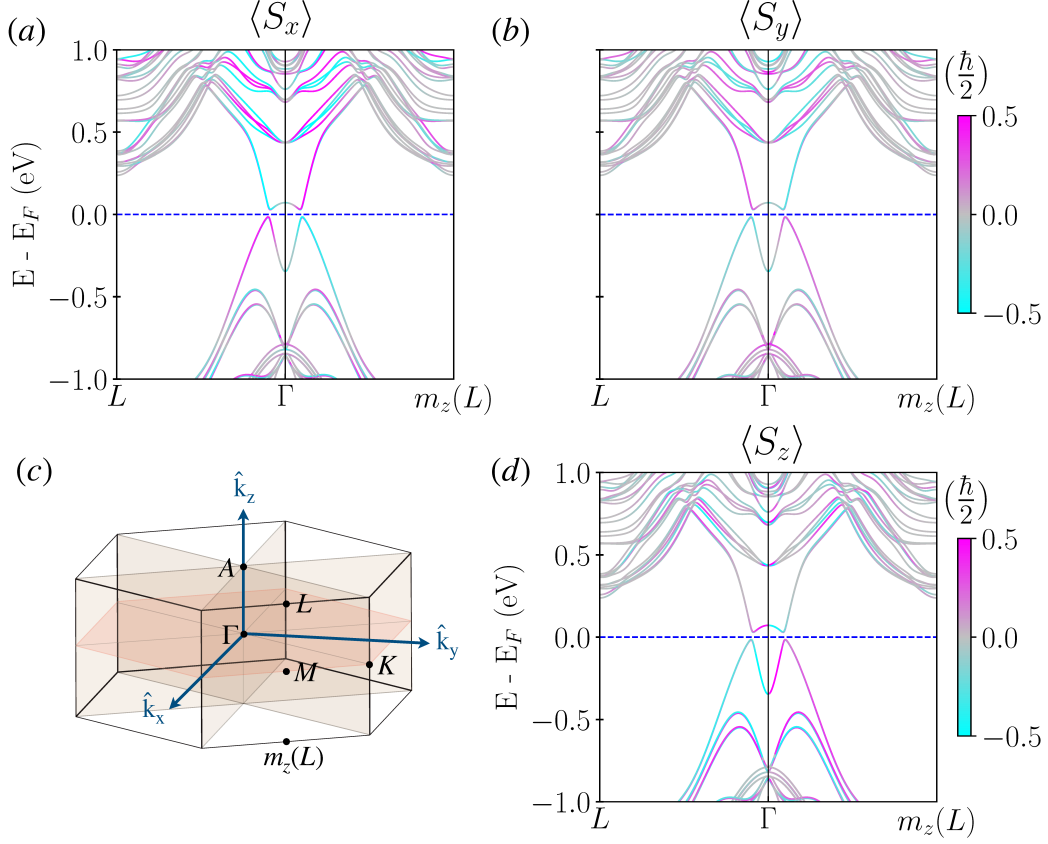


Figure 4.8: **GGA+U electronic structure of the broken-helical phase without SOC**: Spin-polarized energy bands along the $L - \Gamma - m_z(L)$ path. (c) The hexagonal BZ including the four nodal planes linked to the g-wave order, each separating regions of opposite spin polarization.

The total non-trivial spin point group identified for the broken-helical phase is

$$\mathcal{R}_s^B = {}^{2z}6/{}^{2u}m^1m^{2z}m \times \left\{ [E||E], [C_{2z}\mathcal{T}||\mathcal{T}] \right\}. \quad (4.6)$$

Here, the spin translation group ${}^{3z}1$ is no longer a symmetry of the system, meaning that the in-plane spin polarization is now allowed and it is constrained by the coplanar symmetry to be \mathcal{P} -symmetric in the momentum-space. To identify the symmetric spin ordering, we have rewritten the non-trivial spin point group using conventional crystallographic point groups, in the following form:

$$\mathbf{R}_s^B = \left([E||\mathbf{H}] + [C_{2z}||\mathbf{G} - \mathbf{H}] \right) \times \left\{ [E||E], [C_{2v}||\mathcal{P}] \right\}, \quad (4.7)$$

where $\mathbf{G} = 6mm$ and $\mathbf{H} = 3m$ are crystallographic point groups. Here, we note a similarity between the first term in parentheses and the spin point group of the collinear g-wave altermagnetic phase of EuIn_2As_2 discussed in Chapter 1. The spin rotation C_{2z}

has an axis orthogonal to the in-plane spins, analogous to the C_2 spin rotation in an altermagnetic point group [57]. This indicates that the in-plane spin components will exhibit a g -wave order with four spin-unpolarized nodal planes protected by the mirror symmetries: $[C_{2z}||m_v]$, $[C_{2z}||m_{v'}]$, $[C_{2z}||m_{v''}]$, and $[C_{2z}||m_z]$.

Another key symmetry in Eq. 4.7 is $[C_{2v}||\mathcal{P}]$, which enforces a pure g -wave order on S_v , while vanishing S_u . Notably, the v -axis defined in Fig. 4.9(a), aligns with the direction of the collinear order associated with the \mathbf{Q}_2 propagation vector. Furthermore, the antisymmetric order of S_z imposed by the coplanar symmetry, along with the preserved $[C_{2z}||C_{2z}]$ symmetry, allows the existence of a p -wave order in the broken-helical phase as well. Interestingly, this phase allows a mixed even and odd parity character on its spin polarization.

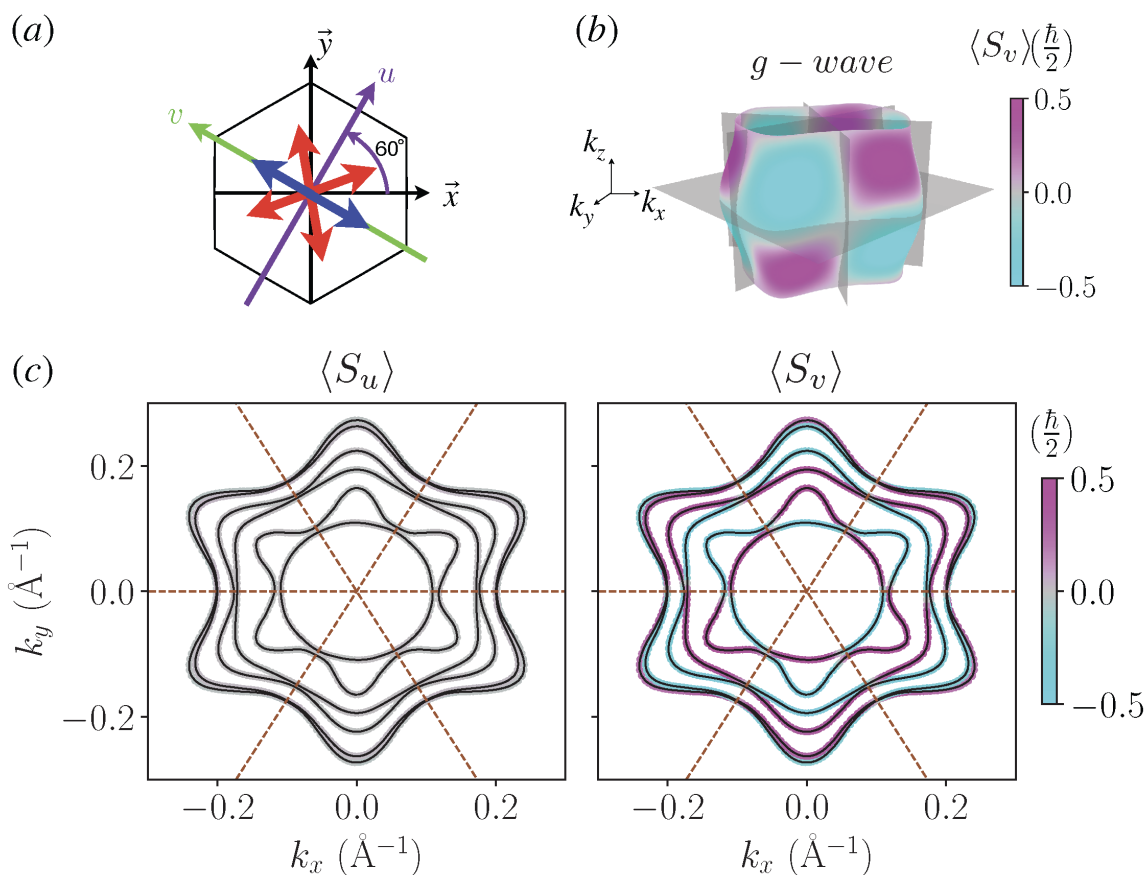


Figure 4.9: **Non-relativistic energy iso-surface of the broken-helical phase:** (a) The orthogonal spin axes u (violet), and v (green), which are chosen to visualize the in-plane g -wave order. (b) Sied view of S_v spin-polarized energy iso-surface at $E = +0.60$ eV, featuring a g -wave order with four un-polarized nodal planes. (c) S_u and S_v spin-polarized energy iso-surfaces at $E = E_F + 0.60$ eV and at the $k_z = 0.2c$ plane. The mustard-dotted lines indicate the nodal planes.

The effective two-band Hamiltonian of the broken helical phase constructed using

all the spin symmetry generators of \mathbf{R}_s^B is given by

$$h(\mathbf{k}) = \left(A (k_x^2 + k_y^2) + B k_z^2 \right) \sigma_0 + C k_z \sigma_z + D k_y k_z \left((\sqrt{3} k_x)^2 - k_y^2 \right) \vec{\sigma} \cdot \hat{v}. \quad (4.8)$$

Here, $\hat{v} = \{1, -\sqrt{3}/3, 0\}$ is an in-plane vector that points along the v axis. In contrast to the helical phase, the broken-helical introduces a third term in the Hamiltonian that captures the g -wave order of S_v . The emergence of a \mathcal{P} -symmetric spin polarization is expected, as $\mathcal{T}\tau$ is broken.

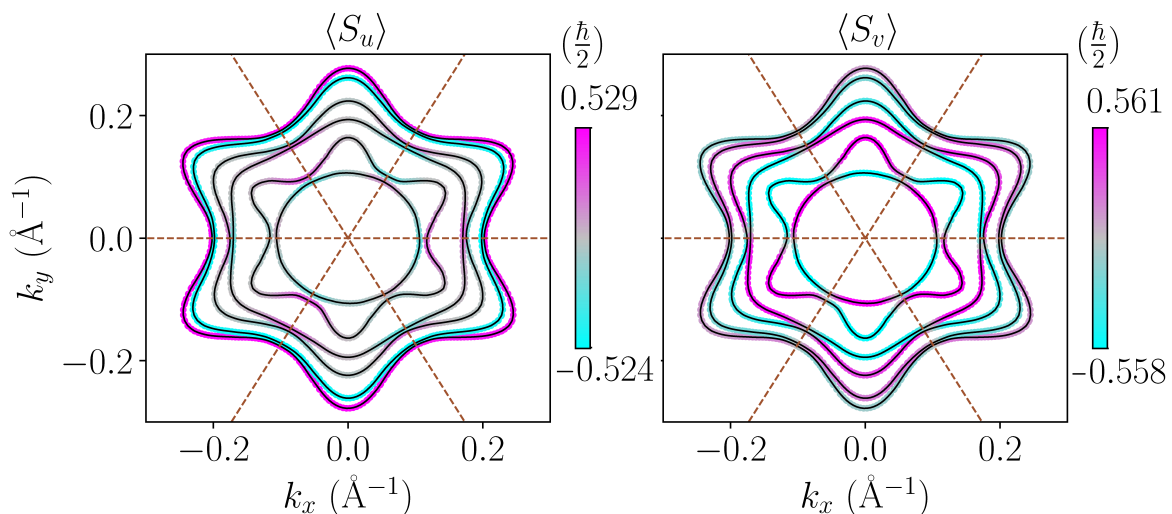


Figure 4.10: **GGA+U+SOC energy iso-surface of the broken-helical phase:** Momentum-space $S_u(S_v)$ spin-polarized energy iso-surfaces at the $k_z = 0.2c$ plane, for an energy $E = E_F + 0.60$ eV.

Next, we carry out the non-relativistic electronic structure calculations, again selecting the $L - \Gamma - m_z(L)$ path, as it does not lie on any spin-unpolarized plane, then allowing to visualize the spin-splittings. In Fig. 4.8 we show the spin-polarized bands with the spin components along the conventional xyz axis. Pronounced in-plane spin splittings are observed, exceeding those of S_z , which are significantly reduced compared to the helical phase.

By setting the spin axes along uv , which are axes highlighted in Fig. 4.9(a), we plot the S_v spin-polarized energy iso-surface shown in Fig 4.8(b), which features the bulk g -wave order with four nodal planes: one at $k_z = 0$ and the three others oriented perpendicular to it. Figure 4.9(c), further illustrates the energy iso-surfaces at the $k_z = 0.2c$ plane, confirming the vanishing of S_u and the presence of a pure g -wave order for S_v , with their opposite spin polarizations connected by the spin symmetry $[C_{2z}||C_{6z}]$, in agreement with our symmetry analysis.

Including SOC, now allows regions with non-zero S_u spin polarization, as shown in Fig. 4.10(right). Meanwhile, the g -wave character of S_v remains mostly unchanged

and SOC does not substantially change the magnitude of the spin-splittings, as shown in Fig. 4.10(left).

Our results show that the magnetic orderings identified through spin symmetries are quite robust under SOC effects and they may influence the transport properties of EuIn_2As_2 . A symmetry allowed response arising from the antisymmetric p -wave order is the Edelstein effect, which we discuss in the next section.

4.5 Non-relativistic linear Edelstein effect

The Edelstein effect refers to the generation a non-equilibrium spin polarization, or spin-density accumulation, induced by an applied electric field. Traditionally, this effect has been attributed to the Rashba spin-orbit coupling, which induces an in-plane antisymmetric spin texture characterized by a momentum-dependent spin orientation; and which under an electric field, it leads to an in-plane non-equilibrium spin polarization [187–191]. However, recent studies have revealed that a non-relativistic Edelstein effect is also possible in non-collinear, non-centrosymmetric materials featuring an antisymmetric spin texture [61, 62]. In particular, Ref. [61] reports a large out-of-plane non-equilibrium spin polarization, in contrast to the Rashba Edelstein effect.

The non-equilibrium spin polarization can be evaluated via the Kubo linear response theory [188, 192] as $\delta s_i = \chi_{ij} E_j$, where χ_{ij} denotes the spin-current response tensor and E the applied uniform electric field. The explicit form of χ_{ij} is given by,

$$\chi_{i,j} = \frac{1}{2\pi} \text{Re} \sum_{\mathbf{k}, n, m} s_{nm}^i(\mathbf{k}) v_{mn}^j(\mathbf{k}) \left[G_n^R(\mathbf{k}) G_m^A(\mathbf{k}) - G_n^R(\mathbf{k}) G_m^R(\mathbf{k}) \right]. \quad (4.9)$$

Here, s_{nm}^i and v_{mn}^j denote the matrix elements of the spin and velocity operators, respectively. The functions $G_n^{R/A}(\mathbf{k}) = 1/(E_n(\mathbf{k}) - E_F \pm i\Gamma)$ are the retarded and advanced Green's functions at the energy $E_{\mathbf{k}n}$, evaluated at the fermi level E_F , with Γ accounting for a constant spectral broadening determined by the quasiparticle lifetime.

This response tensor can be decomposed into two contributions, $\chi = \chi^{intra} + \chi^{inter}$, the intraband and interband terms. In the limit of weak disorder, i.e., $\Gamma \rightarrow 0$ and assuming a constant Γ , the intraband spin polarization term is given by [188, 193, 194],

$$\delta \mathbf{s}^{intra} = \frac{e\hbar}{2\Gamma} \int \frac{d\mathbf{k}}{(2\pi)^3} \sum_n \mathbf{s}_{nn}(\mathbf{k}) (\mathbf{E} \cdot \mathbf{v}(\mathbf{k}))_{nn} \delta(E_n(\mathbf{k}) - E_F). \quad (4.10)$$

This contribution contains only the diagonal components and it is proportional to $1/\Gamma$ and is therefore an *extrinsic* contribution as it is impurity dependent. In addition, $\delta \mathbf{s}^{intra}$ is invariant under \mathcal{T} symmetry, meaning it is forbidden in \mathcal{T} -symmetry broken magnetic orderings such as in the case of ferromagnets and altermagnets, while it exists in \mathcal{T} -symmetric magnetic orderings such the odd-parity-wave orderings.

The interband spin polarization term is given by,

$$\delta \mathbf{s}^{inter} = 2e\hbar \int \frac{d\mathbf{k}}{(2\pi)^3} \sum_{n \neq m} (f_n(\mathbf{k}) - f_m(\mathbf{k})) \text{Im}[\mathbf{s}_{nm} (\mathbf{E} \cdot \mathbf{v}(\mathbf{k}))_{mn}] \times \frac{(E_n(\mathbf{k}) - E_m(\mathbf{k}))^2 - \Gamma^2}{[(E_n(\mathbf{k}) - E_m(\mathbf{k}))^2 + \Gamma^2]^2}. \quad (4.11)$$

This contribution contains the off-diagonal components and since it is independent of Γ in the clean limit, it is an *intrinsic* contribution. Here, $f_n(\mathbf{k})$ denotes the Fermi distribution function. In contrast to the intraband term, the interband term is odd under \mathcal{T} , consequently, it vanishes in \mathcal{T} -symmetric magnetic orderings.

Table 4.1: Symmetry constrained intraband and interband response tensor of helical and broken-helical phases. The response tensor is expressed in the lattice coordinates. For the non-relativistic case, the spin-point group generators are applied, while for the relativistic case, magnetic-point group generators are employed

	Without SOC	With SOC
Helical	$\chi^{intra} = \begin{pmatrix} 0 & 0 & 0 \\ 0 & 0 & 0 \\ 0 & 0 & \chi_{cc} \end{pmatrix}$	$\begin{pmatrix} \chi_a & \chi_a/2 & 0 \\ \chi_a/2 & \chi_a & 0 \\ 0 & 0 & \chi_{cc} \end{pmatrix}$
	$\chi^{inter} = \begin{pmatrix} 0 & 0 & 0 \\ 0 & 0 & 0 \\ 0 & 0 & 0 \end{pmatrix}$	$\begin{pmatrix} 0 & \chi_b & 0 \\ -\chi_b & 0 & 0 \\ 0 & 0 & 0 \end{pmatrix}$
Broken Helical	$\chi^{intra} = \begin{pmatrix} 0 & 0 & 0 \\ 0 & 0 & 0 \\ 0 & 0 & \chi_{cc} \end{pmatrix}$	$\begin{pmatrix} \chi_a & \chi_b & 0 \\ \chi_b & \chi_a & 0 \\ 0 & 0 & \chi_{cc} \end{pmatrix}$
	$\chi^{inter} = \begin{pmatrix} 0 & 0 & 0 \\ 0 & 0 & 0 \\ 0 & 0 & 0 \end{pmatrix}$	$\begin{pmatrix} \chi_a & \chi_b & 0 \\ -\chi_b & -\chi_a & 0 \\ 0 & 0 & 0 \end{pmatrix}$

As previously reported, the non-centrosymmetric helical and broken-helical phases of EuIn_2As_2 exhibit a S_z p-wave order, which effectively preserves \mathcal{T} symmetry in momentum-space, even though \mathcal{T} is not a symmetry operation of the point group itself. Consequently, an Edelstein effect is expected for both configurations in the absence of SOC. Before evaluating the magnitude of this effect, we first analyze the symmetry constraints on the response tensor χ_{ij} imposed by the spin point group and magnetic point group generators (see Table 4.1 and Appendix A for more details). In the absence of SOC, only the intraband spin polarization along the coplanar axis $\hat{\mathbf{z}}$ is allowed in both non-collinear states, while the interband contribution vanishes, reflecting the effective \mathcal{T} -symmetric magnetic ordering of S_z . In other words, applying an electric field along

the z -axis generates a non-equilibrium out-of-plane spin polarization, analogous to the behavior reported in [61]. Now, when SOC is included, additional in-plane intraband components become allowed, and the interband contribution becomes possible.

From the symmetry analysis, we find that only the intraband contribution is directly linked to the non-relativistic p -wave spin ordering. We compute this contribution with and without SOC in Fig. 4.11. Within the energy window $E = E_F \pm 1$ eV, the helical phase exhibits spin density δs_z values larger than those in the broken-helical phase, which is consistent with the observation of S_z spin splittings in the helical phase with magnitudes larger than those in the broken-helical. On the other hand, the Edelstein response in the helical phase has a magnitude comparable to the responses reported in $\mathcal{T}\tau$ p -wave magnets [61, 80], which are known to exhibit a giant response. Near the Fermi level, $E = E_F \pm 0.3$ eV, the magnitude of the intraband responses can be approximately related by a factor of $\chi_{zz}^{\text{helical}}/\chi_{zz}^{\text{broken}} \approx 5$. Introducing SOC has a minimal effect on the out-of-plane spin density values, which aligns with the subtle breaking of the p -wave spin ordering upon including SOC, as seen in Fig. 4.7(a).

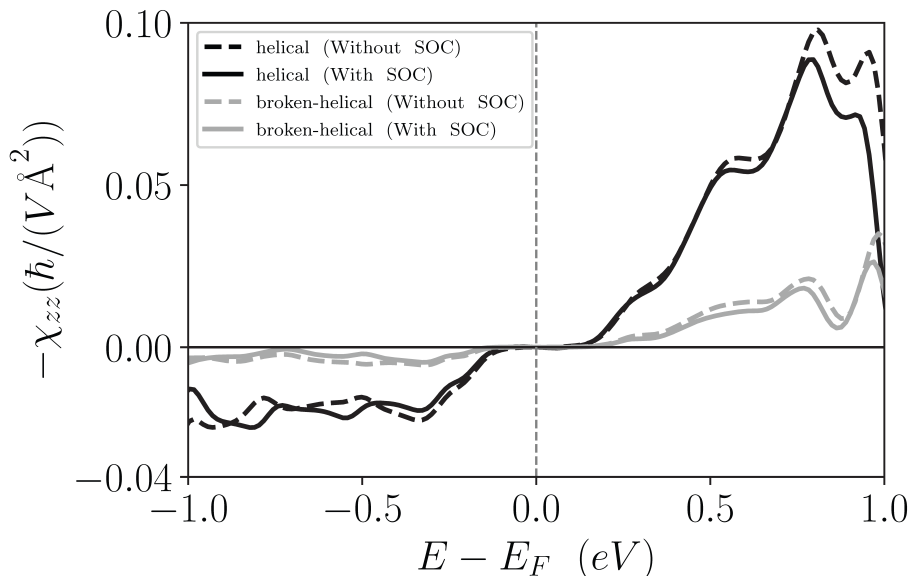


Figure 4.11: **Intraband out-of-plane response tensor χ_{zz} for both the helical and broken-helical states:** Calculations with and without spin-orbit coupling correspond to solid-line and dashed-line, respectively. We consider a disorder value of $\Gamma = 0.01$ eV. The effects of exchange dominate on the Edelstein response compared with the minimal effects due to SOC. The helical phase exhibits a significantly larger response than the broken-helical.

In addition, we normalize the intraband Edelstein response by the longitudinal conductivity calculated using the linear response Equation 4.12. Since both responses scale disorder scattering as $1/\Gamma$, the normalized intraband Edelstein response in Fig.4.12(b) is now a disorder independent response, and still shows spin density values for the helical phase surpassing four times the ones in the broken-helical. Although the spin

density vanishes at the Fermi level, EuIn_2As_2 is experimentally known to be highly hole-doped [195–197], which could already lead to a sizable Edelstein response.

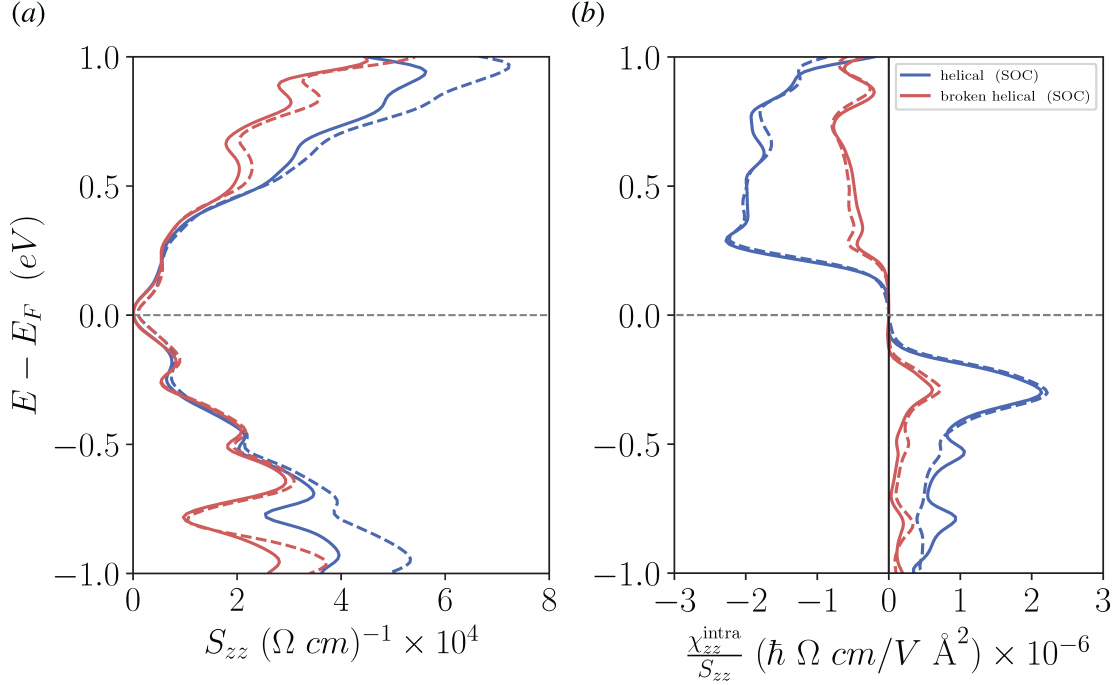


Figure 4.12: **Longitudinal conductivity and scattering time independent spin density:** (a) The ohmic conductivity S_{zz} for the helical (red) and broken-helical (blue) phases including SOC (solid line), and without SOC (dashed lines). (b) The normalized intraband spin density, resulting in a disorder independent response.

$$S_{ij} = \frac{e^2}{\Gamma \hbar} \int \frac{d\mathbf{k}}{(2\pi)^3} \sum_n \text{Re}[(\hat{v}_i)_{nn}(\hat{v}_j)_{nn}] \times \delta(E_n(\mathbf{k}) - E_F), \quad (4.12)$$

This significant difference in the out-of-plane spin density values between both phases could serve as a way of detecting the magnetic transition via transport measurements, in contrast to other transport quantities, such as the longitudinal conductivity, which also shows differences between both phases but to a lesser extent, as seen in Fig. 4.12(a).

In Fig. 4.13, we show the in-plane intraband response that emerges upon including SOC. The results are consistent with the symmetry constraints listed in Table 4.1, and their magnitudes are approximately an order of magnitude smaller than the dominant out-of-plane response.

A final important point with regards to the measurement of the Edelstein effect, is that its presence – or absence – will also serve to validate or discard the proposed amplitude modulated phases in Ref. [66], since both their A_1 (P symmetric) and A_2 (PT symmetric) phases would not allow an Edelstein effect.

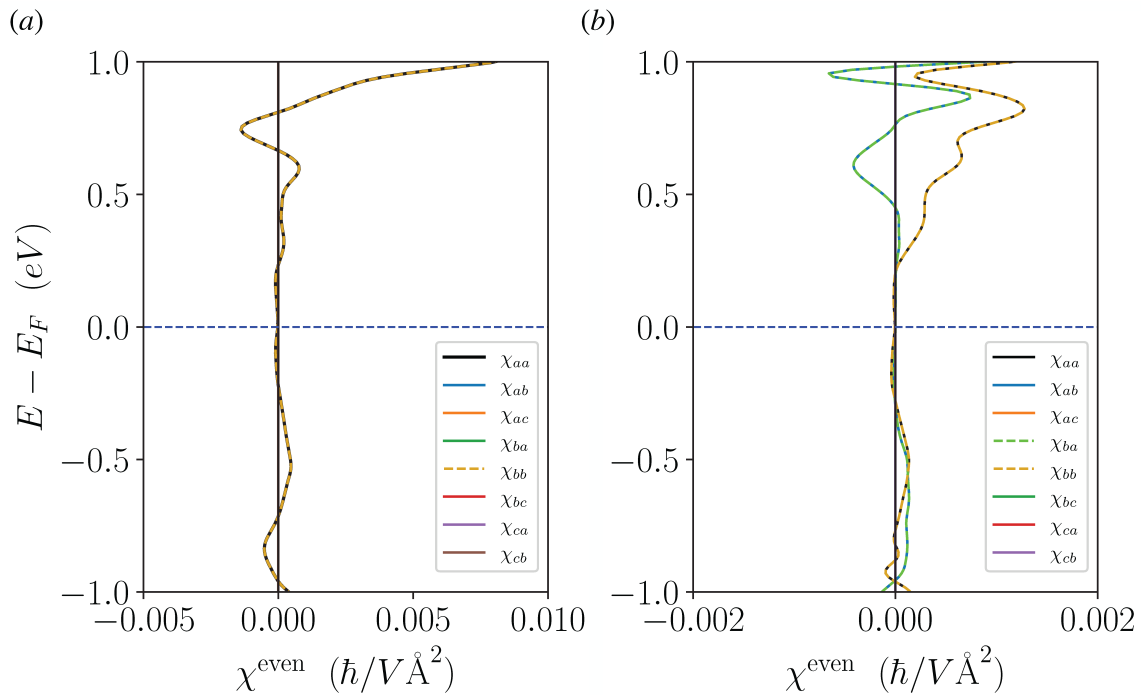


Figure 4.13: **Intraband response tensor $\chi_{i,j}$ including SOC:** Computed response tensor for (a) the helical and (b) broken-helical phases assuming $\Gamma = 0.01$ eV.

4.6 Summary

Direct-space	Momentum-space	
<p>Helical</p> <p>Non-collinear</p>	<p>p-wave</p> <p>Collinear spin-ordering</p>	
<p>Broken-Helical</p> <p>Non-collinear</p>	<p>p-wave</p>	<p>g-wave</p>
	<p>Non-collinear spin-ordering</p>	

In this Chapter, we have investigated two commensurate non-collinear coplanar phases reported in EuIn_2As_2 , as the "helical" phase and the "broken-helical" phase, the latter arising from a superposition of a helical state and a compensated collinear state. Our

spin symmetry analysis and non-relativistic electronic calculations show that exchange alone induces a spin-ordering in the electronic structure in both phases.

In the helical state, we identify a collinear S_z spin polarization with a p-wave character. This collinearity in momentum-space results from the presence of pure spin-translation symmetries in real-space. Although the helical phase breaks \mathcal{T} symmetry as a point group operation, it still allows for a \mathcal{T} -symmetric spin-ordering, but only in the limit of zero SOC. In contrast, the broken-helical phase hosts the same p-wave order and an additional in-plane spin polarization with a g-wave character.

With SOC included, we find that the spin-orderings and spin-splitting magnitudes remain mostly unchanged, indicating they may play an important role in the transport of EuIn_2As_2 . Here, we computed the Edelstein effect, originating from the antisymmetric p-wave order, and we identified a distinctive out-of-plane polarized spin density in both phases. Remarkably, the helical phase exhibits a giant response, comparable to that reported in $\mathcal{T}\tau$ p-wave magnets [61]. As a final remark, this anisotropic response also offers a way to distinguish the non-collinear phases studied here from the recently proposed amplitude-modulated collinear phases [66], which cannot realize such effect even in the presence of SOC.

Concluding remarks

In this Thesis we have studied – through a symmetry-based framework – the electronic structure of two compensated Eu-based compounds: the conventional $\mathcal{T}\tau$ antiferromagnet EuCd_2As_2 , which exhibits Kramers spin degeneracy in momentum-space, and the compensated EuIn_2As_2 which instead shows spin-split bands in momentum-space even in the absence of spin-orbit coupling effects.

In Chapter 1, we introduce two symmetry frameworks that are used for characterizing magnetic materials. We start reviewing *magnetic symmetries*, that only allows the application of the same symmetry operators in both the real-space and spin-space, reflecting the coupling between these two spaces. This symmetry framework have been to date mostly used to explore the topological properties in crystals, thereby, within this framework we summarize the distinct topological phases reported in compensated magnets, followed by their corresponding topological invariants, and relevant symmetries protecting these states. We also introduce the formalism of magnetic topological quantum chemistry, that we used to characterize the topological nature of our electronic band structures. Furthermore, we review the framework of *spin symmetries*, which unlike magnetic symmetries, the spin-space and real-space are decoupled, allowing different symmetry transformations to act simultaneously in the real-space and spin-space. Within this framework we review how to build the *spin point groups* based on Litvins approach [53, 54], and we implement this to identify the *g-wave* altermagnetic phase of the collinear phase of EuIn_2As_2 .

In Chapter 2 we provide a description of the density functional theory (DFT) implemented within VASP that we used to calculate the electronic band structures of our model systems. We discuss the several approximations that we have taken into account, from Hubbard corrections and spin-orbit coupling effects. We also discussed the importance of constraining the magnetic moments to converge to non-collinear magnetic ground-states that preserve the symmetries of interest. We also discussed how to construct tight-binding Hamiltonians from our DFT electronic structures, by using the atom-centered Wannier functions. We later used these tight-binding models to evaluate the surface states of EuCd_2As_2 and the spin-dependent transport responses in EuIn_2As_2 .

In Chapter 3, we analyzed the band topology and the corresponding surface states of the collinear antiferromagnetic (AFM) phases of EuCd_2As_2 , both with and without

strain effects [52]. In the unstrained case, we confirm the existence of a stable Dirac semimetal phase (DSM) protected by an additional rotational C_{3z} symmetry in the out-of-plane AFM order, and an Axion insulator phase (AXI) that coexist with a topological crystalline insulator phase in the in-plane AFM order. Applying in-plane shear strains, we show that the transition from the DSM phase to the AXI phase is possible inducing a band gap not only on the bulk but also on one of EuCd_2As_2 cleavage surfaces. The resulting gapped surface would support the emergence of hinge modes and contribute to the half quantized Hall conductivity – characteristic features of the axion insulator phase. Thus, shear strain offers an additional way for tuning the band topology and surface states in EuCd_2As_2 or related systems. We note, however, that recent optical experiments [198] and *ab initio* calculations using hybrid exchange-correlation functionals [64] suggest that EuCd_2As_2 may behave as a trivial semiconductor rather than a topological magnet. Nevertheless, our analysis can still be applied on related systems such as EuCd_2Bi_2 still considered as robust topological insulator [64].

In Chapter 4, motivated by reports of non-relativistic spin-splittings in EuIn_2As_2 , we examine the effects of exchange and crystal fields on the electronic structure of two experimentally observed coplanar, non-collinear compensated phases: the helical and the broken-helical states [69]. Using the framework of *spin symmetries*, we construct the corresponding spin point groups and identify relevant spin symmetries that shape the spin-polarization of the electronic band structure. To isolate the effects of exchange and crystal fields, we performed electronic structure calculations without spin-orbit coupling (SOC) effects. In the helical phase, we identify a p -wave order in the out-of-plane spin polarization that results in an effective collinear order in momentum-space, enforced by pure spin-translation symmetries of the form $[C_{3\perp}||\tau]$ – akin to the recently proposed $\mathcal{T}\tau$ p -wave magnets, which instead feature $[C_{2\perp}||\tau]$. In the broken-helical phase, the same p -wave order coexist with an additional g -wave order arising on the in-plane spin polarization. Such mixed odd/even character of the spin polarization in non-collinear coplanar systems are allowed as long as time-reversal symmetry \mathcal{T} is broken as a point group operation. Upon including SOC, these exchange-driven magnetic orderings remain robust in momentum-space, highlighting their potential impact on the transport and magneto-optical responses of EuIn_2As_2 and opening promising avenues to explore the interplay between the axion insulator phase and unconventional magnetism in this material. Our calculations of the Edelstein effect in both phases show a predominantly non-relativistic origin, primarily arising from the antisymmetric p -wave character of the out-of-plane spin polarization – distinct from the conventional in-plane spin density generated by the relativistic Rashba-Edelstein mechanism. Overall, these results underscore spin symmetries as a powerful framework for characterizing unconventional magnetic orderings in non-collinear systems – even in materials where SOC can be strong.

Appendix A

Symmetry transformation rules of the linear response tensor

According to Neumann's principle, the physical properties of a crystal must be invariant under all the symmetry operators of its point group [199]. For the linear Edelstein effect, $\delta s_a = \chi_{ab} E_b$, an applied electric field \mathbf{E} induces a non-equilibrium spin density $\delta \mathbf{s}$. The linear spin-current response tensor χ_{ab} can be decomposed into two contributions that are even or odd under time reversal \mathcal{T} symmetry,

$$\chi = \chi^{even} + \chi^{odd}. \quad (\text{A.1})$$

When spin-orbit coupling is taken into account, the symmetry operations of the crystal belong to the magnetic point groups with symmetry operators r that act simultaneously on both the spin-space and real-space. In this case, χ obeys the following symmetry transformation rules in the cartesian coordinates [194]:

$$\chi_{a'b'}^{even} = \det(\mathcal{R}) \mathcal{R}_{a'a} \mathcal{R}_{b'b} \chi_{ab}^{even}, \quad (\text{A.2})$$

and

$$\chi_{a'b'}^{odd} = \eta_{\mathcal{T}} \det(\mathcal{R}) \mathcal{R}_{a'a} \mathcal{R}_{b'b} \chi_{ab}^{odd}. \quad (\text{A.3})$$

Here, \mathcal{R} denotes a 3×3 matrix representations of the symmetry operator r . The term $\det(\mathcal{R})$ appears because the spin \mathbf{s} as axial vector, and \mathbf{v} as polar vector transform differently under improper symmetry operations. The additional factor $\eta_{\mathcal{T}} = -1$ under antiunitary transformations, otherwise $\eta_{\mathcal{T}} = +1$.

If spin-orbit coupling is neglected, spin point group generators of the form $[s||r]$ are applied with s acting exclusively on the spin-space and r on the real-space. In this case, the symmetry transformation rules are given by

$$\chi_{a'b'}^{even} = \mathcal{S}_{a'a} \mathcal{R}_{b'b} \chi_{ab}^{even}, \quad (\text{A.4})$$

and

$$\chi_{a'b'}^{odd} = \eta_T \mathcal{S}_{a'a} \mathcal{R}_{b'b} \chi_{ab}^{odd}. \quad (\text{A.5})$$

Here, \mathcal{S} denotes the matrix representations of the symmetry operators s . Note that the factor \det here, is not included as the spin-space within our notation transforms only under proper rotations $\mathcal{S} \in \text{SO}(3)$ with $\det(\mathcal{S}) = 1$.

Bibliography

- [1] L. Néel, “Propriétés magnétiques des ferrites; ferrimagnétisme et antiferromagnétisme,” in *Annales de physique*, vol. 12, pp. 137–198, 1948.
- [2] L. Néel, “Magnetism and local molecular field,” *Science*, vol. 174, no. 4013, pp. 985–992, 1971.
- [3] L. Néel, “Magnetism and the local molecular field,” *Nobel Lecture Physics 1970*, 1970.
- [4] E. Gomonay and V. Loktev, “Spintronics of antiferromagnetic systems,” *Low Temperature Physics*, vol. 40, no. 1, pp. 17–35, 2014.
- [5] P. Wadley, B. Howells, J. Železný, C. Andrews, V. Hills, R. P. Campion, V. Novák, K. Olejník, F. Maccherozzi, S. Dhesi, *et al.*, “Electrical switching of an antiferromagnet,” *Science*, vol. 351, no. 6273, pp. 587–590, 2016.
- [6] T. Jungwirth, X. Marti, P. Wadley, and J. Wunderlich, “Antiferromagnetic spintronics,” *Nature nanotechnology*, vol. 11, no. 3, pp. 231–241, 2016.
- [7] P. Němec, M. Fiebig, T. Kampfrath, and A. V. Kimel, “Antiferromagnetic optospintronics,” *Nature Physics*, vol. 14, no. 3, pp. 229–241, 2018.
- [8] K. Olejník, T. Seifert, Z. Kašpar, V. Novák, P. Wadley, R. P. Campion, M. Baumgartner, P. Gambardella, P. Němec, J. Wunderlich, *et al.*, “Terahertz electrical writing speed in an antiferromagnetic memory,” *Science advances*, vol. 4, no. 3, p. eaar3566, 2018.
- [9] T. Jungwirth, R. Fernandes, E. Fradkin, A. MacDonald, J. Sinova, and L. Smejkal, “Altermagnetism: an unconventional spin-ordered phase of matter,” *arXiv preprint arXiv:2411.00717*, 2025.
- [10] T. Jungwirth, J. Sinova, R. M. Fernandes, Q. Liu, H. Watanabe, S. Murakami, S. Nakatsuji, and L. Smejkal, “Symmetry, microscopy and spectroscopy signatures of altermagnetism,” *arXiv preprint arXiv:2506.22860*, 2025.
- [11] B. A. Bernevig, C. Felser, and H. Beidenkopf, “Progress and prospects in magnetic topological materials,” *Nature*, vol. 603, no. 7899, pp. 41–51, 2022.

- [12] L. Šmejkal, Y. Mokrousov, B. Yan, and A. H. MacDonald, “Topological antiferromagnetic spintronics,” *Nature physics*, vol. 14, no. 3, pp. 242–251, 2018.
- [13] J.-P. Hanke, F. Freimuth, C. Niu, S. Blügel, and Y. Mokrousov, “Mixed weyl semimetals and low-dissipation magnetization control in insulators by spin–orbit torques,” *Nature Communications*, vol. 8, no. 1, p. 1479, 2017.
- [14] A. Dal Din, O. Amin, P. Wadley, and K. Edmonds, “Antiferromagnetic spintronics and beyond,” *npj Spintronics*, vol. 2, no. 1, p. 25, 2024.
- [15] P. Tang, Q. Zhou, G. Xu, and S.-C. Zhang, “Dirac fermions in an antiferromagnetic semimetal,” *Nature Physics*, vol. 12, no. 12, pp. 1100–1104, 2016.
- [16] K. Kuroda, T. Tomita, M.-T. Suzuki, C. Bareille, A. Nugroho, P. Goswami, M. Ochi, M. Ikhlas, M. Nakayama, S. Akebi, *et al.*, “Evidence for magnetic weyl fermions in a correlated metal,” *Nature materials*, vol. 16, no. 11, pp. 1090–1095, 2017.
- [17] J. Kübler and C. Felser, “Weyl fermions in antiferromagnetic mn₃sn and mn₃ge,” *Europhysics Letters*, vol. 120, no. 4, p. 47002, 2018.
- [18] J. Schütte-Engel, D. J. Marsh, A. J. Millar, A. Sekine, F. Chadha-Day, S. Hoof, M. N. Ali, K. C. Fong, E. Hardy, and L. Šmejkal, “Axion quasiparticles for axion dark matter detection,” *Journal of Cosmology and Astroparticle Physics*, vol. 2021, no. 08, p. 066, 2021.
- [19] A. Sekine and K. Nomura, “Axion electrodynamics in topological materials,” *Journal of Applied Physics*, vol. 129, no. 14, 2021.
- [20] G.-G. Liu, S. Mandal, X. Xi, Q. Wang, C. Devescovi, A. Morales-Pérez, Z. Wang, L. Yang, R. Banerjee, Y. Long, *et al.*, “Photonic axion insulator,” *Science*, vol. 387, no. 6730, pp. 162–166, 2025.
- [21] L. Šmejkal, J. Železný, J. Sinova, and T. Jungwirth, “Electric control of dirac quasiparticles by spin-orbit torque in an antiferromagnet,” *Physical review letters*, vol. 118, no. 10, p. 106402, 2017.
- [22] H. Yang, Y. Sun, Y. Zhang, W.-J. Shi, S. S. Parkin, and B. Yan, “Topological weyl semimetals in the chiral antiferromagnetic materials mn₃ge and mn₃sn,” *New Journal of Physics*, vol. 19, no. 1, p. 015008, 2017.
- [23] J. Liu and L. Balents, “Anomalous hall effect and topological defects in antiferromagnetic weyl semimetals: Mn₃sn/ge,” *Physical review letters*, vol. 119, no. 8, p. 087202, 2017.

- [24] J. Ma, H. Wang, S. Nie, C. Yi, Y. Xu, H. Li, J. Jandke, W. Wulfhekel, Y. Huang, D. West, *et al.*, “Emergence of nontrivial low-energy dirac fermions in antiferromagnetic eucd₂as₂,” *Advanced Materials*, vol. 32, no. 14, p. 1907565, 2020.
- [25] Y. Xu, Z. Song, Z. Wang, H. Weng, and X. Dai, “Higher-order topology of the axion insulator EuIn₂As₂,” *Physical review letters*, vol. 122, no. 25, p. 256402, 2019.
- [26] Y. Zhao, Y. Jiang, H. Bae, K. Das, Y. Li, C.-X. Liu, and B. Yan, “Hybrid-order topology in unconventional magnets of eu-based zintl compounds with surface-dependent quantum geometry,” *Physical Review B*, vol. 110, no. 20, p. 205111, 2024.
- [27] H. Reichlova, D. Kriegner, A. Mook, M. Althammer, and A. Thomas, “Role of topology in compensated magnetic systems,” *APL Materials*, vol. 12, no. 1, 2024.
- [28] B. Bradlyn, L. Elcoro, J. Cano, M. G. Vergniory, Z. Wang, C. Felser, M. I. Aroyo, and B. A. Bernevig, “Topological quantum chemistry,” *Nature*, vol. 547, no. 7663, pp. 298–305, 2017.
- [29] L. Elcoro, B. J. Wieder, Z. Song, Y. Xu, B. Bradlyn, and B. A. Bernevig, “Magnetic topological quantum chemistry,” *Nature communications*, vol. 12, no. 1, p. 5965, 2021.
- [30] Y. Xu, L. Elcoro, Z.-D. Song, B. J. Wieder, M. G. Vergniory, N. Regnault, Y. Chen, C. Felser, and B. A. Bernevig, “High-throughput calculations of magnetic topological materials,” *Nature*, vol. 586, no. 7831, pp. 702–707, 2020.
- [31] H. Tsai, T. Higo, K. Kondou, T. Nomoto, A. Sakai, A. Kobayashi, T. Nakano, K. Yakushiji, R. Arita, S. Miwa, *et al.*, “Electrical manipulation of a topological antiferromagnetic state,” *Nature*, vol. 580, no. 7805, pp. 608–613, 2020.
- [32] T. Chen, T. Tomita, S. Minami, M. Fu, T. Koretsune, M. Kitatani, I. Muhammad, D. Nishio-Hamane, R. Ishii, F. Ishii, *et al.*, “Anomalous transport due to weyl fermions in the chiral antiferromagnets mn₃x, x= sn, ge,” *Nature communications*, vol. 12, no. 1, p. 572, 2021.
- [33] A. Low, S. Ghosh, S. Changdar, S. Routh, S. Purwar, and S. Thirupathaiiah, “Tuning of topological properties in the strongly correlated antiferromagnet mn₃sn via fe doping,” *Physical Review B*, vol. 106, no. 14, p. 144429, 2022.
- [34] A. Valadkhani, M. Iraola, A. Fünfhaus, Y.-J. Song, L. Šmejkal, J. Sinova, and R. Valentí, “Influence of magnetism, strain, and pressure on the band topology of eucd₂as₂,” *Physical Review B*, vol. 108, no. 23, p. 235113, 2023.

- [35] C. W. Hicks, F. Jerzembeck, H. M. Noad, M. E. Barber, and A. P. Mackenzie, “Probing quantum materials with uniaxial stress,” *Annual Review of Condensed Matter Physics*, vol. 16, 2024.
- [36] Y. Liu, Y. Li, S. Rajput, D. Gilks, L. Lari, P. Galindo, M. Weinert, V. Lazarov, and L. Li, “Tuning dirac states by strain in the topological insulator Bi_2Se_3 ,” *Nature Physics*, vol. 10, no. 4, pp. 294–299, 2014.
- [37] E. Gati, S. L. Bud’ko, L.-L. Wang, A. Valadkhani, R. Gupta, B. Kuthanazhi, L. Xiang, J. M. Wilde, A. Sapkota, Z. Guguchia, *et al.*, “Pressure-induced ferromagnetism in the topological semimetal EuCd_2As_2 ,” *Physical Review B*, vol. 104, no. 15, p. 155124, 2021.
- [38] M. C. Rahn, J.-R. Soh, S. Francoual, L. Veiga, J. Strempler, J. Mardegan, D. Yan, Y. Guo, Y. Shi, and A. Boothroyd, “Coupling of magnetic order and charge transport in the candidate dirac semimetal EuCd_2As_2 ,” *Physical Review B*, vol. 97, no. 21, p. 214422, 2018.
- [39] G. Hua, S. Nie, Z. Song, R. Yu, G. Xu, and K. Yao, “Dirac semimetal in type-iv magnetic space groups,” *Physical Review B*, vol. 98, no. 20, p. 201116, 2018.
- [40] S. X. Riberolles, T. V. Trevisan, B. Kuthanazhi, T. Heitmann, F. Ye, D. Johnston, S. Bud’ko, D. Ryan, P. Canfield, A. Kreyssig, *et al.*, “Magnetic crystalline-symmetry-protected axion electrodynamics and field-tunable unpinned dirac cones in EuIn_2As_2 ,” *Nature communications*, vol. 12, no. 1, p. 999, 2021.
- [41] M. Arguilla, N. Cultrara, Z. Baum, S. Jiang, R. Ross, and J. Goldberger, “ EuSn_2 as 2: an exfoliatable magnetic layered zintl–klemm phase,” *Inorganic Chemistry Frontiers*, vol. 4, no. 2, pp. 378–386, 2017.
- [42] H. Li, S.-Y. Gao, S.-F. Duan, Y.-F. Xu, K.-J. Zhu, S.-J. Tian, J.-C. Gao, W.-H. Fan, Z.-C. Rao, J.-R. Huang, *et al.*, “Dirac surface states in intrinsic magnetic topological insulators EuSn_2 as 2 and MnBi_2Te_3 as 1,” *Physical Review X*, vol. 9, no. 4, p. 041039, 2019.
- [43] G. M. Pierantozzi, A. De Vita, C. Bigi, X. Gui, H.-J. Tien, D. Mondal, F. Mazzola, J. Fujii, I. Vobornik, G. Vinai, *et al.*, “Evidence of magnetism-induced topological protection in the axion insulator candidate EuSn_2P_2 ,” *Proceedings of the National Academy of Sciences*, vol. 119, no. 4, p. e2116575119, 2022.
- [44] Z.-C. Wang, J. D. Rogers, X. Yao, R. Nichols, K. Atay, B. Xu, J. Franklin, I. Sochnikov, P. J. Ryan, D. Haskel, *et al.*, “Colossal magnetoresistance without mixed valence in a layered phosphide crystal,” *Advanced Materials*, vol. 33, no. 10, p. 2005755, 2021.

- [45] Z.-C. Wang, E. Been, J. Gaudet, G. M. A. Alqasseri, K. Fruhling, X. Yao, U. Stuhr, Q. Zhu, Z. Ren, Y. Cui, *et al.*, “Anisotropy of the magnetic and transport properties of EuZn_2As_2 ,” *Physical Review B*, vol. 105, no. 16, p. 165122, 2022.
- [46] J.-Z. Ma, S. Nie, C. Yi, J. Jandke, T. Shang, M.-Y. Yao, M. Naamneh, L. Yan, Y. Sun, A. Chikina, *et al.*, “Spin fluctuation induced weyl semimetal state in the paramagnetic phase of eucl_2as_2 ,” *Science advances*, vol. 5, no. 7, p. eaaw4718, 2019.
- [47] J.-R. Soh, F. De Juan, M. Vergniory, N. Schröter, M. C. Rahn, D. Yan, J. Jiang, M. Bristow, P. Reiss, J. Blandy, *et al.*, “Ideal weyl semimetal induced by magnetic exchange,” *Physical Review B*, vol. 100, no. 20, p. 201102, 2019.
- [48] N. H. Jo, B. Kuthanazhi, Y. Wu, E. Timmons, T.-H. Kim, L. Zhou, L.-L. Wang, B. G. Ueland, A. Palasyuk, D. H. Ryan, *et al.*, “Manipulating magnetism in the topological semimetal eucl_2as_2 ,” *Physical Review B*, vol. 101, no. 14, p. 140402, 2020.
- [49] Y. Sun, Y. Li, S. Li, C. Yi, H. Deng, X. Du, L. Liu, C. Zhu, Y. Li, Z. Wang, *et al.*, “Experimental evidence for field-induced metamagnetic transition of eucl_2as_2 ,” *Journal of Rare Earths*, vol. 40, no. 10, pp. 1606–1610, 2022.
- [50] G. C. Jose, K. Burrage, J. L. G. Jimenez, W. Xie, B. Lavina, J. Zhao, E. E. Alp, D. Zhang, Y. Xiao, Y. K. Vohra, *et al.*, “Evolution of magnetism, valence, and crystal lattice in EuCd_2As_2 under pressure,” *Physical Review B*, vol. 107, no. 24, p. 245121, 2023.
- [51] B. Li, W. Sun, X. Zou, X. Li, B. Huang, Y. Dai, and C. Niu, “Switchable quantum anomalous and spin hall effects in honeycomb magnet eucl_2as_2 ,” *New Journal of Physics*, vol. 24, no. 5, p. 053038, 2022.
- [52] N. A. Á. Pari, V. K. Bharadwaj, R. Jaeschke-Ubiergo, A. Valadkhani, R. Valentí, L. Šmejkal, and J. Sinova, “Strain control of band topology and surface states in antiferromagnetic eucl_2as_2 ,” *Physical Review B*, vol. 109, no. 19, p. 195117, 2024.
- [53] D. B. Litvin and W. Opechowski, “Spin groups,” *Physica*, vol. 76, no. 3, pp. 538–554, 1974.
- [54] D. B. Litvin, “Spin point groups,” *Foundations of Crystallography*, vol. 33, no. 2, pp. 279–287, 1977.
- [55] P. Liu, J. Li, J. Han, X. Wan, and Q. Liu, “Spin-group symmetry in magnetic materials with negligible spin-orbit coupling,” *Physical Review X*, vol. 12, no. 2, p. 021016, 2022.

- [56] L. Šmejkal, J. Sinova, and T. Jungwirth, “Emerging research landscape of alter-magnetism,” *Physical Review X*, vol. 12, no. 4, p. 040501, 2022.
- [57] L. Šmejkal, J. Sinova, and T. Jungwirth, “Beyond conventional ferromagnetism and antiferromagnetism: A phase with nonrelativistic spin and crystal rotation symmetry,” *Physical Review X*, vol. 12, no. 3, p. 031042, 2022.
- [58] K. Samanta, M. Ležaić, M. Merte, F. Freimuth, S. Blügel, and Y. Mokrousov, “Crystal hall and crystal magneto-optical effect in thin films of srruo3,” *Journal of applied physics*, vol. 127, no. 21, 2020.
- [59] R. González-Hernández, L. Šmejkal, K. Vyborný, Y. Yahagi, J. Sinova, T. Jungwirth, and J. Železný, “Efficient electrical spin splitter based on nonrelativistic collinear antiferromagnetism,” *Physical Review Letters*, vol. 126, no. 12, p. 127701, 2021.
- [60] L. Šmejkal, R. González-Hernández, T. Jungwirth, and J. Sinova, “Crystal time-reversal symmetry breaking and spontaneous hall effect in collinear antiferromagnets,” *Science advances*, vol. 6, no. 23, p. eaaz8809, 2020.
- [61] A. Chakraborty, A. B. Hellenes, R. Jaeschke-Ubiergo, T. Jungwirth, L. Šmejkal, and J. Sinova, “Highly efficient non-relativistic edelstein effect in p-wave magnets,” *arXiv preprint arXiv:2411.16378*, 2024.
- [62] R. González-Hernández, P. Ritzinger, K. Vyborný, J. Železný, and A. Manchon, “Non-relativistic torque and edelstein effect in non-collinear magnets,” *Nature Communications*, vol. 15, no. 1, p. 7663, 2024.
- [63] A. B. Hellenes, T. Jungwirth, R. Jaeschke-Ubiergo, A. Chakraborty, J. Sinova, and L. Šmejkal, “P-wave magnets,” *arXiv preprint arXiv:2309.01607*, 2023.
- [64] G. Cuono, R. M. Sattigeri, C. Autieri, and T. Dietl, “Ab initio overestimation of the topological region in eu-based compounds,” *Physical Review B*, vol. 108, no. 7, p. 075150, 2023.
- [65] J.-R. Soh, A. Bombardi, F. Mila, M. C. Rahn, D. Prabhakaran, S. Francoual, H. M. Rønnow, and A. T. Boothroyd, “Understanding unconventional magnetic order in a candidate axion insulator by resonant elastic x-ray scattering,” *Nature Communications*, vol. 14, no. 1, p. 3387, 2023.
- [66] E. Donoway, T. Trevisan, A. Liebman-Peláez, R. Day, K. Yamakawa, Y. Sun, J. Soh, D. Prabhakaran, A. Boothroyd, R. Fernandes, *et al.*, “Multimodal approach reveals the symmetry-breaking pathway to the broken helix in euin 2 as 2,” *Physical Review X*, vol. 14, no. 3, p. 031013, 2024.

- [67] H. Takeda, J. Yan, Z. Jiang, X. Luo, Y. Sun, and M. Yamashita, “Incommensurate magnetic order in an axion insulator candidate $\text{eui}n2as2$ investigated by nmr measurement,” *npj Quantum Materials*, vol. 9, no. 1, p. 67, 2024.
- [68] M. Gen, Y. Fujishiro, K. Okigami, S. Hayami, K. Adachi, D. Hashizume, T. Kurumaji, H. Sagayama, H. Nakao, Y. Tokura, *et al.*, “Incommensurate broken-helix and broken-fanlike states in axion insulator candidate $\text{eui}n_{-2}$ as $_{-2}$,” *arXiv preprint arXiv:2403.03022*, 2024.
- [69] N. A. Á. Pari, R. Jaeschke-Ubiergo, A. Chakraborty, L. Šmejkal, and J. Sinova, “Nonrelativistic linear edelstein effect in helical $\text{eui}n 2$ as 2 ,” *Physical Review B*, vol. 112, no. 2, p. 024404, 2025.
- [70] J. Sivianes, F. J. d. Santos, and J. Ibañez-Azpiroz, “Unconventional p-wave magnets as sources of nonlinear photocurrents,” *arXiv preprint arXiv:2406.19842*, 2024.
- [71] Q. Song, S. Stavrić, P. Barone, A. Droghetti, D. S. Antonenko, J. W. Venderbos, C. A. Occhialini, B. Ilyas, E. Ergeçen, N. Gedik, *et al.*, “Electrical switching of a p-wave magnet,” *Nature*, pp. 1–7, 2025.
- [72] Y. Fukaya, B. Lu, K. Yada, Y. Tanaka, and J. Cayao, “Superconducting phenomena in systems with unconventional magnets,” *arXiv preprint arXiv:2502.15400*, 2025.
- [73] P. Sukhachov, H. G. Gil, B. Brekke, and J. Linder, “Coexistence of p-wave magnetism and superconductivity,” *Physical Review B*, vol. 111, no. 22, p. L220403, 2025.
- [74] L. D. Landau *et al.*, “On the theory of phase transitions,” *Zh. eksp. teor. Fiz.*, vol. 7, no. 19-32, p. 926, 1937.
- [75] F. D. M. Haldane, “Model for a quantum hall effect without landau levels: Condensed-matter realization of the " parity anomaly",” *Physical review letters*, vol. 61, no. 18, p. 2015, 1988.
- [76] C. L. Kane and E. J. Mele, “ \mathbb{Z}_2 topological order and the quantum spin hall effect,” *Physical review letters*, vol. 95, no. 14, p. 146802, 2005.
- [77] J. E. Moore, “The birth of topological insulators,” *Nature*, vol. 464, no. 7286, pp. 194–198, 2010.
- [78] Z. Song, T. Zhang, Z. Fang, and C. Fang, “Quantitative mappings between symmetry and topology in solids,” *Nature communications*, vol. 9, no. 1, p. 3530, 2018.

- [79] W. Brinkman and R. J. Elliott, “Theory of spin-space groups,” *Proceedings of the Royal Society of London. Series A. Mathematical and Physical Sciences*, vol. 294, no. 1438, pp. 343–358, 1966.
- [80] A. B. Hellenes, T. Jungwirth, R. Jaeschke-Ubiergo, A. Chakraborty, J. Sinova, and L. Šmejkal, “P-wave magnets,” 2024.
- [81] M. S. Dresselhaus, G. Dresselhaus, and A. Jorio, *Group theory: application to the physics of condensed matter*. Springer Science & Business Media, 2007.
- [82] R. Elliott, “Spin-orbit coupling in band theory—character tables for some " double" space groups,” *Physical Review*, vol. 96, no. 2, p. 280, 1954.
- [83] L. Elcoro, B. Bradlyn, Z. Wang, M. G. Vergniory, J. Cano, C. Felser, B. A. Bernevig, D. Orobengoa, G. Flor, and M. I. Aroyo, “Double crystallographic groups and their representations on the Bilbao crystallographic server,” *Applied Crystallography*, vol. 50, no. 5, pp. 1457–1477, 2017.
- [84] C. Bradley and B. Davies, “Magnetic groups and their corepresentations,” *Reviews of Modern Physics*, vol. 40, no. 2, p. 359, 1968.
- [85] D. B. Litvin, “Spin translation groups and neutron diffraction analysis,” *Foundations of Crystallography*, vol. 29, no. 6, pp. 651–660, 1973.
- [86] O. Fedchenko, J. Minár, A. Akashdeep, S. W. D’Souza, D. Vasilyev, O. Tkach, L. Odenbreit, Q. Nguyen, D. Kutnyakhov, N. Wind, *et al.*, “Observation of time-reversal symmetry breaking in the band structure of altermagnetic RuO₂,” *Science advances*, vol. 10, no. 5, p. eadj4883, 2024.
- [87] Z. Lin, D. Chen, W. Lu, X. Liang, S. Feng, K. Yamagami, J. Osiecki, M. Andersson, B. Thiagarajan, J. Liu, *et al.*, “Observation of giant spin splitting and d-wave spin texture in room temperature altermagnet RuO₂,” *arXiv preprint arXiv:2402.04995*, 2024.
- [88] H. Reichlova, R. Lopes Seeger, R. González-Hernández, I. Kounta, R. Schlitz, D. Kriegner, P. Ritzinger, M. Lammel, M. Leiviskä, A. Birk Hellenes, *et al.*, “Observation of a spontaneous anomalous hall response in the Mn₅Si₃ d-wave altermagnet candidate,” *Nature Communications*, vol. 15, no. 1, p. 4961, 2024.
- [89] B. Jiang, M. Hu, J. Bai, Z. Song, C. Mu, G. Qu, W. Li, W. Zhu, H. Pi, Z. Wei, *et al.*, “A metallic room-temperature d-wave altermagnet,” *Nature Physics*, pp. 1–6, 2025.
- [90] J. Krempaský, L. Šmejkal, S. D’souza, M. Hajlaoui, G. Springholz, K. Uhlířová, F. Alarab, P. Constantinou, V. Strocov, D. Usanov, *et al.*, “Altermagnetic lifting of kramers spin degeneracy,” *Nature*, vol. 626, no. 7999, pp. 517–522, 2024.

- [91] S. Lee, S. Lee, S. Jung, J. Jung, D. Kim, Y. Lee, B. Seok, J. Kim, B. G. Park, L. Šmejkal, *et al.*, “Broken kramers degeneracy in altermagnetic mnte,” *Physical review letters*, vol. 132, no. 3, p. 036702, 2024.
- [92] J. Ding, Z. Jiang, X. Chen, Z. Tao, Z. Liu, T. Li, J. Liu, J. Sun, J. Cheng, J. Liu, *et al.*, “Large band splitting in g-wave altermagnet crsb,” *Physical Review Letters*, vol. 133, no. 20, p. 206401, 2024.
- [93] S. Reimers, L. Odenbreit, L. Šmejkal, V. N. Strocov, P. Constantinou, A. B. Hellenes, R. Jaeschke Ubiergo, W. H. Campos, V. K. Bharadwaj, A. Chakraborty, *et al.*, “Direct observation of altermagnetic band splitting in crsb thin films,” *Nature Communications*, vol. 15, no. 1, p. 2116, 2024.
- [94] K. Shinohara, A. Togo, H. Watanabe, T. Nomoto, I. Tanaka, and R. Arita, “Algorithm for spin symmetry operation search,” *Acta Crystallographica Section A: Foundations and Advances*, vol. 80, no. 1, 2024.
- [95] N. Ong and S. Liang, “Experimental signatures of the chiral anomaly in dirac–weyl semimetals,” *Nature Reviews Physics*, vol. 3, no. 6, pp. 394–404, 2021.
- [96] S. D. Sarma, M. Freedman, and C. Nayak, “Majorana zero modes and topological quantum computation,” *npj Quantum Information*, vol. 1, no. 1, pp. 1–13, 2015.
- [97] S. Frolov, M. Manfra, and J. Sau, “Topological superconductivity in hybrid devices,” *Nature Physics*, vol. 16, no. 7, pp. 718–724, 2020.
- [98] K. v. Klitzing, G. Dorda, and M. Pepper, “New method for high-accuracy determination of the fine-structure constant based on quantized hall resistance,” *Physical review letters*, vol. 45, no. 6, p. 494, 1980.
- [99] D. J. Thouless, M. Kohmoto, M. P. Nightingale, and M. den Nijs, “Quantized hall conductance in a two-dimensional periodic potential,” *Physical review letters*, vol. 49, no. 6, p. 405, 1982.
- [100] M. V. Berry, “Quantal phase factors accompanying adiabatic changes,” *Proceedings of the Royal Society of London. A. Mathematical and Physical Sciences*, vol. 392, no. 1802, pp. 45–57, 1984.
- [101] D. Vanderbilt, *Berry phases in electronic structure theory: electric polarization, orbital magnetization and topological insulators*. Cambridge University Press, 2018.
- [102] M. Z. Hasan and C. L. Kane, “Colloquium: topological insulators,” *Reviews of modern physics*, vol. 82, no. 4, pp. 3045–3067, 2010.

- [103] L. Trifunovic and P. W. Brouwer, “Higher-order bulk-boundary correspondence for topological crystalline phases,” *Physical Review X*, vol. 9, no. 1, p. 011012, 2019.
- [104] A. Bansil, H. Lin, and T. Das, “Colloquium: Topological band theory,” *Reviews of Modern Physics*, vol. 88, no. 2, p. 021004, 2016.
- [105] H. Zhang, C.-X. Liu, X.-L. Qi, X. Dai, Z. Fang, and S.-C. Zhang, “Topological insulators in Bi_2Se_3 , Bi_2Te_3 and Sb_2Te_3 with a single Dirac cone on the surface,” *Nature physics*, vol. 5, no. 6, pp. 438–442, 2009.
- [106] L. Fu, C. L. Kane, and E. J. Mele, “Topological insulators in three dimensions,” *Physical review letters*, vol. 98, no. 10, p. 106803, 2007.
- [107] R. S. Mong, A. M. Essin, and J. E. Moore, “Antiferromagnetic topological insulators,” *Physical Review B—Condensed Matter and Materials Physics*, vol. 81, no. 24, p. 245209, 2010.
- [108] X.-L. Qi, T. L. Hughes, and S.-C. Zhang, “Topological field theory of time-reversal invariant insulators,” *Physical Review B—Condensed Matter and Materials Physics*, vol. 78, no. 19, p. 195424, 2008.
- [109] C. Vafa and E. Witten, “Parity conservation in quantum chromodynamics,” *Physical Review Letters*, vol. 53, no. 6, p. 535, 1984.
- [110] F. Chadha-Day, J. Ellis, and D. J. Marsh, “Axion dark matter: What is it and why now?,” *Science advances*, vol. 8, no. 8, p. eabj3618, 2022.
- [111] N. Varnava and D. Vanderbilt, “Surfaces of axion insulators,” *Physical Review B*, vol. 98, no. 24, p. 245117, 2018.
- [112] A. M. Essin, J. E. Moore, and D. Vanderbilt, “Magnetoelectric polarizability and axion electrodynamics in crystalline insulators,” *Physical review letters*, vol. 102, no. 14, p. 146805, 2009.
- [113] A. M. Turner, Y. Zhang, R. S. Mong, and A. Vishwanath, “Quantized response and topology of magnetic insulators with inversion symmetry,” *Physical Review B—Condensed Matter and Materials Physics*, vol. 85, no. 16, p. 165120, 2012.
- [114] T. H. Hsieh, H. Lin, J. Liu, W. Duan, A. Bansil, and L. Fu, “Topological crystalline insulators in the SnTe material class,” *Nature communications*, vol. 3, no. 1, p. 982, 2012.
- [115] R.-J. Slager, A. Mesaros, V. Juričić, and J. Zaanen, “The space group classification of topological band-insulators,” *Nature Physics*, vol. 9, no. 2, pp. 98–102, 2013.

- [116] J. C. Teo, L. Fu, and C. Kane, “Surface states and topological invariants in three-dimensional topological insulators: Application to Bi_2Se_3 ,” *Physical Review B—Condensed Matter and Materials Physics*, vol. 78, no. 4, p. 045426, 2008.
- [117] J. Liu, T. H. Hsieh, P. Wei, W. Duan, J. Moodera, and L. Fu, “Spin-filtered edge states with an electrically tunable gap in a two-dimensional topological crystalline insulator,” *Nature materials*, vol. 13, no. 2, pp. 178–183, 2014.
- [118] I. Zeljkovic, D. Walkup, B. A. Assaf, K. L. Scipioni, R. Sankar, F. Chou, and V. Madhavan, “Strain engineering dirac surface states in heteroepitaxial topological crystalline insulator thin films,” *Nature nanotechnology*, vol. 10, no. 10, pp. 849–853, 2015.
- [119] X. Qian, L. Fu, and J. Li, “Topological crystalline insulator nanomembrane with strain-tunable band gap,” *Nano Research*, vol. 8, no. 3, pp. 967–979, 2015.
- [120] D. Walkup, B. A. Assaf, K. L. Scipioni, R. Sankar, F. Chou, G. Chang, H. Lin, I. Zeljkovic, and V. Madhavan, “Interplay of orbital effects and nanoscale strain in topological crystalline insulators,” *Nature communications*, vol. 9, no. 1, p. 1550, 2018.
- [121] W. A. Benalcazar, B. A. Bernevig, and T. L. Hughes, “Quantized electric multipole insulators,” *Science*, vol. 357, no. 6346, pp. 61–66, 2017.
- [122] Z. Song, Z. Fang, and C. Fang, “(d-2)-dimensional edge states of rotation symmetry protected topological states,” *Physical review letters*, vol. 119, no. 24, p. 246402, 2017.
- [123] F. Schindler, A. M. Cook, M. G. Vergniory, Z. Wang, S. S. Parkin, B. A. Bernevig, and T. Neupert, “Higher-order topological insulators,” *Science advances*, vol. 4, no. 6, p. eaat0346, 2018.
- [124] B. Xie, H.-X. Wang, X. Zhang, P. Zhan, J.-H. Jiang, M. Lu, and Y. Chen, “Higher-order band topology,” *Nature Reviews Physics*, vol. 3, no. 7, pp. 520–532, 2021.
- [125] M. Gu, J. Li, H. Sun, Y. Zhao, C. Liu, J. Liu, H. Lu, and Q. Liu, “Spectral signatures of the surface anomalous hall effect in magnetic axion insulators,” *Nature communications*, vol. 12, no. 1, p. 3524, 2021.
- [126] C. Yue, Y. Xu, Z. Song, H. Weng, Y.-M. Lu, C. Fang, and X. Dai, “Symmetry-enforced chiral hinge states and surface quantum anomalous hall effect in the magnetic axion insulator Bi_2Se_3 ,” *Nature Physics*, vol. 15, no. 6, pp. 577–581, 2019.

- [127] M. S. Hossain, Q. Zhang, Z. Wang, N. Dhale, W. Liu, M. Litskevich, B. Casas, N. Shumiya, J.-X. Yin, T. A. Cochran, *et al.*, “Quantum transport response of topological hinge modes,” *Nature Physics*, vol. 20, no. 5, pp. 776–782, 2024.
- [128] A. Burkov, “Topological semimetals,” *Nature materials*, vol. 15, no. 11, pp. 1145–1148, 2016.
- [129] L. Šmejkal, T. Jungwirth, and J. Sinova, “Route towards dirac and weyl anti-ferromagnetic spintronics,” *physica status solidi (RRL)–Rapid Research Letters*, vol. 11, no. 4, p. 1700044, 2017.
- [130] N. P. Armitage, E. J. Mele, and A. Vishwanath, “Weyl and dirac semimetals in three-dimensional solids,” *Reviews of Modern Physics*, vol. 90, no. 1, p. 015001, 2018.
- [131] X. Wan, A. M. Turner, A. Vishwanath, and S. Y. Savrasov, “Topological semimetal and fermi-arc surface states in the electronic structure of pyrochlore iridates,” *Physical Review B—Condensed Matter and Materials Physics*, vol. 83, no. 20, p. 205101, 2011.
- [132] B. Lv, H. Weng, B. Fu, X. P. Wang, H. Miao, J. Ma, P. Richard, X. Huang, L. Zhao, G. Chen, *et al.*, “Experimental discovery of weyl semimetal taas,” *Physical Review X*, vol. 5, no. 3, p. 031013, 2015.
- [133] S. N. Guin, P. Vir, Y. Zhang, N. Kumar, S. J. Watzman, C. Fu, E. Liu, K. Manna, W. Schnelle, J. Gooth, *et al.*, “Zero-field nernst effect in a ferromagnetic kagome-lattice weyl-semimetal $\text{Co}_3\text{Sn}_2\text{S}_2$,” *Advanced Materials*, vol. 31, no. 25, p. 1806622, 2019.
- [134] D. Liu, A. Liang, E. Liu, Q. Xu, Y. Li, C. Chen, D. Pei, W. Shi, S. Mo, P. Dudin, *et al.*, “Magnetic weyl semimetal phase in a kagomé crystal,” *Science*, vol. 365, no. 6459, pp. 1282–1285, 2019.
- [135] R. M. Fernandes, V. S. De Carvalho, T. Birol, and R. G. Pereira, “Topological transition from nodal to nodeless zeeman splitting in altermagnets,” *Physical Review B*, vol. 109, no. 2, p. 024404, 2024.
- [136] C. Li, M. Hu, Z. Li, Y. Wang, W. Chen, B. Thiagarajan, M. Leandersson, C. Polley, T. Kim, H. Liu, *et al.*, “Topological weyl altermagnetism in crsb,” *Communications Physics*, vol. 8, no. 1, p. 311, 2025.
- [137] S. M. Young, S. Zaheer, J. C. Teo, C. L. Kane, E. J. Mele, and A. M. Rappe, “Dirac semimetal in three dimensions,” *Physical review letters*, vol. 108, no. 14, p. 140405, 2012.

- [138] B.-J. Yang and N. Nagaosa, “Classification of stable three-dimensional dirac semimetals with nontrivial topology,” *Nature communications*, vol. 5, no. 1, p. 4898, 2014.
- [139] A. Burkov, M. Hook, and L. Balents, “Topological nodal semimetals,” *Physical Review B—Condensed Matter and Materials Physics*, vol. 84, no. 23, p. 235126, 2011.
- [140] L. M. Schoop, M. N. Ali, C. Straßer, A. Topp, A. Varykhalov, D. Marchenko, V. Duppel, S. S. Parkin, B. V. Lotsch, and C. R. Ast, “Dirac cone protected by non-symmorphic symmetry and three-dimensional dirac line node in zrsi,” *Nature communications*, vol. 7, no. 1, p. 11696, 2016.
- [141] Z. Wang, Y. Sun, X.-Q. Chen, C. Franchini, G. Xu, H. Weng, X. Dai, and Z. Fang, “Dirac semimetal and topological phase transitions in a 3 bi (a= na, k, rb),” *Physical Review B—Condensed Matter and Materials Physics*, vol. 85, no. 19, p. 195320, 2012.
- [142] Z. Liu, B. Zhou, Y. Zhang, Z. Wang, H. Weng, D. Prabhakaran, S.-K. Mo, Z. Shen, Z. Fang, X. Dai, *et al.*, “Discovery of a three-dimensional topological dirac semimetal, Na₃Bi,” *Science*, vol. 343, no. 6173, pp. 864–867, 2014.
- [143] J. Xiong, S. K. Kushwaha, T. Liang, J. W. Krizan, M. Hirschberger, W. Wang, R. J. Cava, and N. P. Ong, “Evidence for the chiral anomaly in the dirac semimetal na₃bi,” *Science*, vol. 350, no. 6259, pp. 413–416, 2015.
- [144] S.-Y. Xu, C. Liu, S. K. Kushwaha, R. Sankar, J. W. Krizan, I. Belopolski, M. Neupane, G. Bian, N. Alidoust, T.-R. Chang, *et al.*, “Observation of fermi arc surface states in a topological metal,” *Science*, vol. 347, no. 6219, pp. 294–298, 2015.
- [145] P. J. Moll, N. L. Nair, T. Helm, A. C. Potter, I. Kimchi, A. Vishwanath, and J. G. Analytis, “Transport evidence for fermi-arc-mediated chirality transfer in the dirac semimetal cd₃as₂,” *Nature*, vol. 535, no. 7611, pp. 266–270, 2016.
- [146] Z. Sun, A. Wang, H. Mu, H. Wang, Z. Wang, T. Wu, Z. Wang, X. Zhou, and X. Chen, “Field-induced metal-to-insulator transition and colossal anisotropic magnetoresistance in a nearly dirac material eumnsb₂,” *npj Quantum Materials*, vol. 6, no. 1, p. 94, 2021.
- [147] R. Singha, K. J. Dalgaard, D. Marchenko, M. Krivenkov, E. D. Rienks, M. Jovanovic, S. M. Teicher, J. Hu, T. H. Salters, J. Lin, *et al.*, “Colossal magnetoresistance in the multiple wave vector charge density wave regime of an anti-ferromagnetic dirac semimetal,” *Science Advances*, vol. 9, no. 41, p. eadh0145, 2023.

- [148] M. I. Aroyo, J. M. Perez-Mato, D. Orobengoa, E. Tasci, G. de la Flor, and A. Kirov, “Crystallography online: Bilbao crystallographic server,” *Bulg. Chem. Commun*, vol. 43, no. 2, pp. 183–197, 2011.
- [149] M. Iraola, J. L. Mañes, B. Bradlyn, M. K. Horton, T. Neupert, M. G. Vergniory, and S. S. Tsirkin, “Irrep: symmetry eigenvalues and irreducible representations of ab initio band structures,” *Computer Physics Communications*, vol. 272, p. 108226, 2022.
- [150] P. Hohenberg and W. Kohn, “Inhomogeneous electron gas,” *Physical review*, vol. 136, no. 3B, p. B864, 1964.
- [151] W. Kohn, A. D. Becke, and R. G. Parr, “Density functional theory of electronic structure,” *The journal of physical chemistry*, vol. 100, no. 31, pp. 12974–12980, 1996.
- [152] W. Kohn and L. J. Sham, “Self-consistent equations including exchange and correlation effects,” *Physical review*, vol. 140, no. 4A, p. A1133, 1965.
- [153] G. Kresse and J. Furthmüller, “Efficient iterative schemes for ab initio total-energy calculations using a plane-wave basis set,” *Physical review B*, vol. 54, no. 16, p. 11169, 1996.
- [154] D. Hobbs, G. Kresse, and J. Hafner, “Fully unconstrained noncollinear magnetism within the projector augmented-wave method,” *Physical Review B*, vol. 62, no. 17, p. 11556, 2000.
- [155] P.-W. Ma and S. Dudarev, “Constrained density functional for noncollinear magnetism,” *Physical Review B*, vol. 91, no. 5, p. 054420, 2015.
- [156] J. Toulouse, “Review of approximations for the exchange-correlation energy in density-functional theory,” in *Density Functional Theory: Modeling, Mathematical Analysis, Computational Methods, and Applications*, pp. 1–90, Springer, 2022.
- [157] J. P. Perdew, K. Burke, and M. Ernzerhof, “Generalized gradient approximation made simple,” *Physical review letters*, vol. 77, no. 18, p. 3865, 1996.
- [158] V. I. Anisimov, J. Zaanen, and O. K. Andersen, “Band theory and mott insulators: Hubbard u instead of stoner i,” *Physical Review B*, vol. 44, no. 3, p. 943, 1991.
- [159] A. Liechtenstein, V. I. Anisimov, and J. Zaanen, “Density-functional theory and strong interactions: Orbital ordering in mott-hubbard insulators,” *Physical Review B*, vol. 52, no. 8, p. R5467, 1995.

- [160] S. L. Dudarev, G. A. Botton, S. Y. Savrasov, C. Humphreys, and A. P. Sutton, “Electron-energy-loss spectra and the structural stability of nickel oxide: An lsdas study,” *Physical Review B*, vol. 57, no. 3, p. 1505, 1998.
- [161] E. Pavarini, S. Zhang, and E. Koch, *Many-body methods for real materials*. No. FZJ-2019-04474, Theoretische Nanoelektronik, 2019.
- [162] A. Georges, G. Kotliar, W. Krauth, and M. J. Rozenberg, “Dynamical mean-field theory of strongly correlated fermion systems and the limit of infinite dimensions,” *Reviews of modern physics*, vol. 68, no. 1, p. 13, 1996.
- [163] D. Hamann, M. Schlüter, and C. Chiang, “Norm-conserving pseudopotentials,” *Physical review letters*, vol. 43, no. 20, p. 1494, 1979.
- [164] W. E. Pickett, “Pseudopotential methods in condensed matter applications,” *Computer Physics Reports*, vol. 9, no. 3, pp. 115–197, 1989.
- [165] D. Vanderbilt, “Soft self-consistent pseudopotentials in a generalized eigenvalue formalism,” *Physical review B*, vol. 41, no. 11, p. 7892, 1990.
- [166] P. E. Blöchl, “Projector augmented-wave method,” *Physical review B*, vol. 50, no. 24, p. 17953, 1994.
- [167] G. Kresse and D. Joubert, “From ultrasoft pseudopotentials to the projector augmented-wave method,” *Physical review b*, vol. 59, no. 3, p. 1758, 1999.
- [168] S. Steiner, S. Khmelevskiy, M. Marsmann, and G. Kresse, “Calculation of the magnetic anisotropy with projected-augmented-wave methodology and the case study of disordered fe_{1-x}co_x alloys,” *Physical review B*, vol. 93, no. 22, p. 224425, 2016.
- [169] A. A. Mostofi, J. R. Yates, Y.-S. Lee, I. Souza, D. Vanderbilt, and N. Marzari, “wannier90: A tool for obtaining maximally-localised wannier functions,” *Computer physics communications*, vol. 178, no. 9, pp. 685–699, 2008.
- [170] X. Wang, J. R. Yates, I. Souza, and D. Vanderbilt, “Ab initio calculation of the anomalous hall conductivity by wannier interpolation,” *Physical Review B—Condensed Matter and Materials Physics*, vol. 74, no. 19, p. 195118, 2006.
- [171] N. Marzari, A. A. Mostofi, J. R. Yates, I. Souza, and D. Vanderbilt, “Maximally localized wannier functions: Theory and applications,” *Reviews of Modern Physics*, vol. 84, no. 4, pp. 1419–1475, 2012.
- [172] G.-X. Zhi, C. Xu, S.-Q. Wu, F. Ning, and C. Cao, “Wannsymm: A symmetry analysis code for wannier orbitals,” *Computer Physics Communications*, vol. 271, p. 108196, 2022.

- [173] Q. Wu, S. Zhang, H.-F. Song, M. Troyer, and A. A. Soluyanov, “Wanniertools: An open-source software package for novel topological materials,” *Computer Physics Communications*, vol. 224, pp. 405–416, 2018.
- [174] D. Lee and J. Joannopoulos, “Simple scheme for surface-band calculations. i,” *Physical Review B*, vol. 23, no. 10, p. 4988, 1981.
- [175] M. L. Sancho, J. L. Sancho, and J. Rubio, “Quick iterative scheme for the calculation of transfer matrices: application to mo (100),” *Journal of Physics F: Metal Physics*, vol. 14, no. 5, p. 1205, 1984.
- [176] M. L. Sancho, J. L. Sancho, J. L. Sancho, and J. Rubio, “Highly convergent schemes for the calculation of bulk and surface green functions,” *Journal of Physics F: Metal Physics*, vol. 15, no. 4, p. 851, 1985.
- [177] F. Boschini, M. Zonno, and A. Damascelli, “Time-resolved arpes studies of quantum materials,” *Reviews of Modern Physics*, vol. 96, no. 1, p. 015003, 2024.
- [178] H. Wang, D. Wu, Y. Shi, and N. Wang, “Anisotropic transport and optical spectroscopy study on antiferromagnetic triangular lattice eucd₂as₂: An interplay between magnetism and charge transport properties,” *Physical Review B*, vol. 94, no. 4, p. 045112, 2016.
- [179] I. Schellenberg, U. Pfannenschmidt, M. Eul, C. Schwickert, and R. Pöttgen, “A 121sb and 151eu mössbauer spectroscopic investigation of eucd₂x₂ (x= p, as, sb) and ybcd₂sb₂,” *Zeitschrift für anorganische und allgemeine Chemie*, vol. 637, no. 12, pp. 1863–1870, 2011.
- [180] Y. Wu, N. H. Jo, L.-L. Wang, C. A. Schmidt, K. M. Neilson, B. Schruck, P. Swatek, A. Eaton, S. L. Bud’ko, P. C. Canfield, *et al.*, “Fragility of fermi arcs in dirac semimetals,” *Physical Review B*, vol. 99, no. 16, p. 161113, 2019.
- [181] Y. Zhang, K. Deng, X. Zhang, M. Wang, Y. Wang, C. Liu, J.-W. Mei, S. Kumar, E. F. Schwier, K. Shimada, *et al.*, “In-plane antiferromagnetic moments and magnetic polaron in the axion topological insulator candidate EuIn₂As₂,” *Physical Review B*, vol. 101, no. 20, p. 205126, 2020.
- [182] A. B. Sarkar, S. Mardanya, S.-M. Huang, B. Ghosh, C.-Y. Huang, H. Lin, A. Bansil, T.-R. Chang, A. Agarwal, and B. Singh, “Magnetically tunable dirac and weyl fermions in the zintl materials family,” *Physical Review Materials*, vol. 6, no. 4, p. 044204, 2022.
- [183] S. Riberolles, A. Nedić, B. Kuthanazhi, F. Ye, S. Bud’ko, P. Canfield, R. McQueeney, J. Ahn, V. Quito, T. Trevisan, *et al.*, “Symmetry tuning topological

states of an axion insulator with noncollinear magnetic order,” *arXiv preprint arXiv:2505.22796*, 2025.

- [184] L. Sandratskii, “Symmetry analysis of electronic states for crystals with spiral magnetic order. i. general properties,” *Journal of Physics: Condensed Matter*, vol. 3, no. 44, p. 8565, 1991.
- [185] Y. B. Kudasov, “Topological band structure due to modified kramers degeneracy for electrons in a helical magnetic field,” *Physical Review B*, vol. 109, no. 14, p. L140402, 2024.
- [186] “Labels of the non-collinear magnetic phases of EuIn_2As_2 in magndata: helical(#1.0.31), broken-helical(#1.0.32),”
- [187] A. Johansson, J. Henk, and I. Mertig, “Theoretical aspects of the edelstein effect for anisotropic two-dimensional electron gas and topological insulators,” *Physical Review B*, vol. 93, no. 19, p. 195440, 2016.
- [188] A. Manchon, J. Železný, I. M. Miron, T. Jungwirth, J. Sinova, A. Thiaville, K. Garello, and P. Gambardella, “Current-induced spin-orbit torques in ferromagnetic and antiferromagnetic systems,” *Reviews of Modern Physics*, vol. 91, no. 3, p. 035004, 2019.
- [189] G. Bihlmayer, P. Noël, D. V. Vyalikh, E. V. Chulkov, and A. Manchon, “Rashba-like physics in condensed matter,” *Nature Reviews Physics*, vol. 4, no. 10, pp. 642–659, 2022.
- [190] J. Železný, H. Gao, K. Vybourný, J. Zemen, J. Mašek, A. Manchon, J. Wunderlich, J. Sinova, and T. Jungwirth, “Relativistic néel-order fields induced by electrical current in antiferromagnets,” *Physical review letters*, vol. 113, no. 15, p. 157201, 2014.
- [191] S. Leiva-Montecinos, J. Henk, I. Mertig, and A. Johansson, “Spin and orbital edelstein effect in a bilayer system with rashba interaction,” *Physical Review Research*, vol. 5, no. 4, p. 043294, 2023.
- [192] I. Garate and A. H. MacDonald, “Influence of a transport current on magnetic anisotropy in gyrotropic ferromagnets,” *Physical Review B—Condensed Matter and Materials Physics*, vol. 80, no. 13, p. 134403, 2009.
- [193] H. Li, H. Gao, L. P. Zárbo, K. Vybourný, X. Wang, I. Garate, F. Doğan, A. Čejchan, J. Sinova, T. Jungwirth, *et al.*, “Intraband and interband spin-orbit torques in noncentrosymmetric ferromagnets,” *Physical Review B*, vol. 91, no. 13, p. 134402, 2015.

- [194] J. Železný, H. Gao, A. Manchon, F. Freimuth, Y. Mokrousov, J. Zemen, J. Mašek, J. Sinova, and T. Jungwirth, “Spin-orbit torques in locally and globally noncentrosymmetric crystals: Antiferromagnets and ferromagnets,” *Physical Review B*, vol. 95, no. 1, p. 014403, 2017.
- [195] J. Yan, Z. Z. Jiang, R. C. Xiao, W. Lu, W. Song, X. Zhu, X. Luo, Y. Sun, and M. Yamashita, “Field-induced topological hall effect in antiferromagnetic axion insulator candidate EuIn_2As_2 ,” *Physical Review Research*, vol. 4, no. 1, p. 013163, 2022.
- [196] S. Regmi, M. M. Hosen, B. Ghosh, B. Singh, G. Dhakal, C. Sims, B. Wang, F. Kabir, K. Dimitri, Y. Liu, *et al.*, “Temperature-dependent electronic structure in a higher-order topological insulator candidate EuIn_2As_2 ,” *Physical Review B*, vol. 102, no. 16, p. 165153, 2020.
- [197] J. Yan, J. Si, Z. Jiang, H. Ma, Y. Uwatoko, B.-T. Wang, X. Luo, Y. Sun, and M. Yamashita, “Doping-tunable fermi surface with persistent topological hall effect in the axion candidate EuIn_2As_2 ,” *Physical Review B*, vol. 110, no. 11, p. 115111, 2024.
- [198] D. Santos-Cottin, I. Mohelský, J. Wyzula, F. Le Mardelé, I. Kapon, S. Nasrallah, N. Barišić, I. Živković, J. Soh, F. Guo, *et al.*, “ EuIn_2As_2 : A magnetic semiconductor,” *Physical review letters*, vol. 131, no. 18, p. 186704, 2023.
- [199] A. Cracknell, “Symmetry properties of the transport coefficients of magnetic crystals,” *Physical Review B*, vol. 7, no. 5, p. 2145, 1973.